

3. SITE 794¹

Shipboard Scientific Party²

HOLE 794D

Date occupied: 1. 5 September 1989 2. 22 September 1989
Date departed: 1. 13 September 1989 2. 29 September 1989
Time on hole: 14 days, 19 hr, 49 min
Position: 40°11.366'N, 138°13.944'E
Bottom felt (rig floor; m, drill-pipe measurement): 2818.0
Distance between rig floor and sea level (m): 11.1
Water depth (drill-pipe measurement from sea level, m): 2806.9
Total depth (rig floor, m): 3551.5
Penetration (m): 733.5
Number of cores: 20
Total length of cored section (m): 160.5
Total core recovered (m): 34.85
Core recovery (%): 21.7

Hard rock:

Depth (mbsf): 573.0
Nature: olivine dolerite
Measured velocity (km/s): 5.4

Comments: 1. Operations were conducted in two stages (two visits).
2. Downhole seismometer was permanently installed in this hole for long-term monitoring.

HOLE 794E

Date occupied: 30 September 1989
Date departed: 1 October 1989
Time on hole: 20 hr, 5 min
Position: 40°10.532'N, 138°13.954'E
Bottom felt (rig floor; m, drill-pipe measurement): 2812.5
Distance between rig floor and sea level (m): 11.1
Water depth (drill-pipe measurement from sea level, m): 2800.9
Total depth (rig floor, m): 3212.0
Penetration (m): 400.0
Number of cores: 0
Total length of cored section (m): 0
Total core recovered (m): 0

Comments: No core was recovered. This was a "dedicated hole" to conduct electrical resistivity experiments.

Principal results: Site 794 in the northern Yamato Basin had been scheduled to be occupied during both Legs 127 and 128 in the Japan Sea.

Multiple Occupation of Site 794

The primary drilling objective at this site was penetration and sampling of acoustic basement in a basinal location. Leg 127 had been targeted for this task. The original plan then called for Site 794 to be reoccupied during Leg 128, and two geophysical experiments to be conducted involving a hole previously drilled and cased during Leg 127 and a new, dedicated hole to be drilled during Leg 128. As it turned out, a stuck bottom-hole assembly (BHA) was left in Hole 794C during Leg 127, and ultimately this required a revised schedule for Leg 128 that involved (1) the drilling of two holes at Site 794 because of the failure to recover the stuck BHA and (2) two visits to Site 794 to accommodate a pre-arranged rendezvous with two support vessels that was necessary for completing the geophysical experiments at this site.

The primary drilling objective at Site 794 was met during Leg 127 when scientists recovered a 543-m-thick, Miocene to Holocene, sedimentary sequence and cored a 108.7-m-thick sequence of underlying dolerites and minor sediment representing acoustic basement (a summary of Leg 127 results at Site 794 is included in the "Background and Scientific Objectives" section, this chapter). Primary objectives at Site 794 for Leg 128 were (1) to emplace a downhole seismometer in the basement rock, (2) to conduct a real-time seismic experiment using the downhole instrument, ocean bottom seismometers, and two support ships from the University of Tokyo Ocean Research Institute, and (3) to drill a dedicated hole and perform an electrical resistivity experiment, which also involved the use of support ships. Because of the revised schedule for Leg 128, a fourth objective was added to this list, which was to drill deeper into the igneous basement sequence initially cored during Leg 127.

Drilling of Site 794 during Leg 128 penetrated a total of 160.5 m into the igneous complex representing the early Miocene(?) volcanic floor of the northern Yamato Basin. Hence, rocks recovered from the lower portion of Hole 794D are interpreted to represent igneous "basement" beneath this site.

Drilling in Holes 794B and 794C during Leg 127 initially cored the igneous sequence at this site from the base of the sediment column at 542.4 to 653.7 mbsf, whereas during Leg 128, we cored the interval between 573.0 to 733.5 mbsf in Hole 794D. By correlating and combining core data from Holes 794B and 794C (Tamaki, Pisciotto, Allan, et al., in press) with core and logging data from Hole 794D, a total of 184.7 m of predominantly igneous lithostratigraphy was established at Site 794 between depths of 542.4 and 733.5 mbsf, yielding a detailed record of magmatic events during the early evolution of the Yamato Basin as summarized below.

1. A total of nine hard-rock lithologic units were recognized within the sequence cored between 573.0 and 733.5 mbsf in Hole 794D, including four dolerite sills (Units 1, 3, 4, and 9) that intruded into soft sediments at shallow depth, four doleritic basalts (Units 2, 6, 7, and 8) that erupted onto the seafloor or intruded into soft sediment near the seafloor, and a thin (1.6 m) interbed of tuffaceous clay that constitutes Unit 5. A tenth unit, which represents the shallowest dolerite sill in this complex, was cored exclusively in Hole 794B during Leg 127 and is herein designated as Unit 0.

2. Although none of the igneous rocks at Site 794 have been radiometrically dated, marine sediments overlying the shallowest dolerite sill (Unit 0) cored in Hole 794B are estimated to range from 15.8 to 16.5 Ma, or late early Miocene in age (Tamaki, Pisciotto, Allan, et al., in press) on the basis of evidence indicating

¹ Ingle, J. C., Jr., Suyehiro, K., von Breyman, M. T., et al., 1990. *Proc. ODP, Init. Repts.*, 128: College Station, TX (Ocean Drilling Program).

² Shipboard Scientific Party is as given in list of participants preceding the contents.

intrusion of the upper portion of the igneous complex into these sediments. The upper flows and sills have been assigned a maximum of late early Miocene age.

3. Shipboard X-ray fluorescence (XRF) analysis of major and trace elements, together with analyses completed during Leg 127 (Tamaki, Pisciotto, Allan, et al., in press) indicate that the Site 794 igneous sequence represents two distinct magmatic complexes, including (1) an upper and younger set of sills and flows of probable island-arc tholeiite composition (Units 0, 1, 2, 3, and 4) and (2) an older and lower sequence of ocean floor basalts of back-arc tholeiite composition (Units 6, 7, 8, and 9), which probably constitutes the igneous basement beneath the Yamato Basin, as extruded and injected during initial rapid back-arc spreading and formation of this portion of the Japan Sea.

Geophysical Experiments

A downhole seismic experiment and an electrical resistivity measuring experiment were performed in Holes 794D and 794E, respectively. A digital, broad-band, three-component, seismometer package was installed at 715 mbsf within the igneous rock section of Hole 794D. Before this, the support ship *Tansei-maru* of the University of Tokyo Ocean Research Institute had deployed nine ocean bottom seismographs (OBS) for the ensuing controlled-source seismic experiment. The *Tansei-maru* shot air guns as she traversed two concentric and two crossing line profiles around Hole 794D. A continuous, 48-hr, real-time recording of the air-gun events was made on board the *JOIDES Resolution*, beginning on 26 September 1989. A second support ship, the *Kaiko-maru-5*, arrived at the site to deploy the seafloor recording and retrieval units. The seafloor unit consists of a battery power supply for the downhole and seafloor instruments and an event-driven digital recorder designed to operate for a few months. The retrieval unit was equipped with an acoustic transponder and glass-sphere buoys and was connected to the recorder unit via a 6000-m rope system. Deployment was completed successfully on 30 September.

Hole 794E, a dedicated hole for use in the electrical resistivity experiment, was drilled while the *Kaiko-maru-5* deployed the seafloor units for the seismic experiment. A cable was lowered to measure electric potentials at five depths within Hole 794E. The *Kaiko-maru-5* acted as the shooting/source vessel to inject electric current of 20 A with 100 V into the water column at distances of 1 to 7 km in two different directions from Hole 794E. The electrical potentials induced by this active experiment were measured successfully and reflect the resistivity structure to about 10 km beneath the site. The experiment was completed on 1 October.

Location and Approach

Site 794 is located in the northeastern corner of the Yamato Basin at the original location approved as proposed Site J1b. The location of Site 794 was confirmed by two *JOIDES Resolution* seismic lines run prior to drilling during Leg 127 at this site (Tamaki, Pisciotto, et al., in press). During Leg 127, a second crossing of this site was made parallel to *DELP* cruise multichannel Line E, with the beacon dropped during a third crossing of the site. During Leg 128, we arrived at Site 794 to find that the beacon deployed during Leg 127 had not been working, and so a new beacon was deployed before we began an unsuccessful fishing operation for the BHA that was stuck in Hole 794C. Hole 794D was subsequently drilled 167 m east of Hole 794C.

Igneous Rocks

During Leg 127 drilling in Holes 794A, 794B, and 794C (645.6 mbsf, total depth), scientists recovered an excellent Miocene to Holocene sedimentary sequence and cored the underlying igneous complex, as summarized in the "Background and Scientific Objectives" section (this chapter). During Leg 128, we drilled Hole 794D without sampling the sedimentary column with the aim of penetrating farther into the igneous complex and of preparing this hole for later installation of a downhole seismometer in the basement rock. Coring in Hole 794D commenced at 573 mbsf within the igneous complex, purposely overlapping and duplicating a portion of the same sequence cored in Hole 794C.

The lithologic sequence cored in Hole 794D is predominantly igneous rock with recovery of only a single, thin (1.6-m), sedimentary interbed. An average recovery rate of only 21.7% precluded continuous description of the igneous sequence. However, logging data materially aided us to recognize lithologic boundaries, and also indicated that unsampled portions of this sequence may include marine sediments and/or weathered zones between the igneous flows and sills. Shipboard analysis and interpretation of diagnostic mineralogy and texture, XRF data, preliminary paleomagnetic data, and logging data from this sequence allowed us to recognize nine hard-rock lithologic units as follows:

Unit 1 (573.0–589.4 mbsf)

This unit consists of plagioclase-pyroxene, phyrlic, leucocratic dolerite. This rock is a dark greenish gray dolerite characterized by abundant, uniformly distributed phenocrysts of plagioclase. Alteration is moderate (15%–20%). Top and bottom contacts were not observed.

Unit 2 (595.4–596.1 mbsf)

This unit is doleritic basalt; dark green, massive, dense, vesicular, and highly altered (65%). No contacts were observed, although fracturing is evident.

Unit 3 (604.6–604.9 mbsf)

This unit is aphyric dolerite; dark green, massive, and nonvesicular. Alteration is moderate to high (45%). No contacts were observed, but slickensided fractures are present.

Unit 4 (619.0–642.7 mbsf)

This rock is aphyric to olivine microphyric dolerite; medium gray to greenish with pale green mottling, massive and dense, and has an intergranular to interstitial texture. Vesicles are rare to uncommon. Grain size of the groundmass decreases toward the bottom of the unit, indicating close proximity to the bottom contact, which was recovered; the top contact was not observed. Alteration of the rock is high (50%–60%), and fine fractures are common.

Unit 5 (642.7–643.9 mbsf)

This unit is tuffaceous, clayey siltstone with foraminifers; dark gray to dark brown. The entire unit is bioturbated with only crude bedding preserved. Foraminifers are extensively dissolved and hence are not indentifiable; scarce nannofossils and centric diatoms also are present. Vitric debris are hydroclastic shards deposited in a crude layer and dispersed in silty clay. Baked contacts are conspicuously absent, but contact zones record substantial shearing and brittle deformation.

Unit 6 (643.9–655.0 mbsf)

This rock is olivine-pyroxene, microphyric basalt; medium gray, massive, dense, and vesicular. Vesicles range from 0.3 to 8 mm, are partly unfilled, and become rare at depth. Alteration is high (50%–62%) and includes traces of pyrite. The upper or top contact of the unit was not recovered; overlying sediment (Unit 5) exhibits no evidence of heating, hence Unit 6 has been interpreted as a lava flow on the seafloor; the bottom contact was not observed. A few filled fractures are present.

Unit 7 (660.7–680.5 mbsf)

The rock is aphyric dolerite; dark grayish green and massive. Alteration is moderate to high. No contacts were observed. Frequent variations of grain size may be the result of flow differentiation.

Unit 8 (689.3–708.3 mbsf)

This unit varies aphyric basalt; from fine- to coarse-grained toward the bottom, with ovoid vesicles (0.1–1 mm) in the upper part of the unit. This part of the unit has been highly altered (60%–70%). No contacts were found, but the uppermost rock exhibits evidence of severe quenching and other evidence points to

the proximity of the upper contact. Numerous, filled fractures and veins are present, some with slickensides.

Unit 9 (717.1–727.1 mbsf)

This rock is olivine dolerite; dark greenish gray with a fine to medium grain size. It is massive and has no vesicles. No contacts were observed. Rare filled and bordered fractures are present.

In addition to the nine units recognized in Hole 794D, a tenth unit, here called Unit 0, was cored at the base of the sediment column in Hole 794C (Tamaki, Pisciotto, Allan, et al., in press) and represents the shallowest and youngest dolerite sill in the igneous complex beneath Site 794.

The coarser textures of the basaltic lavas indicate that they erupted at medium-to-great water depths into the upper part of a soft sediment pile. In contrast, the medium- to fine-grained dolerite sills (Units 1, 3, 4, and 9) probably were intruded under a thicker cover after the basaltic outpouring. Significantly, no sediments were found below Unit 6, although logging suggests that either sediment or altered igneous rock may be present between igneous units in the lower part of the sequence. The abrupt changes in concentrations of trace elements (niobium/zirconium, zirconium/yttrium, and barium/yttrium) at the top of Unit 6 and the development of hydrothermal mineralization in Units 6 through 9, collectively indicate that two different volcanic complexes are represented within this sequence that involve (1) a lower complex consisting of Units 6 through 9 and (2) an upper complex or series consisting of Units 0 through 4. Moreover, various plots of incompatible elements (barium, niobium, zirconium, and yttrium) in these rocks clearly separate them into two groups corresponding to two distinct magmatic series, which in turn corresponds to two volcanic complexes: (1) an upper and younger set of sills and flows of probable island-arc tholeiite composition (Units 0, 1, 2, 3, and 4) and (2) a lower and older sequence tentatively interpreted as ocean floor basalts of back-arc tholeiite composition (Units 6, 7, 8, and 9). Unit 6 appears to represent the most primitive magma within the lower series of basalts, with stratigraphic and textural evidence to indicate that this rock was extruded onto the early Miocene(?) floor of the Yamato Basin. Hence, we interpret the upper surface of Unit 6 as the top of igneous basement at this site.

Note that the superposition of island-arc tholeiites over back-arc tholeiites is inconsistent with the perceived normal magmatic evolution of a back-arc area. One possible explanation for this irregular order is that the lower volcanic complex may represent a remnant of the initial magmatic activity of an immature magmatic arc generated from a depleted upper mantle. We hope that further chemical and isotopic analysis will resolve these apparent inconsistencies in magma provenance. No matter what their provenance, both volcanic complexes were emplaced successively and rapidly within the same tectonic context.

Shipboard analysis of fracture patterns and veins and the nature of vein-filling materials and alteration halos within the Site 794 igneous basement complex provide additional insights into the geochemical and tectonic history of these rocks. The fractures fall into two groups or sets: a gently dipping set and a steeply dipping set. Geometry of the gently dipping fractures and veins suggests that they originated as conjugate shear joints (or faults) during a north-northwest to south-southwest compressive phase. The steeply dipping fractures cut across the gently dipping veins and may be younger features; their orientation suggests that an east-west extensional phase was responsible for their initiation. Analysis of the processed Formation Microscanner (FMS) logging record is expected to enhance fracture analysis in that portion of the sequence where this logging tool was run successfully.

Age

As noted earlier, sediments immediately above and intruded by the shallowest dolerite sill (Unit 0) in Hole 794C have been assigned a late early Miocene age (ca. 15.8–16.5 Ma) by Tamaki, Pisciotto, Allan, et al. (in press), fixing a maximum age for the upper portion of the igneous complex as late early Miocene. Unfortunately, foraminifers, diatoms, and radiolarians found in the tuffaceous marine sediments forming Unit 5 of the Hole 794D sequence have been so badly altered and recrystallized that they cannot be used to establish a precise biostratigraphic age for this material. Two species of diatoms, identified in Unit 5 sediments,

Thalassionema nitzschoides and *Coscinodiscus curvatulus*, have Neogene to Holocene ranges that together with the stratigraphic position of this unit and oldest age estimated for the base of the sediment column at this site are consistent with an early to middle Miocene age. All microfossils present in Unit 5 sediments indicate that deposition occurred in a normal, open ocean, and deep bathyal environment.

Paleomagnetic analysis of rocks cored in Hole 794D yielded stable inclinations and natural remanent magnetization (NRM) intensities in Units 1, 2, 4, and 6 through 9. Six of these seven units exhibit negative inclinations. The average period of Miocene polarity events is about 300,000 yr, which suggests that the volcanic activity responsible for the Site 794 igneous sequence occurred within a few hundred thousand years. Alternatively, if this activity encompassed more than one million years, then a middle to early Miocene age is likely, given the extended period of reversed polarity established between about 15.3 to 16.2 Ma (Berggren et al., 1985).

Good paleomagnetic and biostratigraphic age control within the Miocene through Holocene sediments overlying the igneous complexes at Site 794 indicates that the rate of sedimentation in this area ranged from 54 to 29 m/m.y., with an average sedimentation rate of about 37 m/m.y. during late early to early middle Miocene time (Tamaki, Pisciotto, Allan, et al., in press).

Logging

Poor hole conditions in Hole 794D restricted logging to only one run (using the seismic stratigraphic combination of logging tools) between 560.0 mbsf (base of the cased hole) to 733.5 mbsf (total depth of Hole 794D). The FMS obtained high quality data from 560 to 596 mbsf and provided the means to constrain the number and thicknesses of the sills and flows that comprise the igneous complex cored at this site.

Eight volcanic units can be defined on the basis of responses to the Natural Gamma-Ray Spectroscopy Tool (NGT) and when combined with data from the resistivity log, Units 5, 7, and 8 can be subdivided further into smaller subunits. In addition, sedimentary layers and/or zones of altered volcanic rock can be identified from the trace of the Gamma Ray log (GR) because of the higher contents of uranium, thorium, and potassium of these materials relative to those of the igneous rocks. Although sediment was recovered from only one interval in this sequence (Unit 5), logging data suggest sediments and/or altered volcanic rock may be present in unsampled gaps elsewhere in this sequence.

Finally, one should note that the limited FMS record in Hole 794D shows a remarkable amount of detail along the borehole wall, including images of cumulate layering and orientation of infilled veins and fractures on a centimeter scale, with further detail anticipated after processing of this record.

Geophysical Experiments (Downhole Seismometer)

A downhole seismometer was installed in Hole 794D at 714.5 mbsf in the lowermost igneous basement section. The seismometer is equipped with three-component, feedback-type accelerometers having the same basic design as the state-of-the-art seismographs used in global seismic networks. Sensitivity was compromised to make the seismometer package more rugged and to make it fit through the drill pipe (diameter of <100 mm) at installation. A leveling mechanism was added to the horizontal sensors so that an instrument-package tilt of up to 5° could be accommodated. The output from each component was amplified in two gains because the A/D converter is limited to a dynamic range of 16 bits. The high-gain channel has a sensitivity of about 10^{-8} m/s² between 100 s and 30 Hz, while the low gain has a sensitivity of about 5×10^{-8} m/s² between DC and 30 Hz. These six-channel data are relayed digitally at an 80 Hz/channel sampling rate uphole via the seven-conductor logging cable that is normally used for ODP logging operations.

Installation was performed without major difficulties. The instrument was clamped in the hole using a single-arm extension pad. Drill pipes were extracted after cutting the cable at the rig floor. A real-time, continuous recording was made in the *JOIDES Resolution* Underway Geophysics laboratory after the cable was re-connected by torpedo splicing. The support vessel *Tansei-maru* of the University of Tokyo Ocean Research Institute installed an array of nine OBSs for the controlled-source (air guns), seismic

refraction experiment. One type of OBS was a digital recording that was deployed above the downhole seismometer to compare waveforms. The *Tansei-maru* subsequently shot two concentric circles having diameters of 10 and 20 nmi around Hole 794D and two straight lines in the N60°E and N30°W directions to study the detailed seismic structure, taking lateral heterogeneity and anisotropy into account. The records obtained also will be used for orienting the horizontal sensors. However, one horizontal sensor failed to yield meaningful output, possibly due to the failure of leveling. A real-time recording was made for about 58 hr, whereas air-gun shooting lasted for 48 hr.

The downhole seismometer system was designed to be used for long-term observation as well. Another supporting vessel, the *Kaiko-maru-5*, chartered by the University of Tokyo Ocean Research Institute, brought the seafloor recording unit, the battery power supply, and the retrieval unit to the site. After the *JOIDES Resolution* passed the end of the re-headed logging cable to the *Kaiko-maru-5*, these units were deployed. The seafloor recorder has 60 megabytes (Mbyte) of digital data storage. The recording is basically event-driven, and detection was made by monitoring the ratios of the short-term average (STA) and the long-term average (LTA) of the signals. However, time-window recording has also been programmed because the broad-band seafloor noise spectrum is unknown. Although the digital data reach the seafloor at a rate of 80 Hz/channel, present technology limits recording to 20 Hz/channel and 1 Hz/channel for each event. Another constraint is the available power supply, which at present limits recording time to a only a few months. Deployment was completed successfully at 0020UTC, 30 September 1989.

Oblique Electrical Resistivity Experiment

Dedicated Hole 794E was drilled for the electrical resistivity experiment near the point where we had performed the real-time seismic experiment from the *JOIDES Resolution*. This experiment was designed to obtain the structure of the electrical resistivity to a depth of about 10 km. This scale required us to conduct an "active" experiment using an artificial source and to observe signals from within the drilled hole. After the seismic instruments were deployed from the *Kaiko-maru-5*, the ship was prepared to place electrical currents into the water. Each observation involved injecting an electrical current of 20 A into the water column via a seafloor cable with 100-V difference between the sea surface and the seafloor. The change in the electrical field induced by this charge was recorded on board the *JOIDES Resolution* via the electrical cable in Hole 794E, with five electrodes arranged at five depths in the hole. Because the signal-to-noise ratio was small, the source signal was repeated so as to allow for stacking of observations. This sequence was repeated at distances of 1, 2, 4, and 7 km from Hole 794E in two directions, N60°E and N30°W. The greater the distance between the source and point of measurement, the deeper the resistivity structure is probed. Measurements were conducted in two directions to obtain an anisotropic effect. These two directions used were chosen specifically from the standpoint of the regional tectonic setting. Successful measurements were performed for a 24-hr period and the experiment was completed on 1 October 1989. Interpretation of the data produced by this experiment will require post-cruise processing. When integrated with previous measurements using passive natural sources, these data should yield a higher resolution perspective of resistivity at depth over a range of 300 km in the Japan Sea, Japan arc, and Japan Trench area.

BACKGROUND AND SCIENTIFIC OBJECTIVES

Background

Multiple Occupation and Drilling at Site 794

Site 794 (proposed Site J1b) in the northern Yamato Basin had been scheduled to be visited twice during ODP drilling in the Japan Sea. Initial occupation of this site was to take place during Leg 127, when three holes were to be drilled (1) to meet the primary objective of determining the nature and age of basement rock, (2) to recover a complete sedimentary se-

quence from the northern Yamato Basin, (3) to analyze *in-situ* crustal stress, and (4) to case and prepare one hole to be reentered during Leg 128 for geophysical experiments. Holes 794A, 794B, and 794C were successfully drilled during Leg 127, with recovery of a 543-m-thick, Miocene through Quaternary, sedimentary sequence and coring of underlying igneous rocks to a depth of 653.7 mbsf (Tamaki, Pisciotto, Allan, et al., in press). However, a stuck BHA in Hole 794C precluded our analyzing *in-situ* stress and completing the hole preparation for reentry during Leg 128. This event led to a revised schedule for Leg 128, with the following new objectives: (1) to attempt to fish for the stuck BHA in Hole 794C or to drill and case a new hole into igneous basement for the planned geophysical experiments and (2) to accommodate a pre-planned rendezvous at Site 794 with two supporting vessels from the University of Tokyo Ocean Research Institute that had been scheduled to assist with the geophysical experiments at this site. As it turned out, the logistics of drilling and geophysical experiments during Leg 128 ultimately required two visits to Site 794 and two visits to Site 799 (see "Site 799" chapter, this volume) in order to accommodate this schedule. Two holes were drilled at Site 794 during Leg 128 (Holes 794D and 794E).

Because Site 794 was occupied during both Legs 127 and 128 and because drilling objectives at this site were similar, we have freely drawn on the unusually complete Site 794 "Background and Objectives" section in the *Initial Reports* volume of Leg 127 (Tamaki, Pisciotto, Allan, et al., in press) while writing this background review of Site 794; consequently, there has been some duplication of figures and text with the latter report. We have also included summaries of the sedimentary and igneous sequences recovered during Leg 127 drilling at Site 794, both for completeness and on the assumption that not everyone reading this volume will have simultaneous access to the *Initial Reports* volume of Leg 127.

Location and Bathymetry

Site 794 is located in the northeastern Yamato Basin about 130 and 150 km west of the Oga Peninsula and northern Honshu, respectively (Fig. 1). This northernmost reach of the Yamato Basin is sometimes referred to as the Yamato Trough because of the narrow configuration of the basin between the Yamato Rise and northern Sado Ridge (Inoue and Honza, 1979). The site is positioned on a gentle northward-dipping slope at the base of the northernmost extension of the Sado Ridge. Water depth at Site 794 is 2811 m (Hole 794A). This area of the Yamato Basin is somewhat shallower than the abyssal plain of the basin to the south, which averages about 3000 m deep (Inoue and Honza, 1979; Tamaki, 1988). The difference in depth results primarily from the rapid progradation of coarse terrigenous sediment onto the floor of the northern Yamato Basin via the Toyama Trough and submarine fan complex (Bouma, 1975). The Site 794 area is partially protected from this process by the Meiyo-Daisan Seamount, the northernmost peak of the Yamato Seamount chain (Fig. 1). Another conduit of turbidite deposition, the Mogami Channel, is separated from Site 794 by the northern Sado Ridge to the east. The Mogami Channel currently funnels coarse debris directly to the Japan Basin, but may have delivered sediments to the Yamato Basin prior to the Quaternary uplift of the Sado Ridge (Sakurai and Sato, 1971).

Crustal Structure

No modern seismic refraction data are available in the immediate vicinity of Site 794. However, refraction data of Murauchi (1966), sonobuoy data of Ludwig et al. (1975), and a

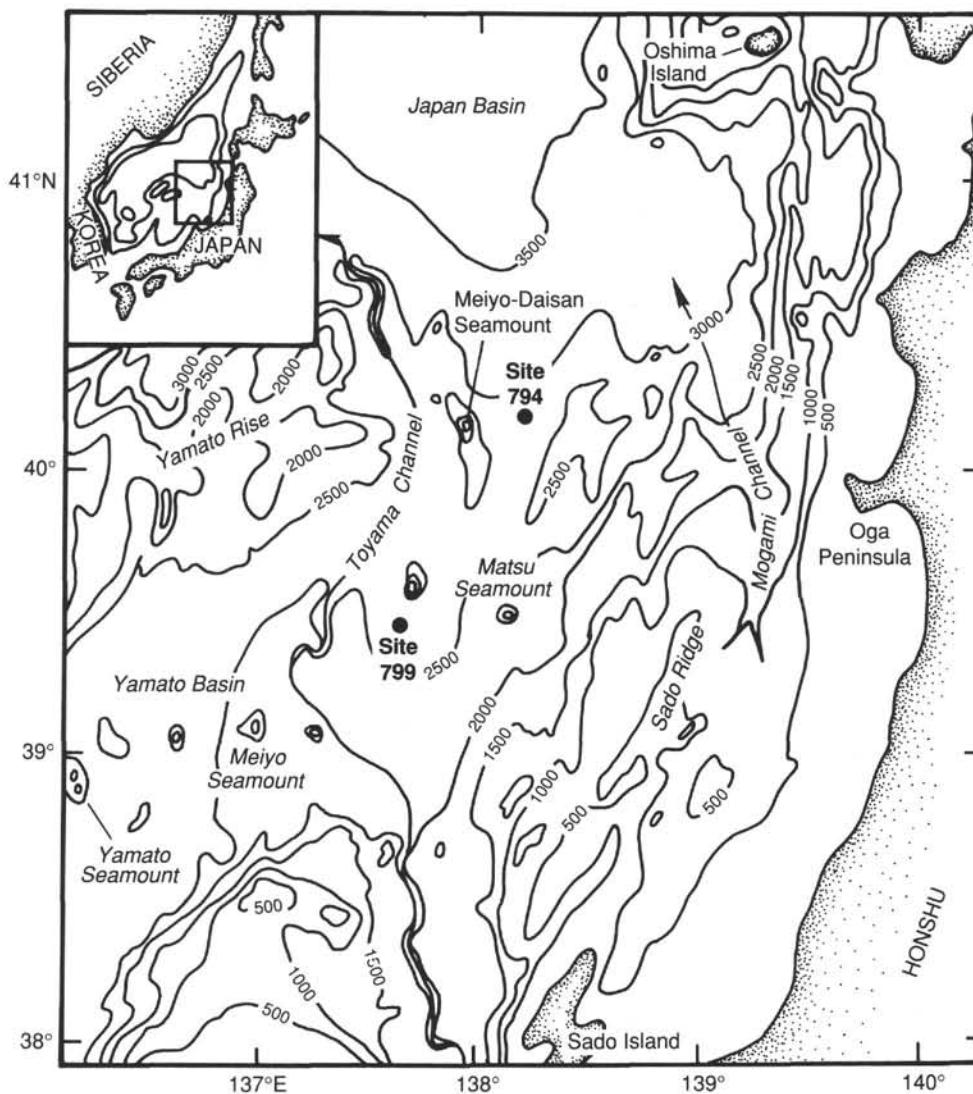


Figure 1. Location map of Site 794 and bathymetry of the northern Yamato Basin and adjacent Japan Basin. Contour interval = 500 m (modified from Tamaki, Pisciotto, Allan, et al., in press).

recent OBS refraction study in the southern Yamato Basin (Hirata et al., 1987; Katao, 1988) allowed us to construct and interpret a north-south crustal section along the axis of the Yamato Basin and into the adjacent northern Japan Basin, including the area of Site 794 (Fig. 2). These data illustrate the fundamental differences in crustal thickness between the two basins. The average depth to the crust/mantle boundary (Moho) beneath the Yamato Basin is 16 km below the seafloor (Fig. 2). In contrast, Ludwig et al.'s (1975) crustal velocity profile 143 indicates that depth to the Moho in the Japan Basin is only 8 km. Ludwig et al.'s refraction profiles 3 and 4, based on Murauchi's (1966) data, also allow one to compare the deep structure beneath the Yamato Basin with that under the adjacent shelf off northern Honshu (Figs. 2 and 3). An even larger crustal perspective is provided by an east-west cross section through the Japan Trench, Japan arc, and Japan Sea presented in Figure 4.

In short, the crust beneath the Japan Basin is oceanic in character, whereas the crust beneath the Yamato Basin is of intermediate or transitional thickness, when compared with typical continental crust that averages 35 km thick. The profile shown in Figure 2 also demonstrates that the so-called "layer-

3" or the "lower crust," defined by velocities of 6.5 to 6.9 km/s, is unusually thick beneath the Yamato Basin, whereas both "layer-3" and "layer-2" thin considerably beneath the Japan Basin. The distribution of velocities representative of sediments and sedimentary rock (1.6–2.8 km/s) indicate that "layer-1" is as much as twice as thick in the Japan Basin as it is in the Yamato Basin, possibly reflecting a difference in the ages of these two basins (Kobayashi, 1985; Tamaki, 1988).

Figures 1 and 2 clearly illustrate that Site 794 is situated at the topographic and geophysical juncture between the Yamato and Japan basins. Unfortunately, a critical gap in refraction data leaves the actual crustal configuration at this boundary unknown. However, the water depth at Site 794 (2807 m) implies a subsidence history indicative of the thickened crust of the Yamato Basin, rather than the thin oceanic crust of the Japan Basin.

Heat Flow

Measured values of heat flow in the northern Yamato Basin and adjacent Japan Basin average about 98 mW/m², with a range of 75 to 116 mW/m² (Fig. 5), based on measurements reported by Yoshii and Yamano (1983) and Tamaki (1988).

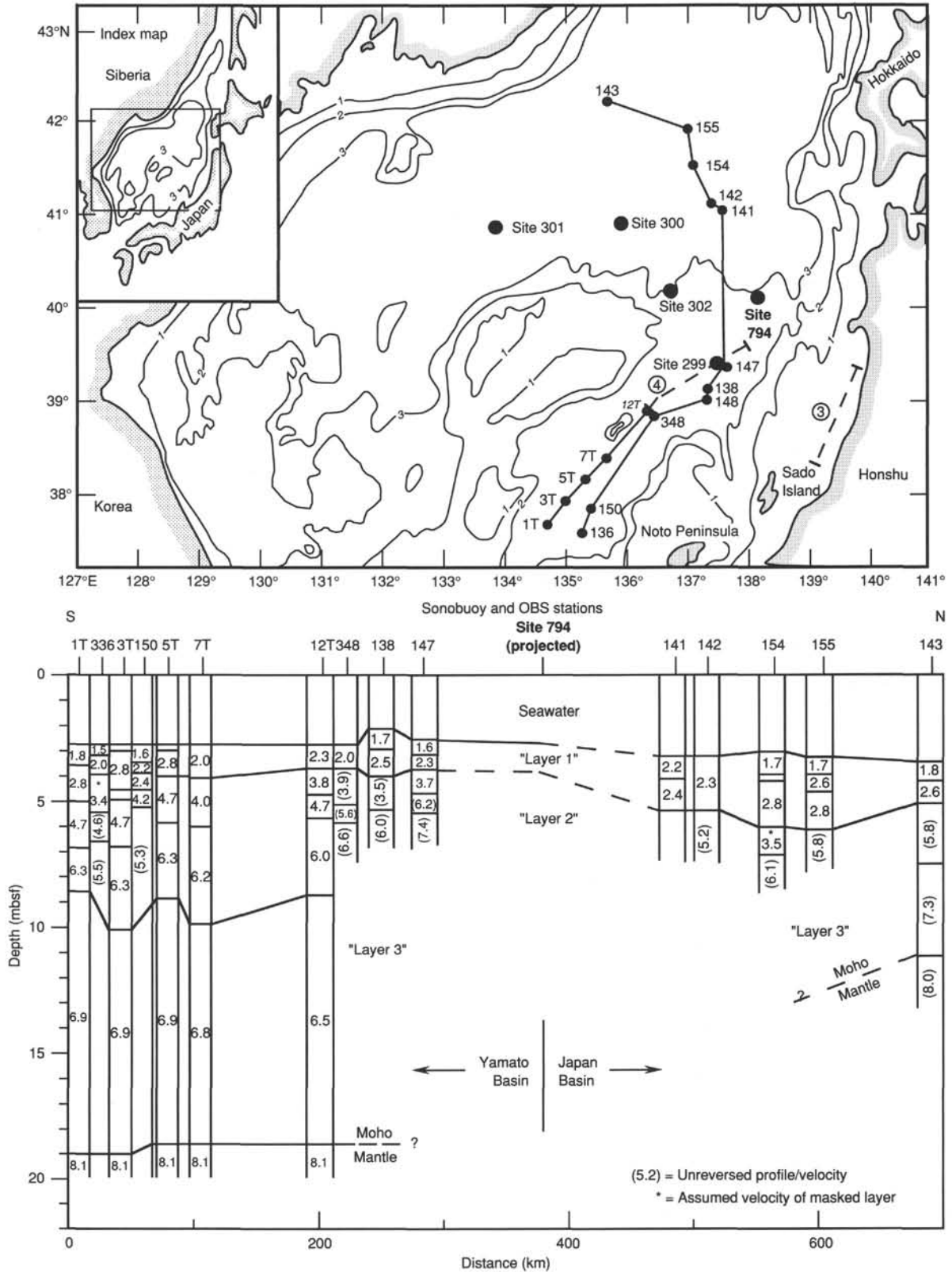


Figure 2. North-south profile of the crustal velocity through the Yamato Basin and northern Japan Basin. The upper map illustrates the location of sonobuoy and OBS stations used to constrain this profile. OBS stations are from Hirata et al. (1987) and are designated by the suffix T; other stations represent sonobuoy locations of Ludwig et al. (1975). Circled numbers and dashed lines mark two-ship refraction profiles of Murauchi (1966), presented by Ludwig et al. (1975), and illustrated in Figure 3. Bathymetric contours in kilometers below sea level. Figure modified from Tamaki, Pisciotto, Allan, et al. (in press).

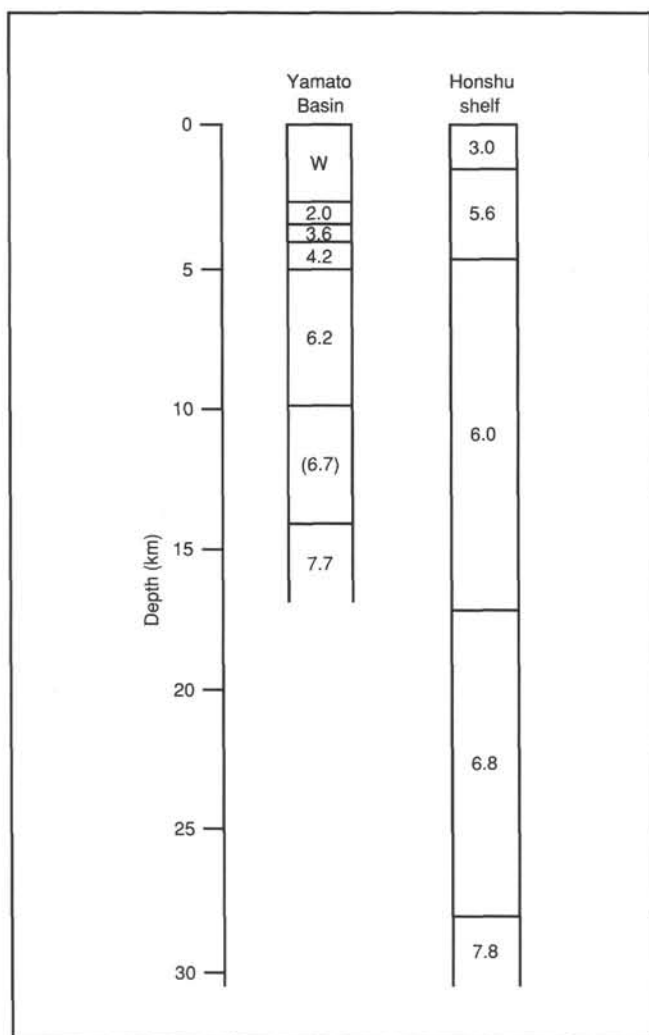


Figure 3. Profiles of crustal velocity beneath the Yamato Basin and northern Honshu shelf based on two-ship profiles and computed from end-to-end pairs and time-distance graphs, as presented by Ludwig et al. (1975); value in parenthesis represents a determination from a later arrival.

Lower values occur on highs in this area and the continental slope and shelf of northern Honshu, a trend that continues to the east under the Japan arc and into the Japan Trench area (Fig. 4).

Magnetics and Gravity

The pattern of magnetic anomalies in the area of Site 794 is complex and typical of most of the Yamato Basin and surrounding topographic highs. Anomalies display peak-to-peak amplitudes of up to 200 nT and wave lengths of about 50 km (Fig. 6). As noted by Tamaki, Pisciotto, Allan, et al. (in press), (1) the magnetic anomaly pattern just to the north of Site 794 in the Japan Basin consists of disrupted linear segments, similar to those found in areas of propagating spreading ridges (Hey, 1977; Tamaki et al., 1988) and (2) this change in anomaly character is essentially coincident with the apparent change from transitional to oceanic crustal thickness beneath the Site 794 area.

Free-air gravity anomalies in the vicinity of Site 794 do not display a distinctive pattern, although the distribution of anomalies over surrounding topographic highs mimics the shape of the seafloor (Fig. 7). The anomaly values in the

immediate area of Site 794 range from 0 to 20 mgal, which is higher than those in the deep abyssal plain area of the Yamato Basin to the south of this site.

Basement Rocks

Dredge hauls provided the only solid clues about the nature of basement rocks in the area of Site 794 prior to ODP drilling (Fig. 5). Rock samples collected from the Meiyō-Daisan Seamount due west of Site 794 surprisingly include lignite and siltstones of unknown age. Dredges from other seamounts in the Yamato chain have recovered volcanic rocks that included trachyandesites and basalts, which have yielded Miocene ^{40}Ar - ^{39}Ar dates of 10 to 16.9 Ma (Kaneoka et al., in press). Potassium-argon dates for andesites collected from Matsu, Hakusan-se, and Meiyō seamounts in this same chain range from 4.2 and 7.7 to 13.4 Ma, respectively (Ueno et al., 1971).

Tamaki et al. (1981) provided a geological map of the central Japan Sea that includes the area of Site 794. This map illustrates that volcanic basement rocks are present in areas both south and east of Site 794, including one site on the northernmost extension of Sado Ridge that yielded a Paleocene ^{40}Ar - ^{39}Ar age of 62 Ma for a rock of andesitic composition (Kaneoka and Yuasa, 1988; Fig. 5). In addition, a Cretaceous date (72 Ma) was derived from a welded tuff dredged from west of Oshima Island to the north of Site 794 along the western margin of Hokkaido (Figs. 1 and 5). However, most of the radiometrically dated, extrusive and intrusive igneous rocks collected from the western slope off Honshu yielded early Miocene ages that range from 22 to 24 Ma (Kaneoka and Yuasa, 1988). Early Miocene dates (ca. 23 Ma) also dominate radiometric ages derived from volcanic rocks dredged from the Yamato Rise on the western edge of the Yamato Basin (Tamaki, 1988), although one recent ^{40}Ar - ^{39}Ar analysis yielded a latest Oligocene age of 26.3 Ma (Kaneoka and Yuasa, 1988).

Onshore exposures of volcanic rocks in northern Honshu to the west of Site 794 include (1) Quaternary andesites, rhyolites, and dacites derived from arc volcanism; and (2) Oligocene and Miocene andesites, basalts, and rhyolites with a dominant middle to early Miocene age range (9–22 Ma). These latter rocks, along with associated lower Miocene volcanoclastic units and nonmarine terrigenous sediments, are generally included in the so-called “Green Tuff” formations (e.g., Monzen and Daijima formations and correlative units) that commonly occur at the base of Neogene sedimentary sequences throughout western Honshu.

The dominant ages of these volcanic rocks point to a major period of extrusive and intrusive igneous activity in the Yamato Basin region during early Miocene time. In fact, “Green Tuff” rocks apparently blanket underlying older basement rocks throughout onshore and offshore areas of the Japan Sea region and represent volcanism accompanying Oligocene-early Miocene rifting of the back-arc basin, including creation of the thickened crust typifying the Yamato Basin (Kobayashi, 1985; Fig. 2).

The upper portion of the sequence representing acoustic and igneous basement at Site 794 in fact was penetrated and sampled during the initial drilling at Site 794 during Leg 127. Shipboard analysis of these rocks (Tamaki, Pisciotto, Allan, et al., in press) resulted in their interpretation as a series of dolerite sills of probable early Miocene(?) age (Fig. 8), consistent with the speculative picture drawn from earlier studies of dredged and onshore basement rocks in this region (Tamaki et al., 1981; Tamaki, 1988). The following descriptions represent a summary of the six lithologic units recognized in the igneous basement sequence in Holes 794B and 794C, as presented by Tamaki, Pisciotto, Allan, et al. (in press):

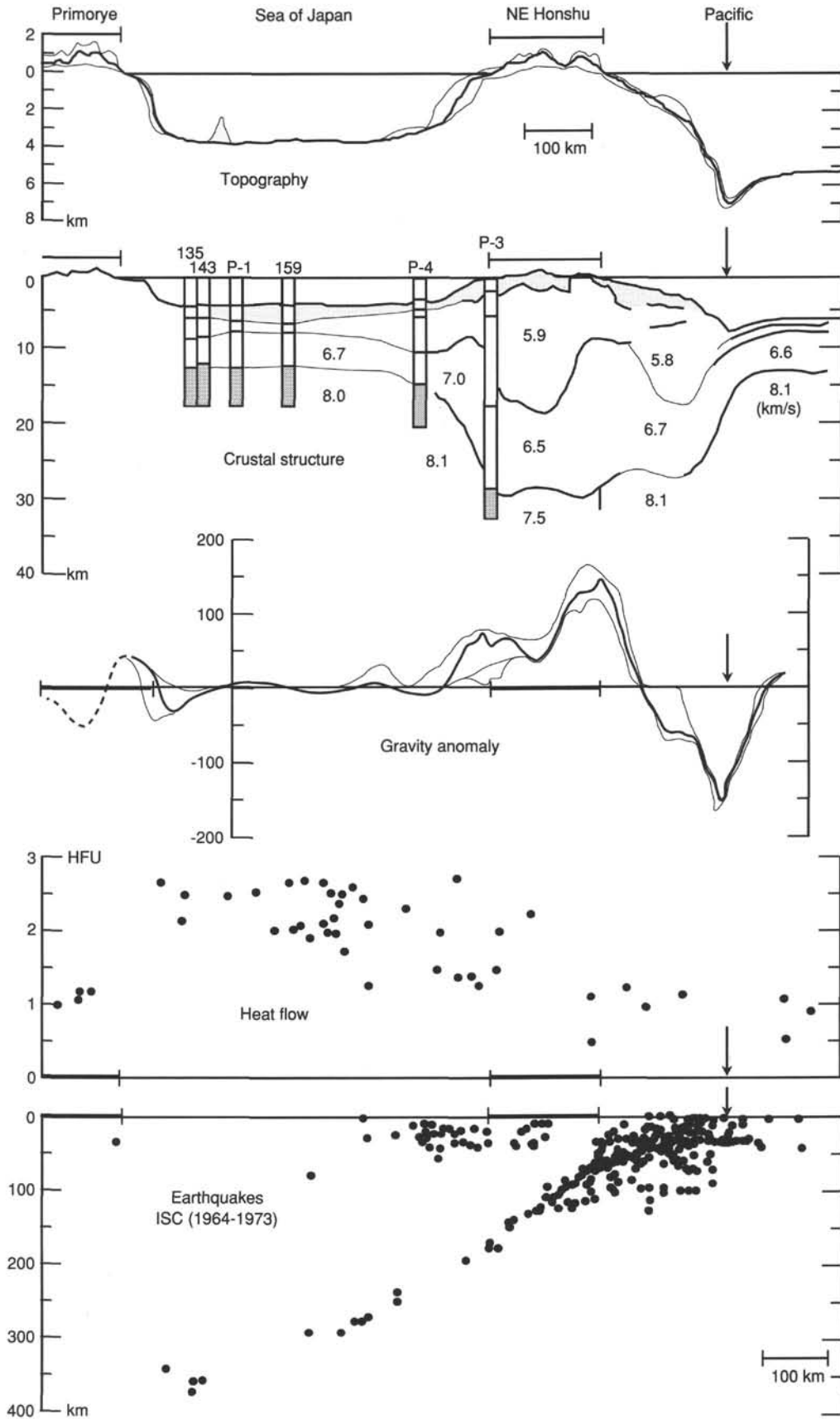


Figure 4. Regional east-west crustal section across the Japan Trench, Japan arc, and the Japan Basin, including refraction profiles 3 and 4 shown in Figure 3. Figure from Yoshii and Asano (1972), incorporating data from Yoshii (1972a, 1972b).

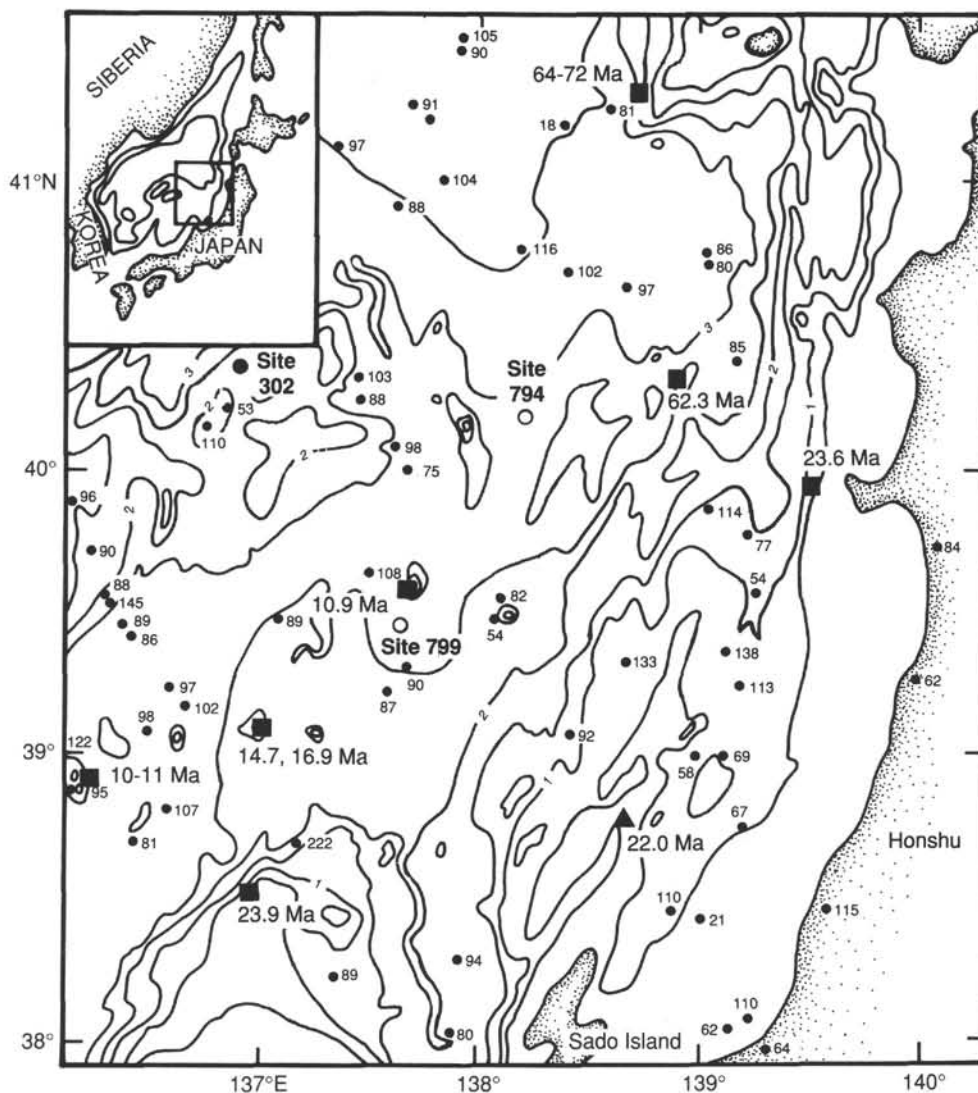


Figure 5. Location of heat flow measurements (mW/m^2) (indicated by closed circles) and radiometrically dated igneous rocks (Ma) in the general area surrounding Site 794. Filled squares represent volcanic rocks and filled triangles mark granites. ^{40}Ar - ^{39}Ar ages (Ma) are based upon ages analyzed and/or reported by Kaneoka (1986), Tamaki (1988), Kaneoka and Yuasa (1988), Ishii et al. (1988), Yamashita (1988), and Kaneoka et al. (in press). Bathymetric contours in kilometers. Figure from Tamaki, Pisciotta, Allan, et al. (in press).

Unit 1 (543–545 mbsf to 560 mbsf): Moderately plagioclase, phyrlic lerite. A horizontal contact was observed at the top of this unit, with a thin zone of baked clay sediment above and a chilled margin of moderately plagioclase, phyrlic basalt below.

Unit 2 (545–560 mbsf and 592–600 mbsf): Moderately to highly plagioclase, phyrlic dolerite. This unit is primarily massive and dense, with some highly fractured intervals.

Unit 3 (592–600 mbsf to 617–627 mbsf): Aphyric dolerite. This unit is moderately vesicular, massive, and highly fractured.

Unit 4 (617–627 mbsf to 629–633 mbsf): Aphyric dolerite. This unit is composed of massive, vesicular, medium- to fine-grained, aphyric dolerite. The upper half is highly fractured, whereas the lower half has few fractures.

Unit 5 (629–633 mbsf to 645–652 mbsf): Aphyric dolerite. This unit is highly vesicular. The lower boundary of the unit is sharply defined by a baked contact with tuffaceous sediments.

Unit 6 (645.6–651.7 mbsf): Aphyric to moderately plagioclase, phyrlic dolerite. The top of this unit is a chilled, intrusive margin against tuffaceous sediments.

Tectonic Setting

As discussed by Tamaki, Pisciotta, Allan, et al. (in press), Site 794 lies about 50 km west of the most active tectonic belt in the Japan Sea region (Fig. 9). The zone of north-south faults and folds marking this belt along the western margins of Hokkaido and northern Honshu is characterized by linear ridge and basin topography and by shallow seismicity (Tamaki et al., 1981; Seno and Eguchi, 1983; Tamaki and Honza, 1985; Tamaki, 1988). Seismic-reflection profiles across this zone suggest that many of these faults are thrust or reverse faults, often visibly expressed as seafloor escarpments and ridge flanks (Fig. 10). Reflection profiles also demonstrate that a

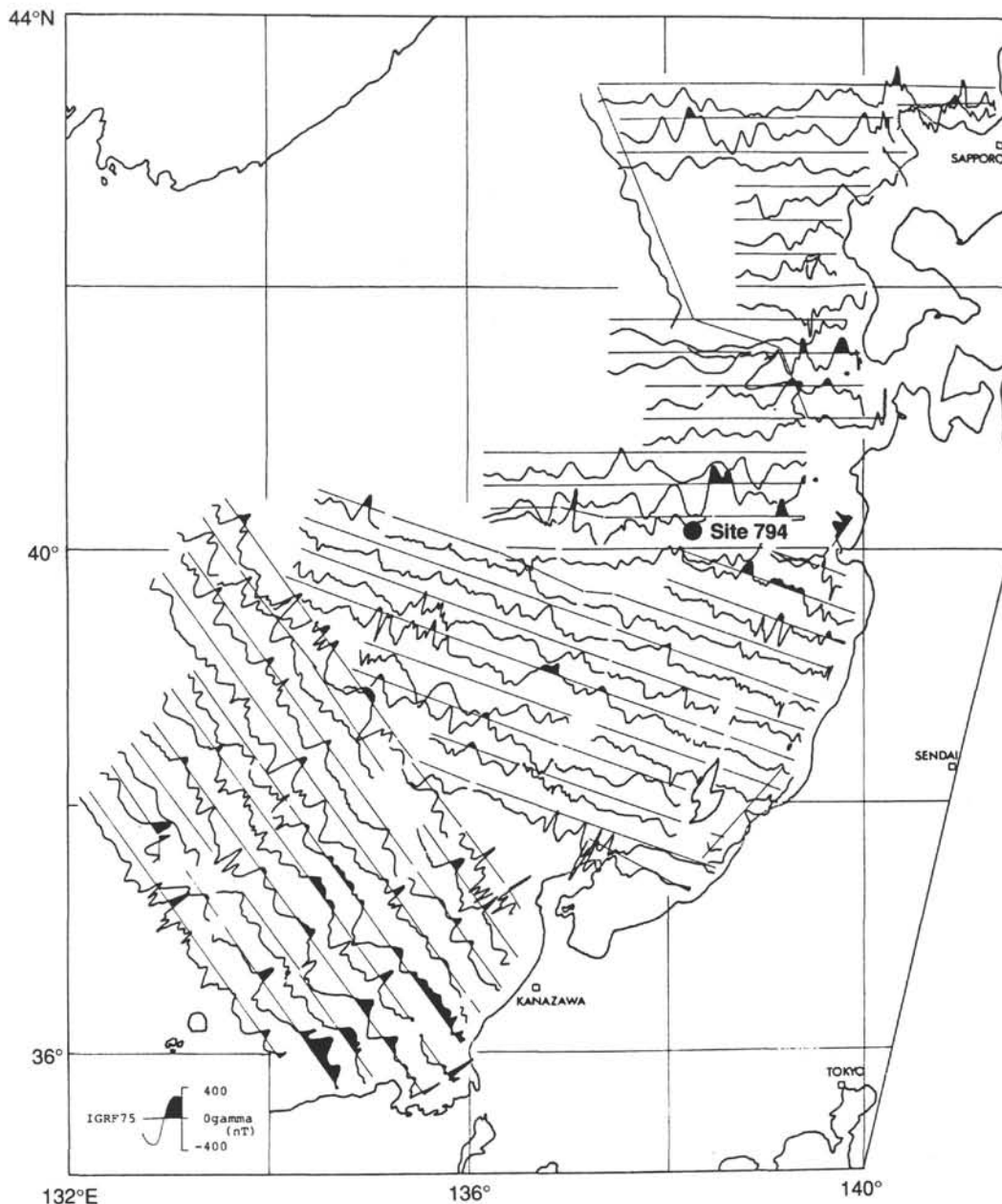


Figure 6. Magnetic anomaly patterns in the eastern Japan Sea and location of Site 794. Figure from Miyazaki et al. (1979).

number of these faults cut and displace acoustic basement in this region.

The distribution of shallow earthquake epicenters in the northeastern Japan Sea dramatically emphasizes the ongoing tectonic activity in the north-south Hokkaido-Honshu thrust belt (e.g., Fukao and Furumoto, 1975; Figs. 4, 9, and 10). More specifically, in 1983 an earthquake of 7.7 magnitude was inferred to have occurred on an eastward-dipping thrust fault only 50 km east of Site 794 (Tamaki and Honza, 1985; Fig. 10), with later analysis indicating a compressional mode for this event (Ishikawa et al., 1984). Other recent earthquakes in this region have also yielded focal-mechanism solutions that point to an active east-west to northwest-southeast compressional stress field in the northeastern Japan Sea (Ichikawa, 1971; Fukao and Furumoto, 1975).

Tamaki and Honza (1985) and Tamaki (1988) discussed the case for lithospheric convergence and ongoing compression

expressed by the western Hokkaido-northern Honshu thrust belt east of Site 794 (Figs. 9 and 10). Two major examples of this convergent process include the Sado Ridge to the east-southeast of Site 794, the Okushiri Ridge located north of this site, and Okishiri Island off the western coast of Hokkaido. Both of these topographic features are bound by steep thrust faults, and both underlying structures incorporate deformed Pliocene and Pleistocene sedimentary units, indicating that compression and uplift within this belt probably began during latest Pliocene time. Drilling at Site 796 on the Okushiri Ridge during Leg 127 confirmed this history (Tamaki, Pisciotto, Allan, et al., in press) and firmly dated the initiation of compressive uplift of this ridge as 1.8 Ma (e.g., near the Pliocene/Pleistocene boundary).

Other faults in the region surrounding Site 794 include an array of east to northeast-trending normal faults that cut the Yamato Rise and underlying acoustic basement (Fig. 1).

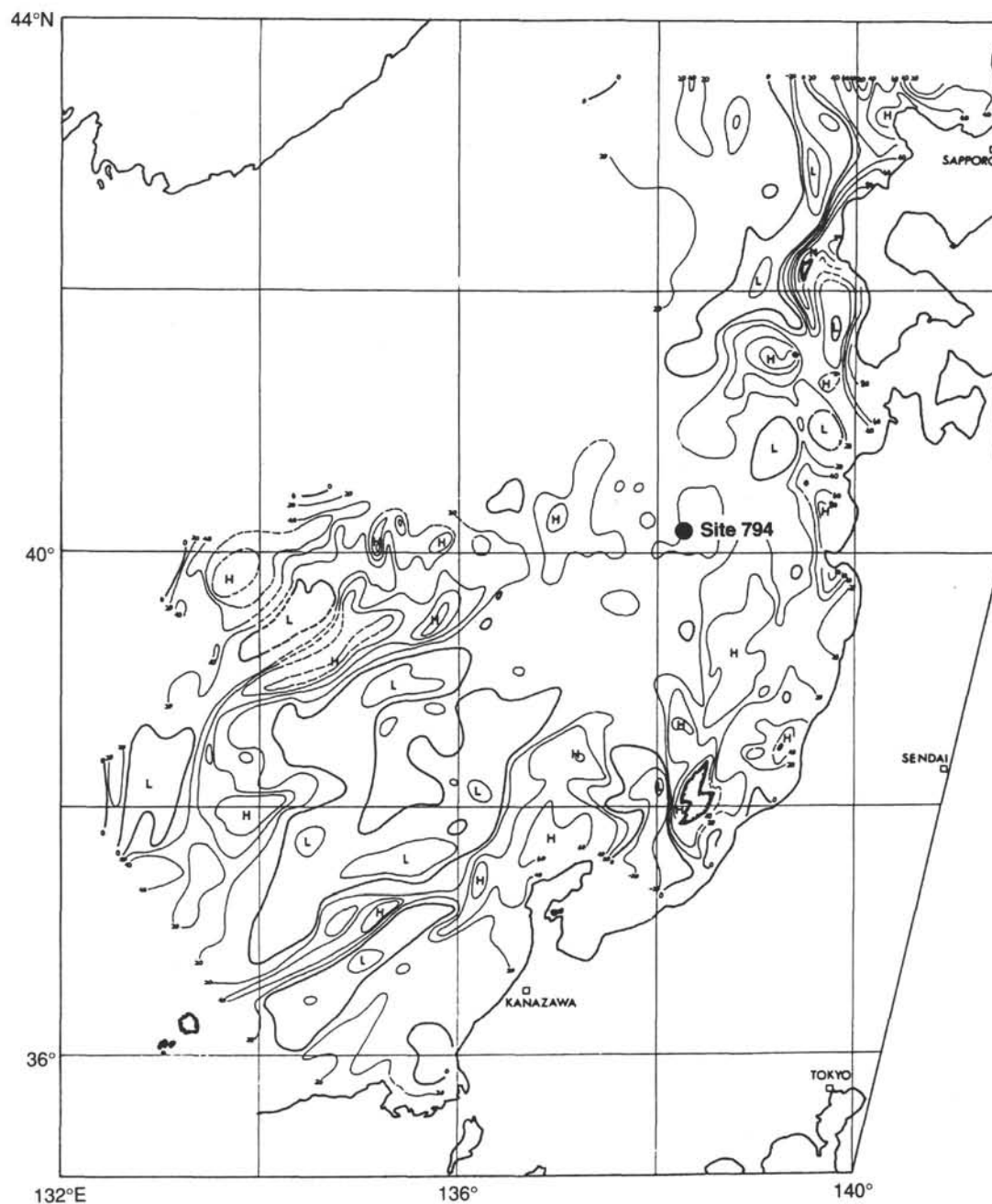


Figure 7. Free-air gravity anomalies in the eastern Japan Sea. Contour interval is 10 mgal. Figure from Miyazaki (1979).

However, no significant faults have been recognized in the immediate vicinity of Site 794 (Fig. 10), despite the location of this site over an area involving the juncture between oceanic and transitional crust and active compressional faulting 50 km to the east (Fig. 2).

Sedimentation

The sedimentary section overlying acoustic basement at Site 794 was originally estimated to range from 500 to 700 m thick on the basis of seismic-reflection data (Fig. 10). During the initial drilling at Site 794 for Leg 127, scientists found a composite section of 543 m of Miocene through Holocene sediments that overlay a series of dolerite sills in Holes 794A, 794B, and 794C (Fig. 8). Shipboard analysis of this sequence

allowed these scientist to divide the sedimentary column into the following six units, as described by Tamaki, Pisciotto, Allan, et al. (in press):

Unit I (0–92.3 mbsf; 0–3.0 Ma; Holocene to upper Pliocene): Clay and silty clay. The upper 63.8 m consists of alternating light bioturbated zones and dark laminated zones with common, thin, ash layers. The lower 28.5 m is similar to the upper interval, but has fewer dark zones. Diatoms increase down the section.

Unit II (92.3–293.5 mbsf; 3.0–8.1 Ma; upper Pliocene to upper Miocene): Diatomaceous ooze and clay. The upper 124.6 m consists of bioturbated and clayey oozes with sparse ash layers. Diatomaceous clay constitutes the lower 76.6 m.

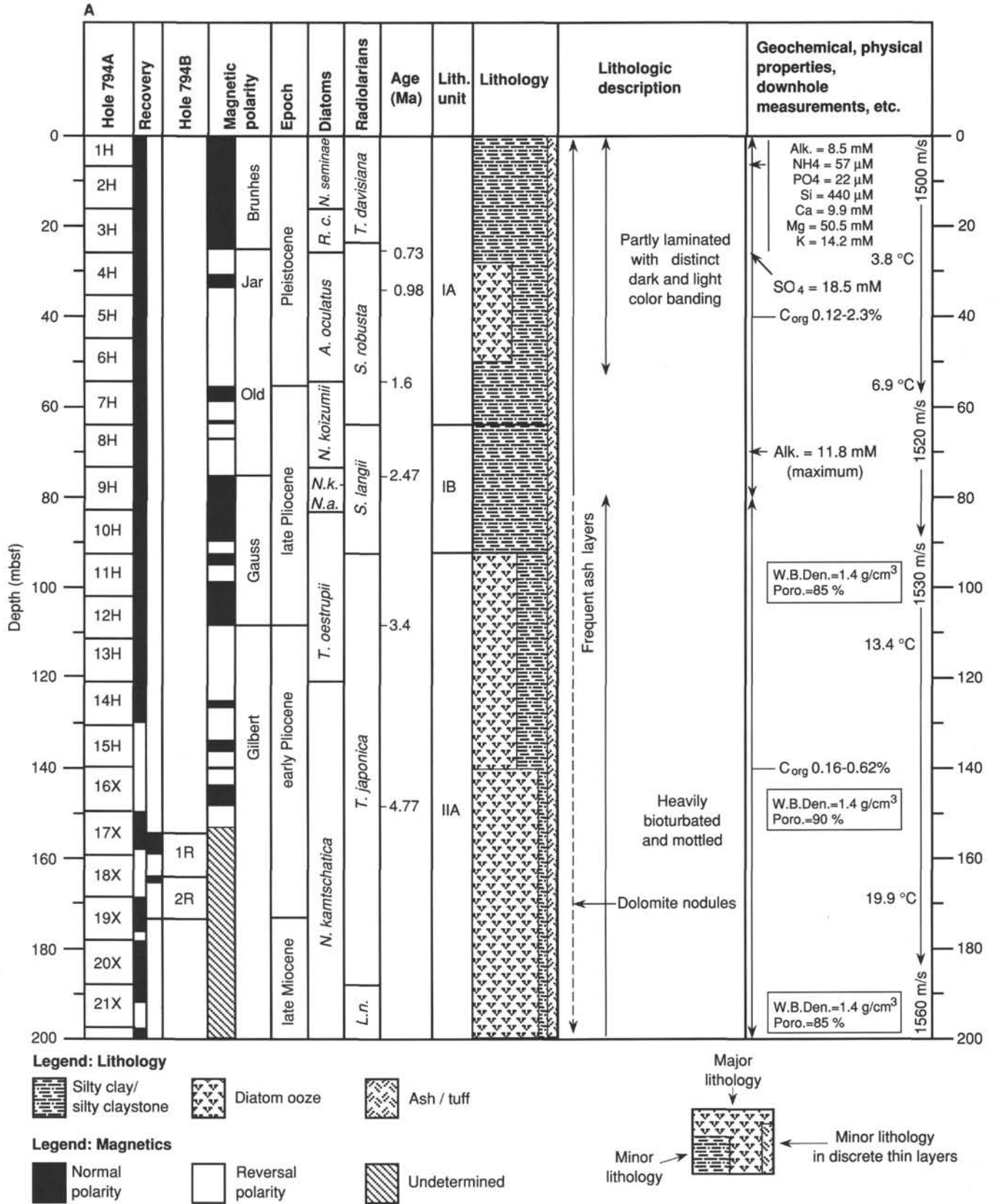


Figure 8. Stratigraphic summary column for Holes 794A, 794B, and 794C, drilled during Leg 127 (from Tamaki, Pisciotta, Allan, et al., in press).

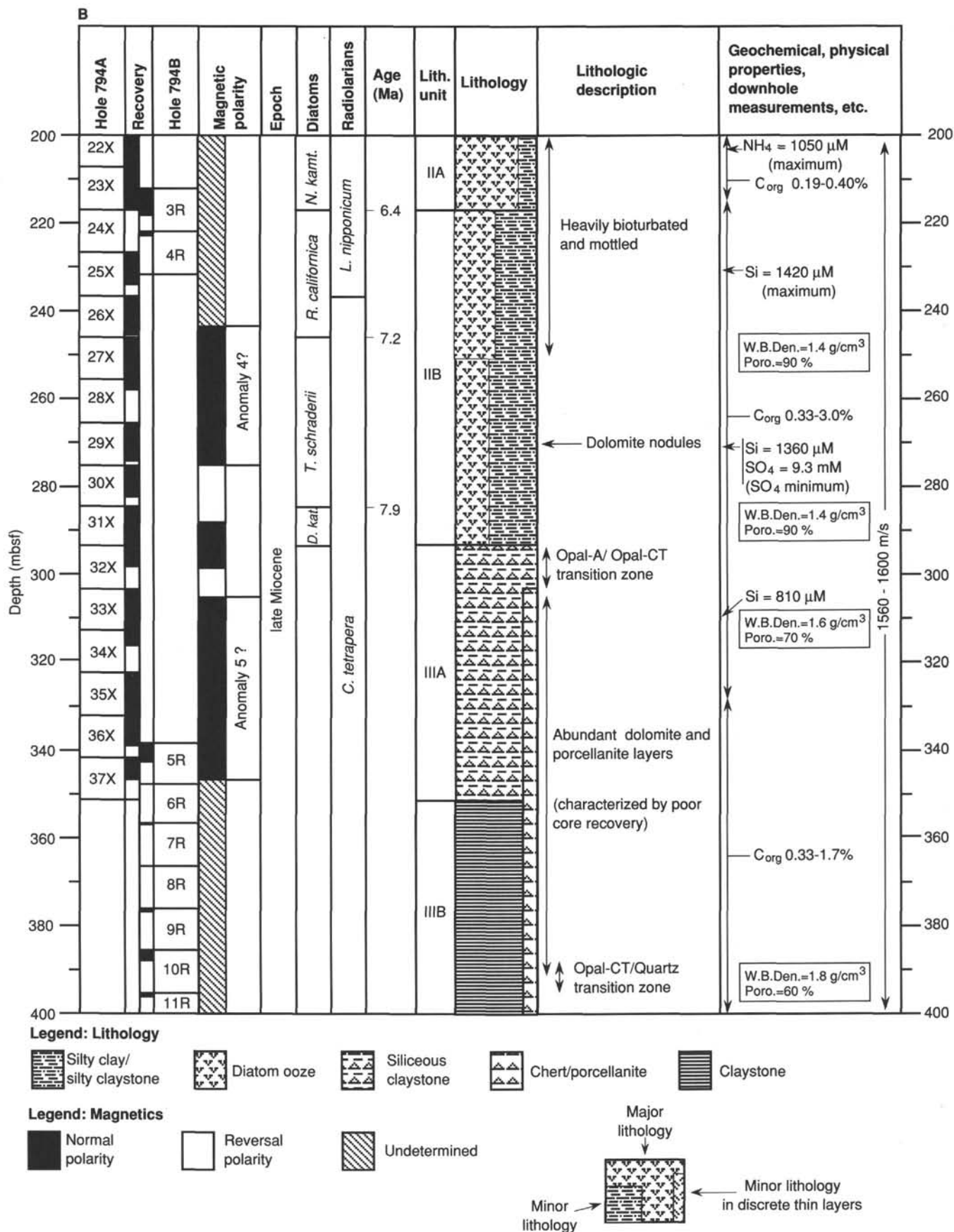


Figure 8 (continued).

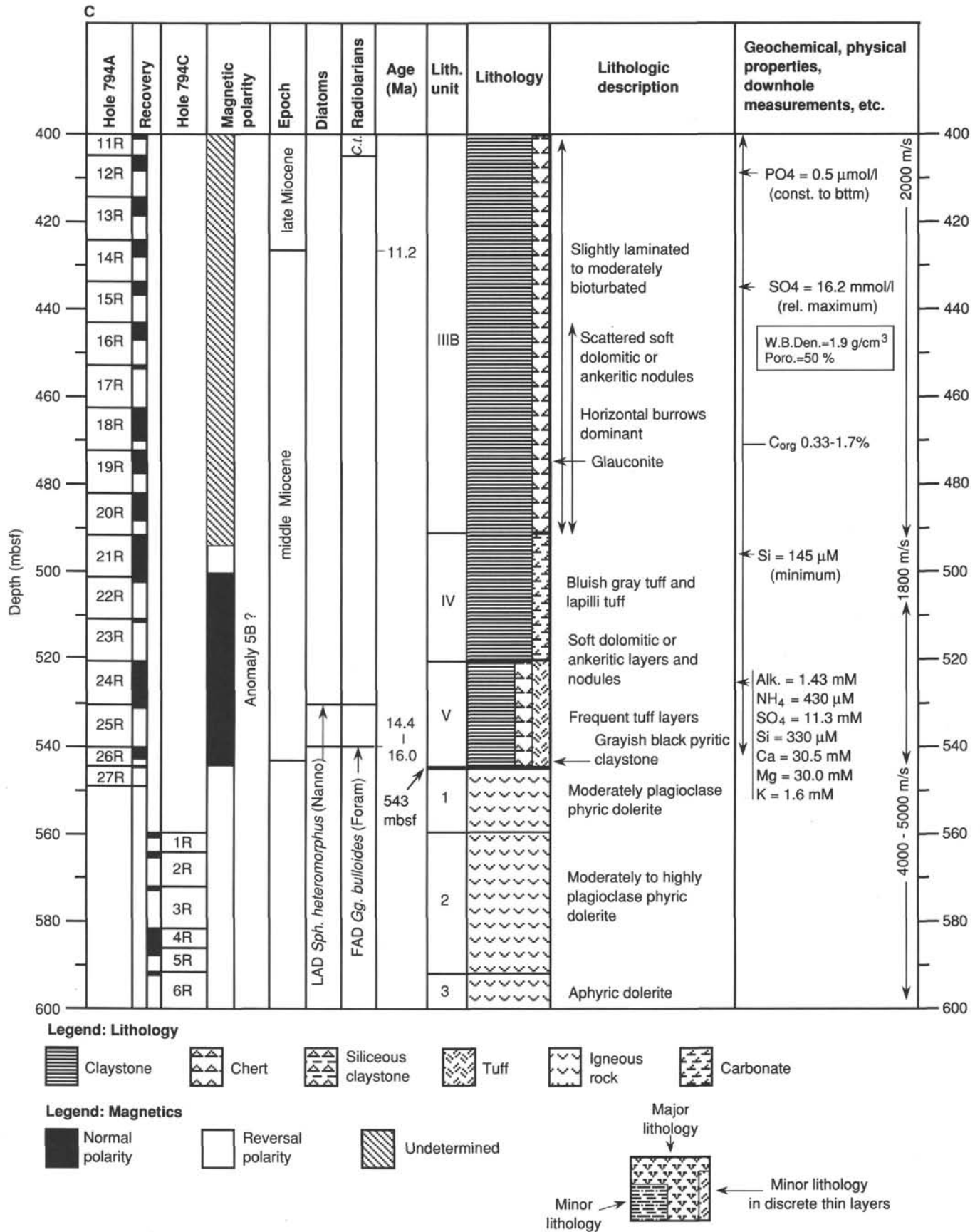


Figure 8 (continued).

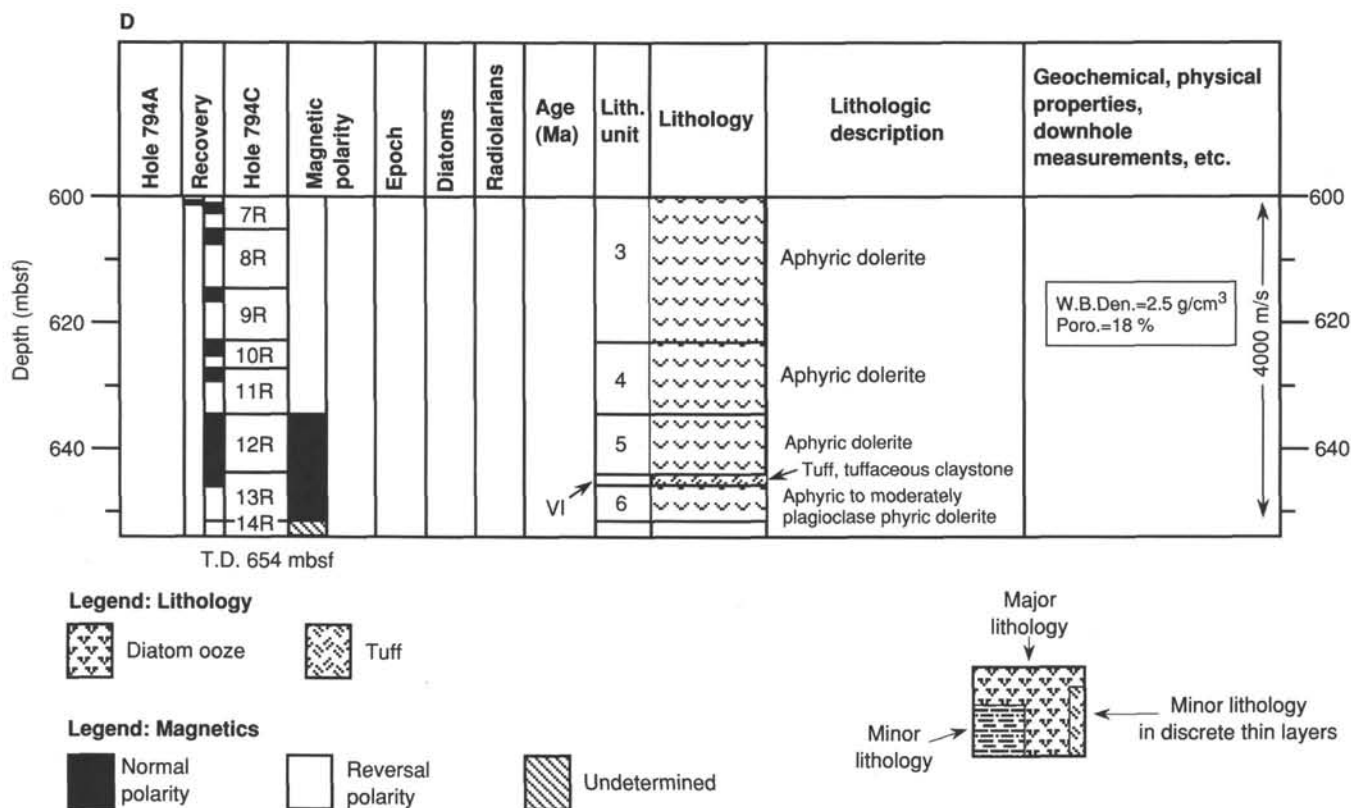


Figure 8 (continued).

Diatoms decrease and opal-CT cement increases in this interval.

Unit III (293.6–491.7 mbsf; 8.1–14.6 Ma; upper to middle Miocene): Clay and claystone. The upper 57.8 m is bioturbated clay and claystone with minor ash, pyrite, and micritic carbonate. The lower 140.3 m is bioturbated claystone with rare laminated intervals. Porcellanites occur at several levels, and dolomitic, sideritic, siliceous cements, and calcareous lenses are common.

Unit IV (491.7–520.6 mbsf; ~14.6–15.8 Ma; middle to upper lower Miocene): Tuff and claystone. This unit consists of interbedded and lapilli tuffs and claystone. Tuffs are variously thin- to thick-bedded, normal to inversely graded, and have sharp basal contacts. Some beds contain planar, convolute, and cross-laminations. Others contain burrowed intervals, are massive and poorly sorted, and have claystone fragments. Interbedded claystones are moderately bioturbated.

Unit V (520.6–543 mbsf; ~15.8–16.5 Ma; upper lower Miocene): Claystone. This unit consists of interbedded claystones of variable compositions with minor interbedded tuff. From top to bottom, silty claystone, claystone, and black claystone are the dominant lithologies. Minor thin intervals and lenses of glauconitic claystone, secondary carbonate, and pyrite also are present in these moderately bioturbated claystones. Sparse, thin tuff layers display cross-laminations and flame structures.

Unit VI (644.1–645.6 mbsf; age unknown): Tuff and tuffaceous claystone. This unit is separated from Unit V by 100 m of dolerite. It consists of bioturbated claystone and massive-to-laminated, fine-grained tuff. The tuff also exhibits convoluted laminations, small slump folds, normal size grading, and bioturbated tops.

The combined lithologic, geochemical, and paleontologic data from this sequence (Fig. 8) were interpreted by the Leg 127 Shipboard Party as representing a three-stage, depositional history for the Site 794 area of the Yamato Basin and involving the following sequence of events, as described by Tamaki, Pisciotto, Allan, et al. (in press):

1. A middle Miocene period characterized by bioturbated hemipelagic-claystones, gravity-flow tuffs, and minor glauconite, deposited at upper bathyal depths (~500 m) in suboxic waters on a slope or borderland ridge
2. Subsidence to lower bathyal depths (>1500 m) during late middle Miocene time and deposition of hemipelagic, diatomaceous sediments and increasing amounts of volcanic ash through the early Pliocene in cool, well-oxygenated waters; and
3. A late Pliocene to Holocene period during which diatomaceous sedimentation shut down, volcanic ash production increased, and oscillating climatic and tectonic activity conspired to produce interbedded, massive and laminated, hemipelagic sediments.

Scientific Objectives

As noted in the introduction to this section, Legs 127 and 128 had shared objectives but separate drilling responsibilities and programs at Site 794. Leg 127 scientists were responsible for the initial drilling at Site 794 for the purposes of (1) coring the sedimentary section, (2) penetrating igneous basement, (3) conducting packer/hydrofracturing experiments in basement rock along with observing stress using the borehole televiewer, and (4) preparing a cased hole to be reentered during Leg 128. Leg 128 scientists were originally scheduled (1) to replace a downhole seismometer and to conduct a real-time

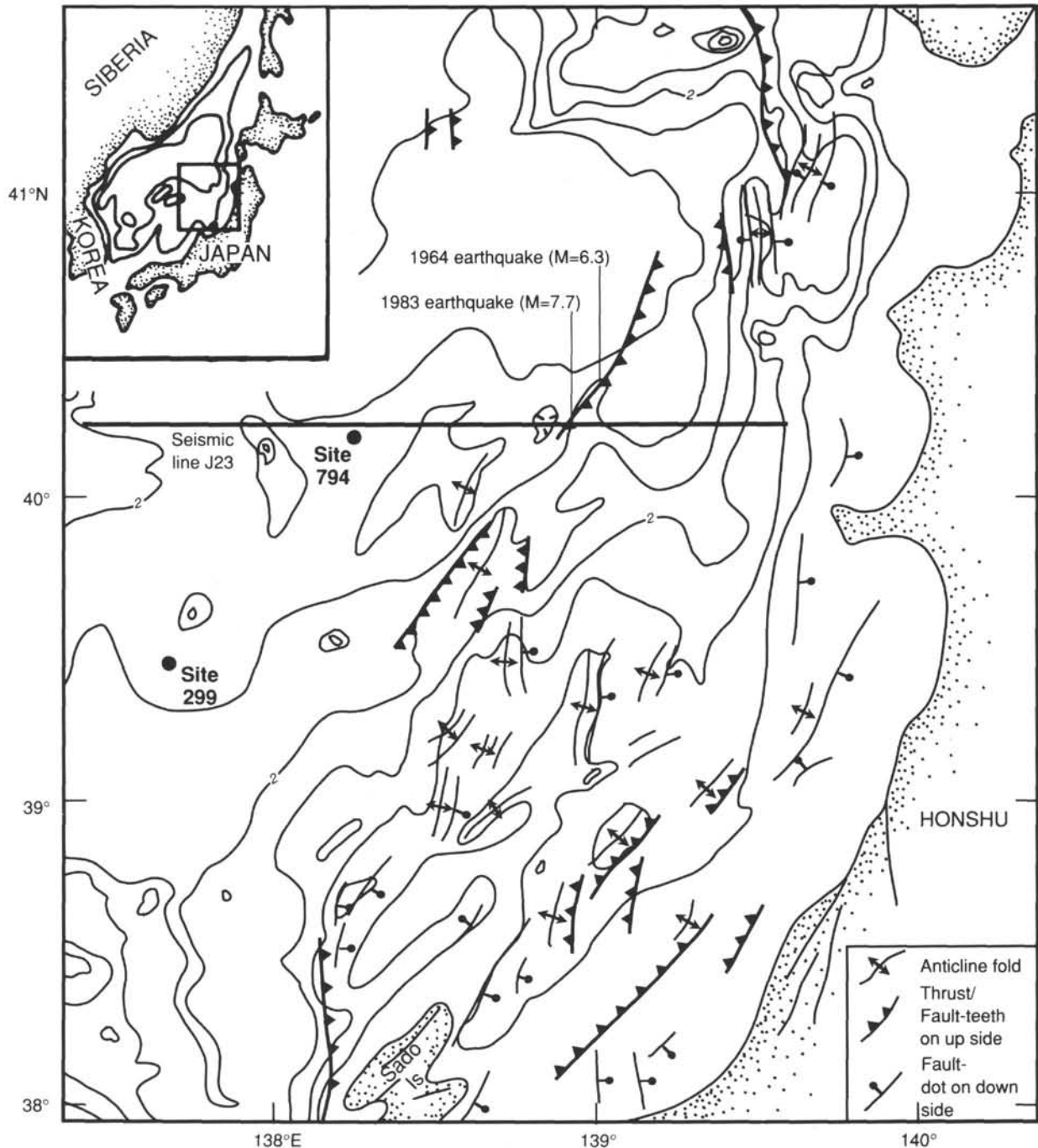


Figure 9. Map illustrating the location of Site 794 relative to recognized faults, fold axes, and recent shallow earthquake epicenters in the northern Yamato Basin region. Also shown is the location of seismic reflection profile J-23, illustrated in Figure 10. Figure from Tamaki, Pisciotto, Allan, et al. (in press).

seismic experiment in the pre-cased hole, and (2) to drill a fourth, dedicated hole for conducting a large-scale electrical resistivity experiment. During Leg 127 drilling, scientists recovered an excellent sedimentary sequence and successfully cored igneous basement at Site 794 (Fig. 8), but they experienced a stuck BHA in Hole 794C when pulling out of the hole, which prevented them from observing the hydrofracturing-crustal stress and required that they leave this hole in a position for fishing or for re-drilling during Leg 128. However, the basic objectives of drilling at Site 794 during Leg 128 remained intact, as summarized below.

Style and Dynamics of Back-Arc Rifting

The primary drilling objective at Site 794 for both Legs 127 and 128 was to determine the character and age of acoustic basement in a basinal location in the Japan Sea. Scientists drilling in both the Yamato and Japan basins during Leg 31 of the Deep Sea Drilling Project in 1973 had attempted this objective, but failed because of evidence of gas and a medical emergency (Karig, Ingle, et al., 1975). Although the intervening 16 yr saw repeated sampling of presumed basement rocks exposed on topographic highs in the Japan Sea, including the

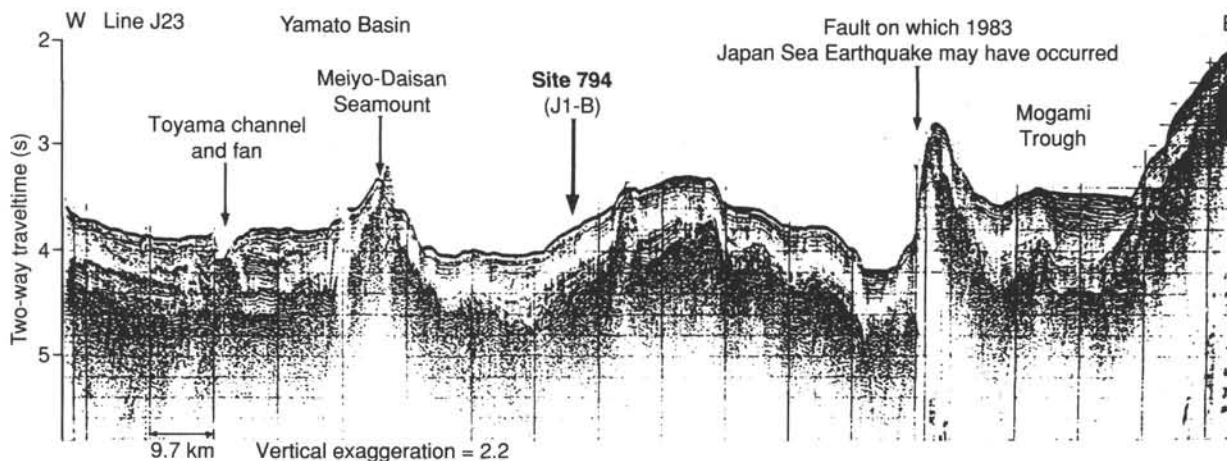


Figure 10. Seismic reflection profile J-23 of Honza (1979) across the northern Yamato Basin and northern extension of Sado Ridge, including the area of Site 794. This figure also illustrates the location of the important neotectonic belt through this area and the fault that may have been associated with the 1983 Japan Sea earthquake (M 7.7). See Figure 9 for the location of this profile.

Yamato Rise (Gnibidenko, 1979; Tamaki, 1988), acoustic basement beneath the major basins of the sea remained controversial and unsampled.

Site 794 is located at a critical juncture between the apparently thickened transitional crust of the Yamato Basin and the oceanic crust of the Japan Basin (Fig. 2). Leg 127 drilling demonstrated that the uppermost 100 m of igneous basement in the Site 794 area consists of stacked dolerite sills intruded into sediment of probable late early Miocene age. Leg 128 drilling was aimed at penetrating deeper into this sequence so as to sample and characterize these rocks further.

Geophysical Experiments

Two unique downhole geophysical experiments were planned for Site 794. Both of these experiments required the use of supporting ships from the University of Tokyo Ocean Research Institute that were scheduled to meet the *JOIDES Resolution* at Site 794. One experiment involved the installation of a broad-band digital seismometer in the igneous rock beneath this site. The second experiment consisted of oblique electrical resistivity measurements that required drilling a dedicated hole at Site 794.

Seismometers are designed to capture and record seismic waves as a means of scanning the Earth's interior and to obtain data about the dynamics of source events. The broader the frequency band and the wider the dynamic range of a given instrument, the more information that can be extracted from the record. A new three-component seismometer system, capable of recording longer period waves (with an 18-bit dynamic range) was developed specifically for the experiment at Site 794. The design of this instrument is such that it can record a wide range of seismic events—from high-frequency waves produced by local microearthquakes to surface waves emanating from major earthquakes of global proportions.

We planned for the downhole seismometer experiment to be performed in two phases or steps. The first phase involved a controlled-source seismic experiment that was aimed at analysis of the crustal structure in the vicinity of Site 794, with simultaneous observations using ocean-bottom seismometers in concert with the special downhole instrument. During this phase, we planned to record seismic data on board the *JOIDES Resolution*, while a second ship acted as a local source by towing and shooting air guns along a pre-planned track around Site 794. The second phase of this experiment involved initiation of long-term seismic observations with the

downhole instrument. This operation involved a supporting vessel and deployment of a seafloor recording and retrieval unit, along with a battery-power supply. This seafloor recording system is designed to be event-driven and was set to record only significant earthquakes because of its limited capacity to store 60-Mbyte data. Data obtained after successfully recovering the seafloor recorder will be used primarily to evaluate the laterally heterogeneous crust/upper mantle structure beneath the Japan Sea (Fig. 11).

The oblique electrical resistivity experiment that was planned for Site 794 was meant to improve our understanding of the structure beneath the Pacific Ocean floor off eastern Japan, across the Japanese Islands, and into the Japan Sea. In particular, variations in electrical resistivity are sensitive indicators of temperature changes in the Earth's crust and mantle and can point to the presence of partial melts or fluid at depth. Measuring natural electromagnetic disturbances allows one to determine resistivity to a depth of about 300 km in continental areas. However, the restriction imposed by a deep water column makes it impossible to obtain a detailed picture of resistivity in ocean areas without resorting to active experiments. Scientists think that very resistive structure exists to a depth of about 100 km beneath the Japan Sea—resistive even in comparison with the old Pacific crust just prior to its subduction in the Japan Trench (Fig. 12). Improved resolution at depth in the Japan Sea will be necessary to interpret the structure better within the zone of generally low resistivity in the young upper mantle beneath this area, which is characterized by indications of low velocity and low attenuation factor (Q). During the resistivity experiment, we planned to use a supporting vessel for injecting electrical current into the water column at various distances from Site 794. Before we began the experiment, a series of electrodes were placed in a dedicated hole drilled to 400 mbsf at Site 794 to measure real-time changes in the electrical field on board the *JOIDES Resolution* when the electrical source was activated on board the supporting ship.

OPERATIONS

The transit from Site 798 to Site 794 covered 248 nmi and took 24.5 hr, at an average speed of 10.1 kt. The *JOIDES Resolution* arrived on site at 1524UTC, 1 September 1989. The beacons deployed during Leg 127 were no longer working, so a new Datasonics beacon, model 354, 15.5 kHz, was launched at 1630UTC, 1 September, in a water depth of 2807 m.

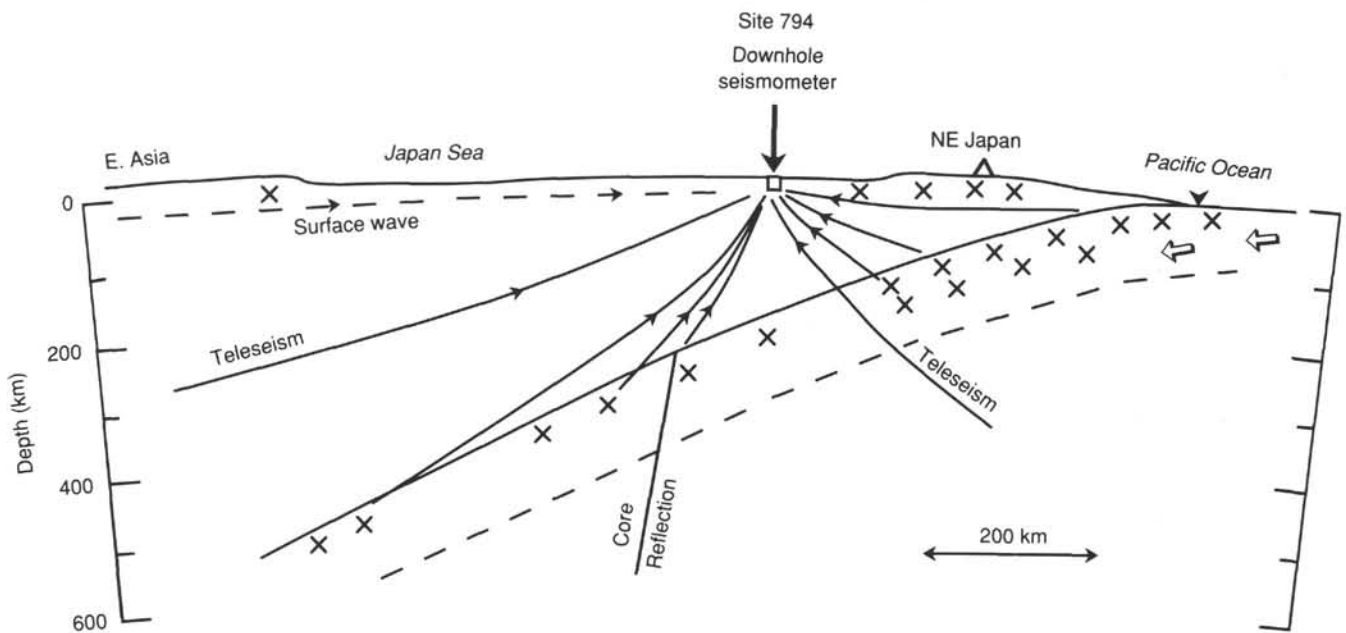


Figure 11. A schematic illustration of the significance of emplacement of a downhole seismometer at Site 794 in the northern Yamato Basin. Crosses represent earthquake foci. Seismic signals recorded by this instrument, including long period surface waves from regional and teleseismic events, will be utilized to analyze the upper mantle heterogeneity introduced by Pacific Plate subduction in this region.

Hole 794C

Hole 794C was drilled and cased during Leg 127; however, during that leg, the pipe became stuck in the hole, and the BHA was left in the bottom of the hole. Our purpose in returning to Hole 794C was to attempt to fish the BHA lost during Leg 127, to deepen the hole 80 m, and to install a downhole seismometer package in the borehole. To attempt the recovery, a fishing BHA was run with a video camera to search for the Hole 794C reentry funnel. An unsuccessful search grid was conducted for 6 hr on the basis of a preliminary global positioning system (GPS) fix. A subsequent GPS window showed that the initial position was 700 m off; thus, the ship was moved and another grid search was conducted. The reentry cone at Hole 794C was found in 1 hr, and was reentered at 0920UTC, 2 September, despite 40-kt winds, 6-ft heave, and strong fluctuating currents. The fishing BHA was run to 35 mbsf, where it hung up in the 11 $\frac{3}{4}$ -in. casing. The heave apparently set weight on the unsupported drill pipe, causing it to bend at the top of the cone and to break in an existing flaw. We did not observe the failure of the drill pipe, in part because of the effects of rough weather; so the crew continued to run drill pipe (along the seafloor) to the anticipated top of the fish (original BHA) at 455 mbsf. When we did not find the top of the fish, the drill pipe was run to a depth that corresponded to the bottom of the hole (688 mbsf) in the hope that perhaps during Leg 127 the original BHA may have unscrewed and fallen on the seafloor, instead of having been left in the hole.

We tried to determine if the original BHA had remained in the reentry cone (i.e., was not lying on the seafloor), but visibility was too poor and clay debris on the drill pipe posed a hazard to the video camera frame. We then pulled the drill pipe out of the hole for an inspection, which showed that the drill pipe had parted in an existing flaw in the bottom transition joint, leaving a 1.1-m stub at the top of the reentry cone. The strong changing currents, inaccurate compass readings, and a beacon at 200 m southeast of our location made further fishing difficult, and given the time constraints, we decided to drill a

new hole (Hole 794D) for the emplacement of the downhole seismometer and ended our operations at Hole 794C.

Hole 794D

The ship was moved 167 m southeast and Hole 794D was spudded at 1823UTC, 5 September 1989, at a water depth of 2806.9 m below sea level (bsl). The 16-in. casing was jetted in to 58 mbsf, with the top of the reentry cone 3 m above the mud line. Five joints of 16-in. casing, a 16-in. hanger, and a new-style reentry cone with an attached beacon were run.

This was the first time the new-style reentry cone had been tried; construction and deployment went smoothly, with only minor modifications required to set the reentry cone on the guide frame in the moon pool. The new reentry cone features an expanded mud pan and does not have a flow-line tube.

After jetting in the 16-in. casing, the hole was drilled to 573 mbsf. This short trip showed that the hole was in excellent shape and that it was filled with KCl mud. The 11 $\frac{3}{4}$ -in. casing was cemented to 560 mbsf. A 9 $\frac{7}{8}$ -in. RCB-BHA was run with a center bit, and a cement plug was drilled. The center bit was pulled, and an RCB with a double short-finger core catcher was lowered for hard-rock formations. RCB Cores 128-794D-1R through 128-794D-12R were taken from 573 to 666 mbsf, with 26.51 m of core recovered (Table 1). Poor recovery in fractured basalt in Cores 128-794D-4R to 128-794D-6R is attributed to frequent core breaks and the regrinding and jamming of cobbles in the throat of the core bit.

The igneous-rock formation was cored at a steady 2 m/hr, despite attempts to improve the rate of penetration. RCB coring was terminated at 2100UTC, 11 September, because of time constraints imposed by the scheduled arrival of the two support vessels (*Tansei-maru* and *Kaiko-maru-5*) needed for our geophysical experiments, which temporarily suspended operations at Hole 794D until the installation of the downhole seismic experiment began on 25 September. The *JOIDES Resolution* departed Site 794 to begin operations at Site 799, but returned to Site 794 at 0448UTC on 22 September. Our beacon was still working. A 9 $\frac{7}{8}$ -in. RCB bit and BHA were run and reentry was accomplished in 14 min at 1133UTC, 22

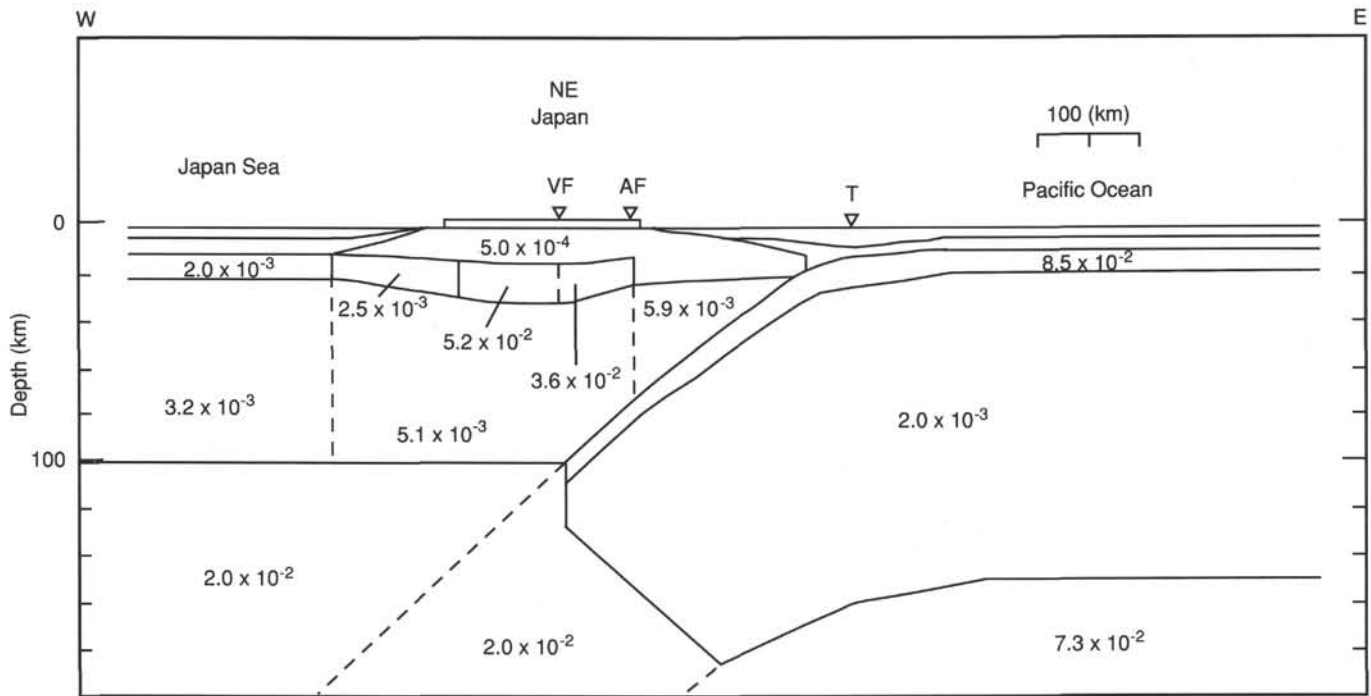


Figure 12. Schematic, two-dimensional, conductivity model across the northeastern Japan arc, including old Pacific crust just prior to subduction, and the presumably much younger upper mantle and crust in the Japan Sea back-arc region. Conductivity of each block in this east-west cross section is given in s/m. Figure from Utada et al. (1986). VF = volcanic front, AF = aseismic front, and T = trench axis.

September. RCB Cores 128-794-13R to 128-794-20R were taken from 666.0 to 733.5 mbsf (Table 1). Recovery was poor as a result of highly fractured and altered basalt cobbles that jammed in the core catcher. Coring was terminated at 2300UTC, 23 September, because of time constraints.

A logging BHA was run to 75.5 mbsf. The seismic stratigraphy combination tool could not get through a bridge at 607 mbsf, and the tool was pulled out while logging up the hole. Hole 794D hole was cleaned out and displaced with a 2% KCl logging mud. The seismic stratigraphy tool was re-run successfully to total depth. The FMS encountered a bridge at 595.6 mbsf, but logging continued up the hole. Bridges at 594 and 640 mbsf were washed, and a second attempt to run the FMS was stopped by an obstruction at 642 mbsf. Attempts to clear the hole and work the tool down were unsuccessful, and logging was terminated to remain on schedule for our geophysical experiments (See "Downhole Seismometer Experiment" section, this chapter).

The borehole seismometer was re-headed, function-tested, and then run in the hole at 0215UTC, 26 September, to a setting depth of 714.5 mbsf. The Schlumberger logging cable was cut, and a Bowen rope socket was installed. After checking the seismometer, a torpedo connector was used to rejoin the Schlumberger logging cable. The ship was offset 1680 m south of Hole 794D at 33.3 m/min, while an additional 1480 m of cable was deployed by the logging unit. A new Datasonics beacon was dropped 1480 m south of Hole 794D to assist with keeping our position during the seismic survey.

The *Tansei-maru* arrived at Hole 794D at 1430UTC, 24 September, deployed one digital and seven analog OBSs and took dredge samples. We then conducted the borehole seismometer real-time experiment in Hole 794D for 56.75 hr, while the *Tansei-maru* shot air guns in a survey pattern around the hole. The seismometer experiment was successful (See "Downhole Seismometer Experiment" section, this

chapter). An additional 49 m of logging cable was deployed, this cable was cut, two guide joints were stripped over the cable, and the cables were re-headed. The cut-off end of the cable was keel-hauled under the ship from the moon pool to the starboard side using a pre-installed transfer line. A second support vessel, the *Kaiko-maru-5*, arrived at the site at 1000UTC, 29 September. After several tries in rough seas, we passed the logging cable from the *JOIDES Resolution* to the *Kaiko-maru-5*. The seafloor instrument package was deployed by the *Kaiko-maru-5* on 30 September. The *Tansei-maru* retrieved the OBSs and left for Japan.

Hole 794E

The *JOIDES Resolution* moved another 50 m south, where Hole 794E was spudded at 1915UTC, 30 September. An 11 $\frac{1}{16}$ -in. hole was drilled to 400 mbsf. Hole 794E hole was swept twice during drilling, and the bit was pulled up to 74.7 mbsf. The electrical resistivity long-spaced tool (see "Electrical Resistivity Experiment" section, this chapter) consists of five potential electrodes that have been installed on 310 m of cable. The *Kaiko maru-5* supplied a 100-V, 20-amp current with a seafloor electrode in a pattern around Hole 794E. Electrical resistivity measurements were conducted from 0815UTC on 30 September to 0800UTC on 1 October. The resistivity tool detected a high background potential, possibly due to electrical noise created by the proximity of the drill pipe, so the bit was pulled to 65.7 mbsf at 1400UTC on 30 September and to 57 mbsf 2 hr later. This seemed to reduce noise levels, and the experiment was completed successfully (see "Electrical Resistivity Experiment" section, this chapter). Both the resistivity cable and the drill pipe were pulled out of the hole, which ended operations at Hole 794E. At this time, the *JOIDES Resolution* departed for Site 799 so that we could finish our drilling program in Hole 799B.

Table 1. Coring summary, Site 794.

Core number	Date (Sept 1989)	Time (UTC)	Depth (mbsf)	Length cored (m)	Length recovered (m)	Recovery (%)	Age
1R	10	1010	573.0–580.6	7.6	1.75	23.0	
2R	10	1335	580.6–585.9	5.3	2.83	53.4	
3R	10	1755	585.9–595.4	9.5	3.45	36.3	
4R	10	2255	595.4–604.6	9.2	0.71	7.7	
5R	11	0500	604.6–614.0	9.4	0.31	3.3	
6R	11	1125	614.0–619.0	5.0	0.00	0.0	
7R	11	1900	619.0–623.5	4.5	2.12	47.1	
8R	12	0145	623.5–633.0	9.5	2.88	30.3	
9R	12	0640	633.0–642.2	9.2	2.12	23.0	
10R	12	1240	642.2–651.4	9.2	2.52	27.4	early or middle Miocene
11R	12	1850	651.4–660.7	9.3	3.61	38.8	
12R	13	0430	660.7–666.0	5.3	4.21	79.4	
13R	22	1950	666.0–670.5	4.5	2.41	53.5	
14R	23	0000	670.5–679.9	9.4	2.35	25.0	
15R	23	0340	679.9–689.3	9.4	0.56	6.0	
16R	23	0810	689.3–698.6	9.3	1.18	12.7	
17R	23	1150	698.6–707.9	9.3	0.74	8.0	
18R	23	1550	707.9–717.1	9.2	0.43	4.7	
19R	23	2050	717.1–726.6	9.5	0.16	1.7	
20R	24	0640	726.6–733.5	6.9	0.51	7.4	
Coring totals				160.5	34.85	21.7	

IGNEOUS ROCKS

Introduction

Hole 794D represents the deepest penetration yet into the igneous complex that floors the Yamato Basin. On the basis of chemical evidence, drilling at this hole penetrated into the igneous complex that represents the early Miocene(?) volcanic floor of the northern Yamato Basin. Rocks recovered from the lower portion of Hole 794D are interpreted to represent igneous "basement" beneath this site. A total of 34.85 m of core was retrieved from Hole 794D between 573.0 and 733.5 mbsf, representing a recovery of 21.7%. All but 1.60 m of the core is igneous. The data base derived from shipboard analysis includes 19 thin sections and 16 shipboard, whole-rock, XRF analyses for major and minor elements. Individual units were identified on the basis of diagnostic mineralogy and texture, supplemented by the XRF analyses and preliminary paleomagnetic data. Care was taken to recognize normally expected increases in grain size with increasing distance from a contact. With one exception, lithologic contacts were not recovered in the cores. The orientation of fractures was recorded as an azimuth relative to the top of a section being 0°. Interpretation of the lithology was complicated by the gaps in recovery and the moderate to high alteration of most of the rocks.

More details about the sequence were obtained from downhole logging data (See "Downhole Measurements" section, this chapter). Using the NGT, we detected clay-rich zones of sediment or altered lava enriched in potassium, uranium, and/or thorium. The upper chilled margins of the lava exhibited drastic enrichments of potassium and uranium. The resistivity log recorded the resistive massive sills and flows. The flows are less resistive and include conductive sediments and/or altered zones. The velocity, resistivity, and FMS logs detected heterogeneous layers and fracture zones. By combining all of this information, lithologic boundaries were located with greater precision than could be done from the core alone.

A summary of the units encountered in Hole 794D and the igneous units in Holes 794B and 794C drilled during Leg 127 is given in Figure 13. Where the boundary for a unit is ambiguous, it was taken from the logging information instead of from

the measured core length because the locations of voids in the core are not known, and by convention the recovered material is pushed to the top end of the core liner.

Lithology

Nine lithologic units were recognized in Hole 794D. One is a clayey silt with an occurrence of small tephra (Unit 5). The remaining eight units are igneous. They consist of:

1. Four dolerite sills (Units 1, 3, 4, and 9) that had been intruded into soft sediments at a shallow depth and
2. Four doleritic basalts (Units 2, 6, 7, and 8) that had been erupted onto the seafloor or intruded into soft sediment near the seafloor. Interpretation of these units as invasive sheet flows is based on their texture, the presence of prominent chilled margins, and in one case (Unit 6), the lack of significant thermal effects on sediments at the upper contact. However, many textural features are intermediate between flows and sills. The magmatic units are obviously more or less contemporaneous and were formed in the upper part of a thick sedimentary sequence or upon the substratum. The distinction of flows and sills is important for determining the sequence of the magmatic events, although an incorrect identification of the type of unit would not alter the determined sequence.

Units 3 and 4 are separated by a large void in the core and are distinguished by their petrographic features and by the presence of a bed of volcanic sand. This sand was not recovered by rotary drilling. It formed a bridge in the hole and was accidentally sampled with the temperature logging tool.

Unit 6 is magnetized in normal polarity, whereas Unit 7 underneath and Unit 5 above have reverse polarity. This feature is used to distinguish Unit 7 as a separate unit, not just the inner and lower part of flow Unit 6.

Petrography

Visual core descriptions and petrographic analyses are given in Section 3 of this volume. The following is a summary description of the petrographic features recognized during shipboard analysis. The interval over which a unit was defined represents the portion of the unit recovered.

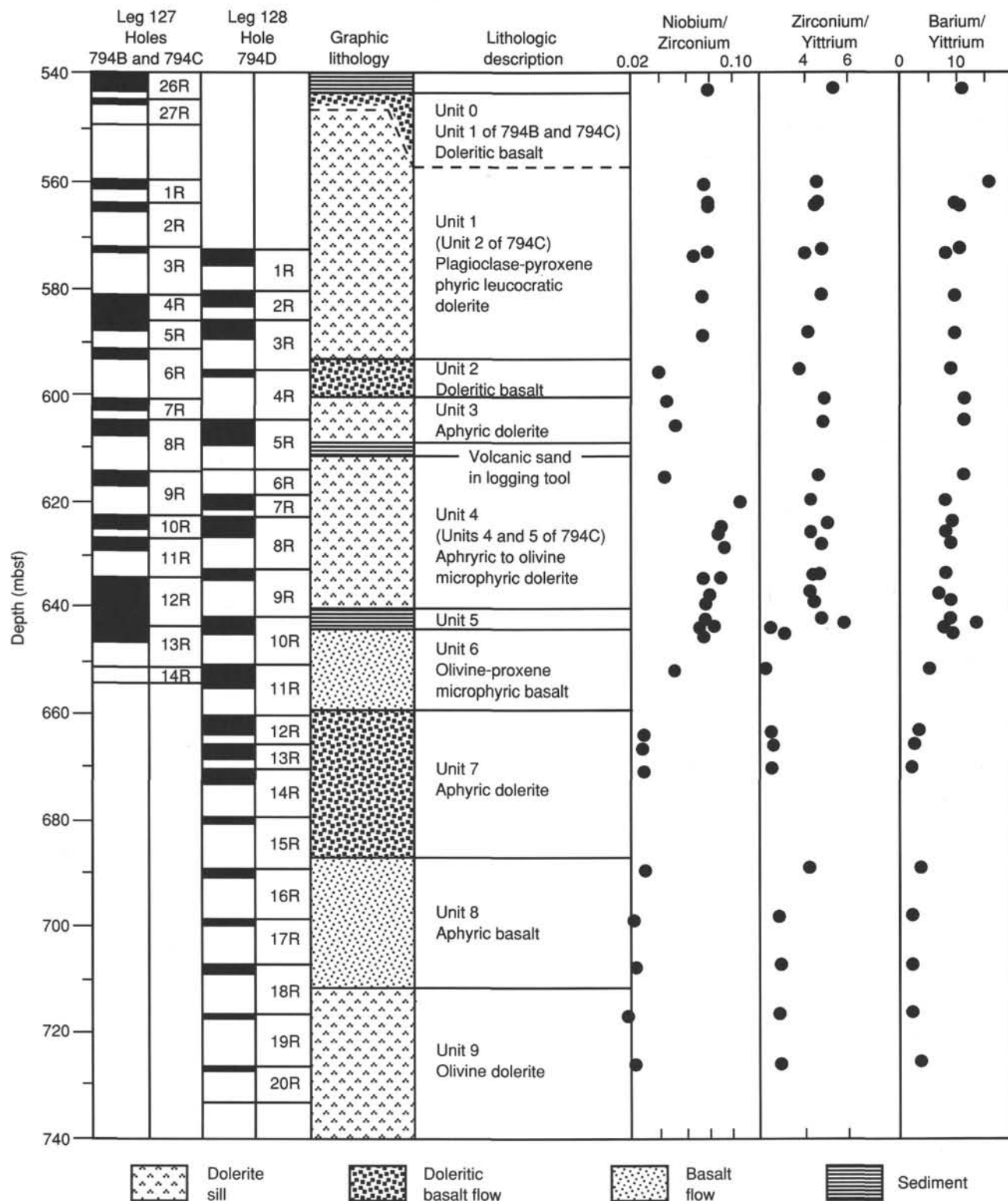


Figure 13. Core summary of igneous rock at Site 794: recovery, lithologies, unit boundaries, and geochemical variations. The unit boundaries are from logging information. Data for Holes 794B and 794C of Leg 127 are from Tamaki, Prosciutto, Allan, et al. (in press). Basement is taken to be the top of Unit 6, where there is an abrupt change in minor element chemistry.

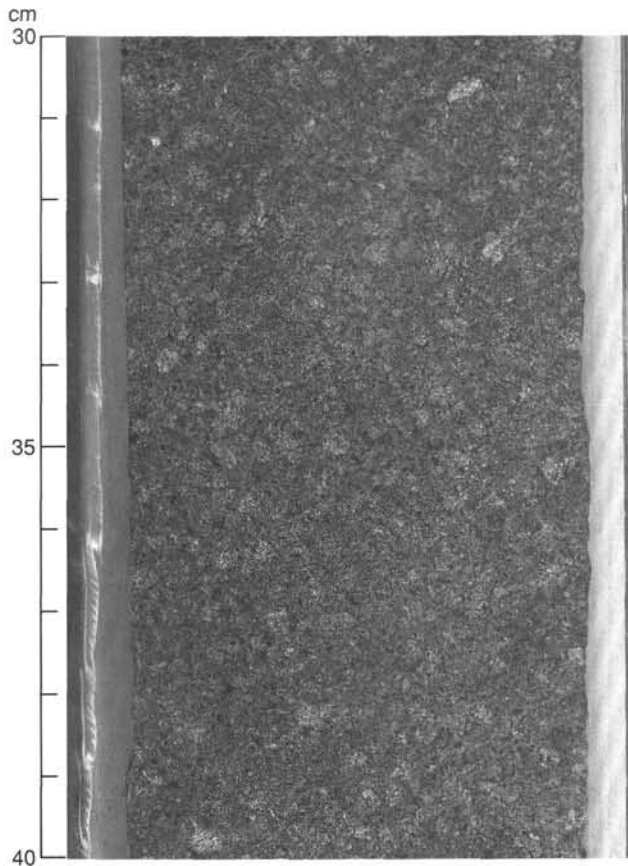


Figure 14. Plagioclase-phyric, leucocratic dolerite of Unit 1 (Section 128-794D-2R-1, 30–40 cm).

Unit 1

Unit 1, plagioclase-pyroxene, phyric, leucocratic dolerite, is defined from Section 128-794D-1R-1, 0 cm to Section 128-794D-3R-3, 150 cm (573.0–589.4 mbsf). Neither the top nor bottom contacts were observed. This dark greenish gray dolerite is massive, dense and nonvesicular, and is characterized by abundant (25%–40%), uniformly distributed, phenocrysts of plagioclase (Fig. 14). The plagioclase occurs as 1- to 5-mm, euhedral to subhedral, tabular to subrounded crystals having a seriated texture and is locally glomerophytic. Phenocrysts of orthopyroxene (1–4 mm, 1%–4%), clinopyroxene (1–2 mm, 2%–8%, euhedral to subhedral), rare pseudomorphs after olivine (3%), and skeletal, euhedral magnetite (5%) are also present. Pyroxene phenocrysts are less abundant in the upper part. An intergranular and intersertal groundmass contains laths of plagioclase, subhedral to anhedral clinopyroxene and euhedral to subhedral magnetite, together with interstitial brown glass, featherlike textures involving plagioclase, trace pyrite, and 1-mm symplectites of plagioclase and pyroxene.

Alteration is moderate (15%–20%), with glass in the mesostasis converted to variolitic sideromelane and smectite and all of the olivine replaced by iron oxide and smectite. A few fine fractures from 0.1 to 1 mm wide are sporadically distributed; these are most abundant in Core 128-794D-3R. Fracture azimuths were measured at 10° to 20°, 290° to 300°, and 340° to 350°. The fractures are filled with chlorite and/or smectite and rare traces of hematite and pyrite.

Unit 2

Unit 2, doleritic basalt, is defined in Section 128-794D-4R-1 from 0 to 85 cm (595.4 to 596.1 mbsf). No contacts are present, although Piece 1 is a slickensided fragment containing quartz

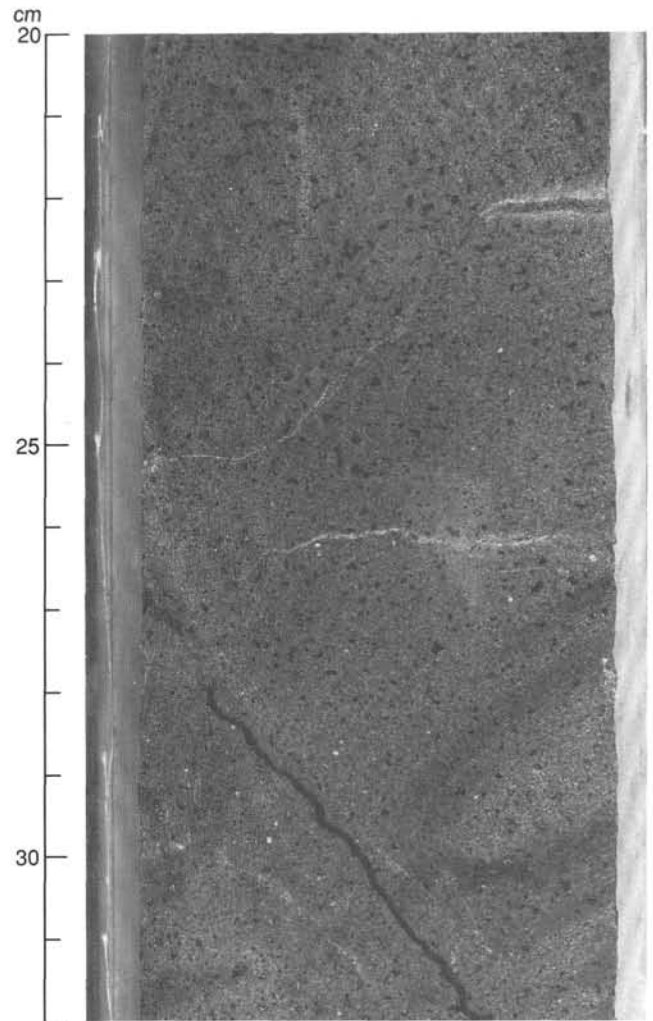


Figure 15. Doleritic basalt of Unit 2 (Section 128-794D-4R-1, 20–32 cm).

and chlorite-smectite (XRD determination), which may indicate a fracture zone. The unit is dark green, massive, dense, and somewhat vesicular (Fig. 15). Irregularly shaped vesicles, from 0.5 to a few millimeters in diameter and filled with green “smectite,” occupy 3 to 5 vol% of Pieces 5A, 5B, and 8. Unit 2 is characterized by 10% of 0.5- to 1-mm, euhedral, totally altered microphenocrysts of (former) olivine, perhaps with some (former) pyroxene. The groundmass contains 30% of 0.2- to 0.6-mm plagioclase laths and 30% of 0.1- to 0.3-mm subhedral pyroxene in an intersertal texture. Featherlike textures are also present.

The rock has been highly altered (65%), with the olivine microphenocrysts and pyroxene microcrysts totally converted to iron oxide and smectite, and the vitric mesostasis converted to sideromelane. A 1-mm vein of chlorite and smectite having an azimuth of 320° was found in Piece 3C.

Unit 3

Unit 3, aphyric dolerite, is defined in a short piece (45 cm) of core recovered in Section 128-794D-5R-1 cm (604.6–604.9 mbsf). There are no contacts in the core. The rock is dark green, massive, dense, and nonvesicular. The groundmass contains 40% of medium-grained (0.5–1 mm) plagioclase laths, 10% of euhedral, pseudomorphosed olivine, and 30% of partly altered, subhedral pyroxene in an intergranular texture, together with 5% of 0.02- to 0.2-mm skeletal magnetite.

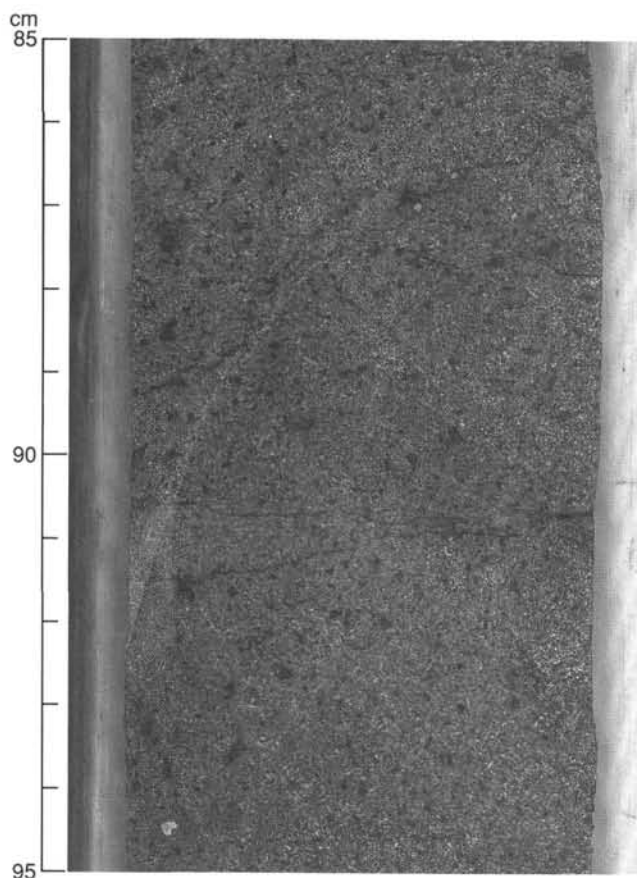


Figure 16. Vesicular microphyric basalt of Unit 4 (Section 128-794D-9R-1, 85–95 cm).

Alteration is moderate to high (45%), with the original olivine or pyroxene totally altered to iron hydroxides and smectite. A large, slickensided, subvertical fracture with normal fault displacement occurs in Pieces 1, 2, and 3.

Unit 4

Unit 4, aphyric to olivine microphyric dolerite, is defined in core from Sections 128-794D-7R-1 at 0 cm, to 128-794D-10R-1 at 5 cm (619.0–642.7 mbsf). The top contact was not recovered. The bottom contact occurs in rubble at the top of Section 128-794D-10R-1 near 5 cm. The grain size of the groundmass decreases toward the bottom of Section 128-794D-9R-2, heralding the approach of the bottom contact. The rock is medium gray to greenish gray with pale green mottling, massive and dense, and has an intergranular to interstitial texture (Fig. 16). Vesicles from 0.2- to 2-mm with rounded, elliptical, and irregular shapes are filled with pale green “smectite.” These vesicles are distributed erratically and are rare to uncommon in abundance. Unit 4 is characterized by 1- to 1.5-mm, pseudomorphosed olivine phenocrysts that constitute about 20% of the rock. The groundmass consists of 30% plagioclase, 30% clinopyroxene, and 5% magnetite together with some interstitial brown glass converted to greenish-brown clays and sideromelane. The plagioclase is ordinarily made up of euhedral to subhedral crystals, 0.5 to 1 mm in size, but in places becomes microphenocrystic at up to 1.5 mm in size. Likewise, subhedral pyroxene is ordinarily 0.3 to 0.6 mm, but also forms rare microphenocrysts up to 1 mm in size. Magnetite is contained in 0.03- to 0.1-mm, euhedral to subhedral crystals with dendritic and skeletal habit.

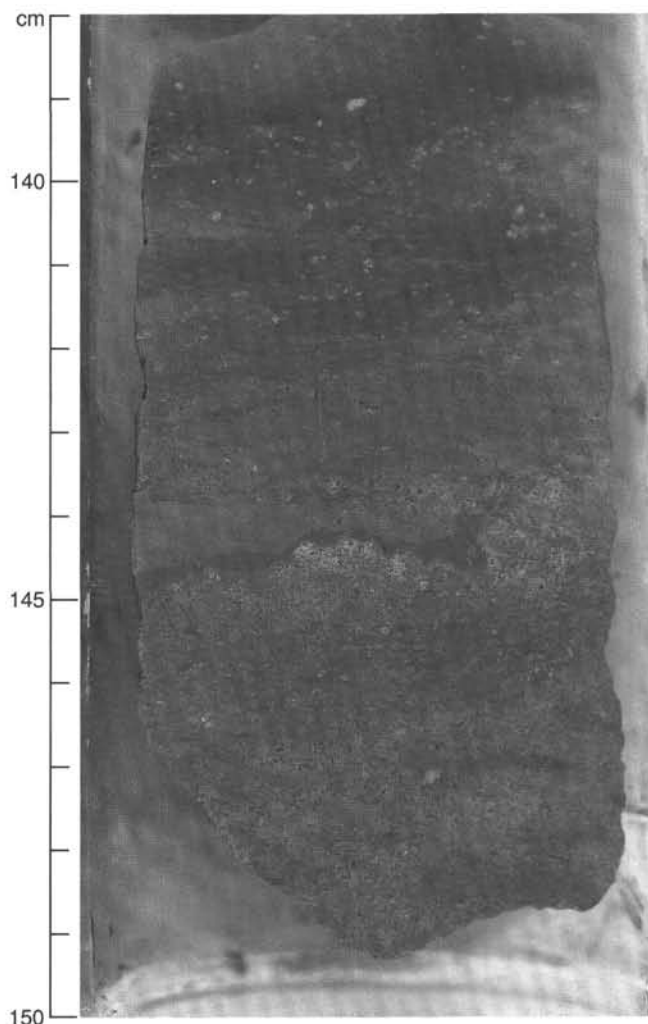


Figure 17. Silty clay of Unit 5 with bioturbated ash layer from 144 to 149 cm (Section 128-794D-10R-1, 138–150 cm).

Alteration is high (50%–60%). Fine fractures, 0.1 to 0.3 mm wide and filled with dark green minerals and minor iron oxides, are fairly common. These fractures are subvertical in the core with azimuths that range from 355° to 10°.

Unit 5

Unit 5, tuffaceous clayey siltstone with foraminifers, is defined in Section 128-794D-10R-1 from 5 to 150 cm, and in the upper 15 cm of Section 128-794D-10R-2 (642.7–643.9 mbsf). The unit is characterized by dark gray to dark brown tuffaceous, clayey siltstone. Sediments in Unit 5 are crudely bedded, a result of the ubiquitous presence of bioturbation. Burrows are exclusively horizontal, unlined, deposit-feeding traces, which have been flattened by compaction. Abundance of foraminifers varies between <1% and 3% of total sediment volume; they are extensively dissolved, which inhibits taxonomic assignment (See “Biostratigraphy” section, this chapter). The basal and upper contacts are associated with slickensides and crenulated slaty cleavage.

Bioturbated, vitric debris consisting of 0.3- to 1-mm hydroclastic shards that have been deposited as a crude layer or dispersed in silty clay, occurs as a minor lithology from 145 to 150 cm in Section 128-794D-10R-1 (Fig. 17). Crystals are absent. The margins of the shards have been altered to greenish brown palagonite, and the cores to blue chalcedony, smectite, and minor zeolite(?). These alteration features, as

well as the typical morphology of blocky shards having fracture-bounded surfaces that transect a few vesicles, attest to the underwater volcanic origin of the tephra.

In four smear slides, scarce nanofossils and minor centric diatom fragments are present, further attesting to the marine origin of the sediments in Unit 5. Volcanic glass is abundant; fish fragments and feldspar euhedra are minor components.

Baked and thermally altered sediments are conspicuously absent at the base and top of Unit 5; therefore, evidence for an intrusive origin of the surrounding igneous rocks is absent. However, the contact zones of Unit 5 do record substantial shearing and brittle deformation.

Well-developed slickensides are present in the upper 30 cm of Section 128-794D-10R-1. At 22 cm, a prominent set of slickensides is bedding-parallel, whereas at 12 to 17 cm, the slickensides are oriented at a high angle to the bedding. These nearly orthogonal structural fabrics may be attributed to polyphase deformation or to partitioning of complex stress into discrete domains of deformation and slickenside formation.

The basal contact of Unit 5 also records structural disturbance. Here, the silty claystone sediments possess a millimeter-scale, bedding-parallel cleavage. From 1 to 8 cm, scaly to slaty partings have well-developed slickensides, which have been deeply crenulated to form wavy partings. This may suggest a polyphase deformation.

Unit 6

Unit 6, olivine-pyroxene microphyric basalt, is defined from Section 128-794D-10R-2 at 15 cm, to Section 128-794D-11R-3 at 122 cm (643.9–655.0 mbsf). The top contact or near-top contact occurs in rubble in Section 128-794D-10R-2 at 15 cm (Piece 1A). Sediment above the contact exhibits no evidence of having been abnormally heated; thus, Unit 6 must be a lava flow. The bottom contact was not observed. The rock is medium gray, massive, dense, and vesicular. In the top part of the unit (Section 128-794D-10R-2, Pieces 1A-6A), vesicles are (1) ovoid to irregular, (2) 0.3 to 1.3 mm in size, (3) occupy about 1% to 3% of the core volume in patchy distribution and in trails, and (4) are partly unfilled. At greater depths, vesicles become rare. They are 1 to 2 mm in diameter and are filled with green smectite and calcite(?). A few scattered large vesicles up to 5 × 8 mm are filled with green smectite and calcite. One of these vesicles contains bladed iron sulfide, probably marcasite.

The upper, finest-grained part of the unit is a totally altered microlitic basalt having 0.2- to 0.6-mm plagioclase in sheaf and poorly distinguishable quench textures. The deeper, coarser part is microphyric. It originally contained 25% of 0.4- to 1.4-mm euhedral olivine and 10% of 0.3- to 1.3-mm euhedral pyroxene, both now totally converted to iron oxide and smectite. The groundmass is intersertal, with 20% to 25% of sheaflike plagioclase microlites, 10% to 25% of 0.1- to 0.4-mm subhedra of partly altered clinopyroxene, and 8% of 0.01- to 0.1-mm euhedral to subhedral magnetite. Interstitial glass is microcrystic with a featherlike texture of plagioclase and has been altered to palagonite and smectite.

Alteration, described previously and including traces of pyrite, is high (50%–62%). There are a few subvertical fractures up to 1 mm wide having azimuths that range from 340° to 0° and that are filled with white calcite (XRD identification), dark green chlorite(?), and pale green smectite. We observed one 0.5-mm fracture having an azimuth of 90° and filled with calcite. Magnetite within about 5 cm of a fracture in Section 128-794D-11R-2, Piece 1A, has been oxidized to hematite.

Unit 7

Unit 7, aphyric dolerite, is defined from Section 128-794D-12R-1 at 0 cm to Section 128-794D-15R-1 at 85 cm (660.7–

680.5 mbsf). No contacts were found. The rock is dark grayish green and massive (Fig. 18). In the middle part of the unit, the texture is subophitic. The groundmass consists of 6% euhedral and skeletal magnetite, 0.03 to 0.3 mm in size; 15% euhedral and partly serpentinized olivine, 0.3 to 0.8 mm in size; 32% plagioclase, 0.5- to 2-mm laths; 35% subhedral clinopyroxene in 0.3- to 2-mm tablets; and 10% interstitial secondary alteration products of microcrystalline phases and glassy mesostasis. Frequent variations of the grain size may be observed, either progressive or sharp, as in some 20- to 30-cm-wide, finer-grained beds that are both horizontal (Section 128-794D-13R-1; Fig. 19A) and steeply dipping (Section 128-794D-14R-1; Fig. 19B). These variations are attributed to flow differentiation. In the uppermost and lowermost parts of Unit 7, the grain size of plagioclase and pyroxene decreases and the abundances of interstitial phases increase.

Alteration is moderate (12%–20%) to high (>50%) in some fracture zones and in the lower part of the unit. Large veins having azimuths of from 295° to 80° and up to 2.5 cm wide are abundant. These veins have a talc-chlorite border and a fibrous calcite core (XRD determinations).

Unit 8

Unit 8, aphyric basalt, is defined from Section 128-794D-16R-1 at 0 cm to Section 128-794D-18R-1 at 43 cm (689.3–708.3 mbsf). No contacts were found, but the uppermost rubble exhibits evidence of severe quenching. Its groundmass has been invaded by minute radiating intergrowths of plagioclase and pyroxene, which indicates the proximity of the upper contact.

In the top part of the unit, vesicles are ovoid, 0.1 to 1 mm in size, and occupy about 3% of the volume. These vesicles are filled with calcite and have chlorite rims. The upper quenched part has been highly altered (60%–70%). Only microcrysts of magnetite, altered olivine, and plagioclase can be recognized. The deeper, coarser part of Unit 8 is less altered. This part is subophitic with 8% of 0.03- to 0.3-mm, euhedral and skeletal magnetite; 15% of 0.3- to 0.8-mm, euhedral, partly serpentinized olivine; 32% of 0.5- to 2-mm, plagioclase laths; 35% of 0.3- to 2-mm, subhedral clinopyroxene; and 10% of interstitial secondary minerals. As a general rule, crystallinity increases in the inner part, and alteration decreases to less than 20%.

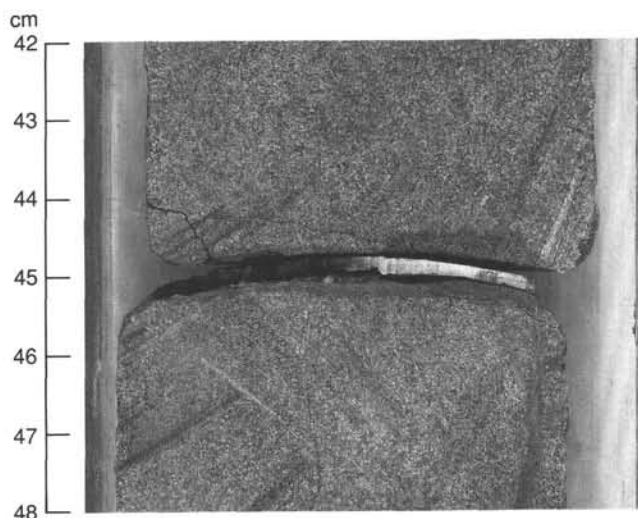


Figure 18. Aphyric dolerite of Unit 7 with flat-lying vein at 45 cm. Note the fibrous texture of calcite (Section 128-794D-12R-3, 42–48 cm).

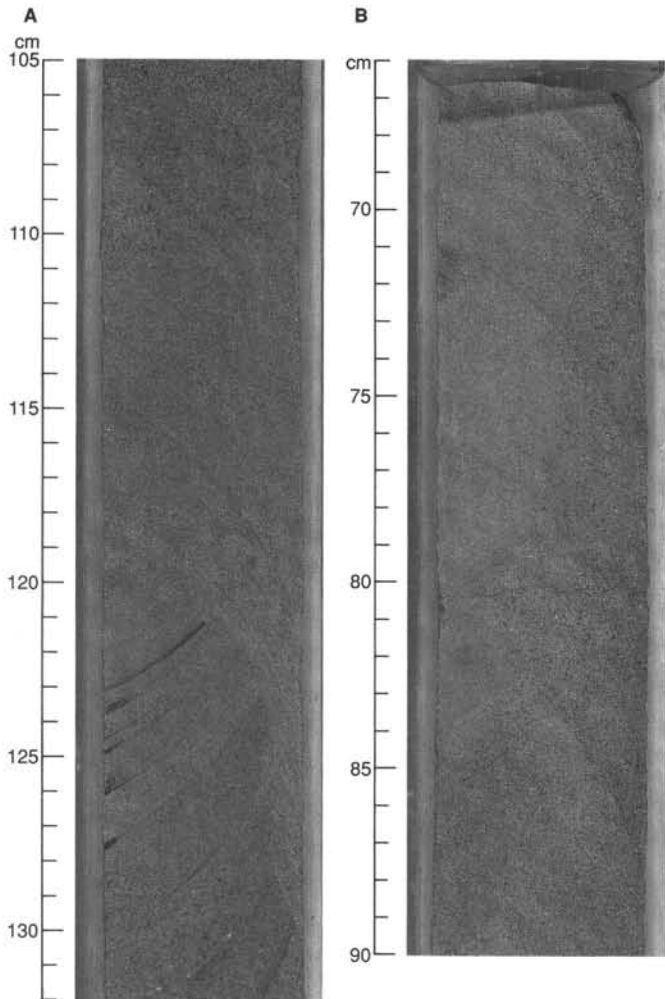


Figure 19. Variation in grain sizes in Unit 7 caused by flow differentiation. **A.** Subhorizontal (Section 128-794D-13R-1, 105–132 cm). **B.** Subvertical (Section 128-794D-14R-1, 66–90 cm).

There are numerous fractures and veins, 1- to 4-mm-wide and filled with talc and chlorite. Two main directions prevail: 60° to 80° and 350° to 10° . The subvertical fractures are commonly slickensided.

Unit 9

Unit 9, olivine dolerite, is defined in core from Section 128-794D-19R-1, 0 cm to the bottom of the hole (Section 128-794D-20R-1, 51 cm; 717.1–727.1 mbsf). No contacts were observed. The rock is dark greenish gray, with a fine-to-medium grain size. The structure is massive without vesicles. The texture is subophitic with 8% of 0.03- to 0.3-mm, euhedral magnetite; 25% of 0.3- to 0.8-mm, partly serpentinized euhedral olivine; 27% of 0.5- to 2-mm, plagioclase laths; and 30% of 0.4- to 2-mm, subhedral pyroxene—some as bladed crystals. Interstitial microcrystalline phases have been altered into smectites and iron-oxides. Rubble at the end of the interval has a fine grain size.

Rare fractures, 1 to 2 mm wide, are bordered by talc and chlorite and are filled with calcite in the center. One fracture contains some clusters of flat, aggregated, pyrite crystals.

Structural Features

Several sets of fractures and veins were observed in Hole 794D cores. They differ in their geometric attitude, in the importance of their alteration halo, and in the presence or absence and nature of filling material.

The attitude allows at least two basic types of fractures to be distinguished: gently dipping and steeply dipping. In both groups, there are likely to be some conjugate systems.

In the igneous rocks, gently dipping fractures (25° – 40° , mostly near 30°) in some places are arranged in sets, showing a symmetry with respect to the horizontal; these are assumed to be conjugate. This occurs, for instance, in Section 128-794D-12R-3 from 84 to 115 cm (663.7 mbsf; Fig. 20B); other examples are found in Sections 128-794D-12R-3 (664.3 mbsf) and 128-794D-13R-1 (666.6 mbsf). These fractures almost systematically exhibit a well-developed alteration halo. They are filled with green (chlorite-talc) material on the margins and, except in a few cases, with white calcite in the center. Their geometry suggests that they were initiated as conjugate shear joints (or faults) during a compressive phase (maximum stress component subhorizontal, minimum stress component vertical). Some flat-lying (i.e., subhorizontal) fractures might be related to that event, as synchronous tension cracks (Fig. 18), but this is not clearly demonstrated. Unfortunately, the pieces containing convincing conjugate sets of these gently dipping fractures are not oriented. However, with reference to the attitude of the low-angle veins in the oriented parts, Sections 128-794D-12R-2, 118 to 128 cm (Fig. 20C) and 128-794D-14R-2, 64 to 80 cm (Fig. 20D), a north-northeast to south-southwest direction of compression is possible. A few gently dipping fractures are almost devoid of an alteration halo and remain closed (fissures, joints), showing no filling. These fractures are probably younger than the aforementioned fractures, but no orientations are available.

The steeply dipping fractures show various attitudes and behavior with respect to their vein-filling history. Some clearly normal faults, with steep-pitched slickensides, appear to be young features because they crosscut the veins. Such fault surfaces, inclined at about 60° , are present, for instance, in Section 128-794D-5R-1 at 604.2 mbsf, and in Section 128-794D-16R-1 at 689.7 mbsf (Fig. 21); they are not oriented. Some steeply dipping (55° – 70°) joints or veinlets are probably

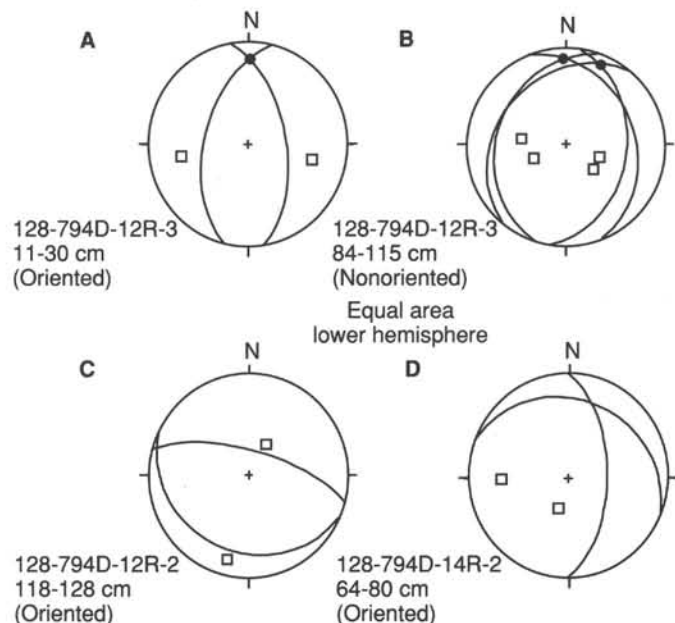


Figure 20. Equal-area stereonet plots of some fractures, great circles, and poles (squares). Dots mark the intersection of assumed conjugate sets. **A**, **C**, and **D** correspond to pieces (intervals) oriented by means of paleomagnetic measurements. **B** corresponds to a nonoriented piece.

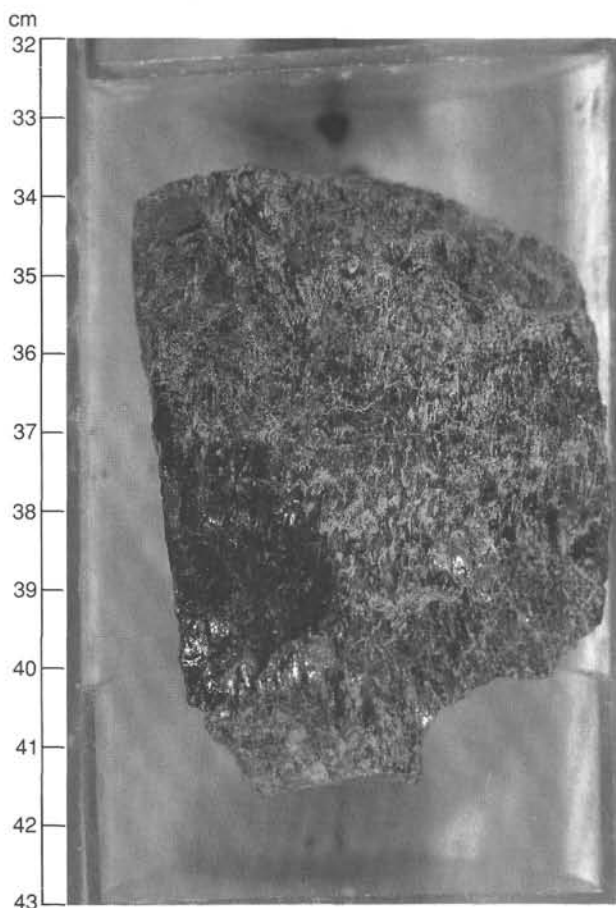


Figure 21. Fault surface with slickensides in Section 128-794D-16R-1 from 32 to 43 cm. True dip of 60° , normal fault slip.

arranged in conjugate sets, as in Section 128-794D-12R-3 (66.9 mbsf; Figs. 20A and 22). In this example, the veinlets are either closed, with a narrow alteration halo, or are filled with a thin film of calcite. Their orientation suggests that an east-west extension phase was responsible for their initiation (Fig. 20A); this is compatible with the attitude of a similar joint in Section 128-794D-14R-2 at 672.7 mbsf (Fig. 20D). Similarly dipping (50° – 70°) fractures are now transformed into veins, as in Sections 128-794D-12R-1 (662.4 mbsf), 128-794D-12R-2 (662.7 mbsf; Fig. 23), or 128-794D-14R-2 (672.3 and 673.2 mbsf; Figs. 24 and 25). These fractures are probably early, as indicated by their complex filling history. Oriented conjugate sets were not recorded. Finally, some subvertical to vertical veins are filled either with green and white material (talc-chlorite and calcite) or with calcite alone, as in Section 128-794D-11R-2 (653.6 mbsf), or are still closed joints, as in Section 128-794D-13R-1 (666.5 mbsf). These represent probable tensional cracks and joints of different generations, but none are oriented.

It is difficult to decipher reliably the complete history of fracturing and vein-filling after only visual description and with the use of a hand-lens. More data, especially orientation constraints and detailed study of the vein material, will be necessary. For the moment, we can make only tentative assumptions. Regarding the vein-filling process, the calcite crystallization obviously post-dates a talc-chlorite crystallization stage; it is often found in the middle of the veins, grown on the green crystals (Figs. 23 and 24), and commonly displays a fibrous texture (Fig. 18). This texture means that crystallization and the opening of fractures were synchronous. At Section 128-794D-16R-1 (690 mbsf), a microgeode has been

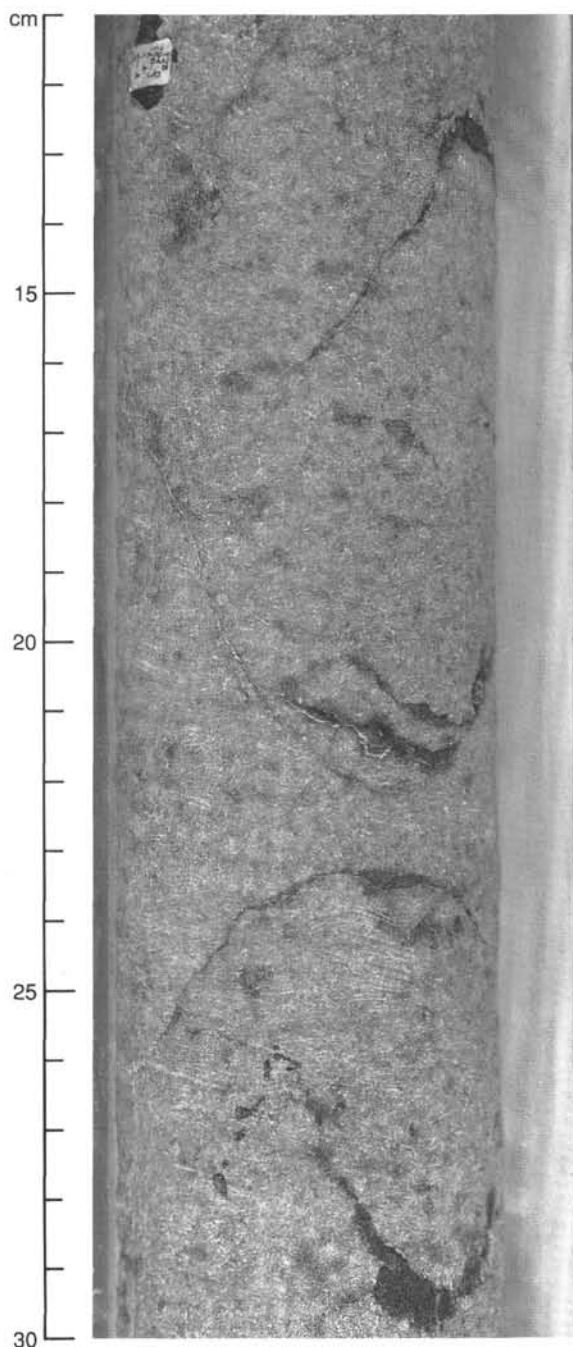


Figure 22. Conjugate normal shear joints in Section 128-794D-12R-3 from 11 to 30 cm.

filled in with zoned calcite at the walls and green material in the center, suggesting that formation of new clayey minerals took place after the calcitic stage. At Section 128-794D-14R-2 (672.3 mbsf), a wide (1 cm), light green, steep vein crosscuts a thin, dark green, gently dipping vein. This is evidence of at least two stages of talc-chlorite vein-filling. A summary of preliminary observations leads to a tentative assumption of at least four stages of crystallization: (1) talc-chlorite (+ pyrite), (2) talc-chlorite (+ quartz?), (3) calcite, and (4) green clayey minerals.

A working scenario for the chronologic relationships among different sets of fractures, from the more recent to the older features, is as follows: (1) normal faults with slickensides cutting the veins, (2) conjugate normal joints (and

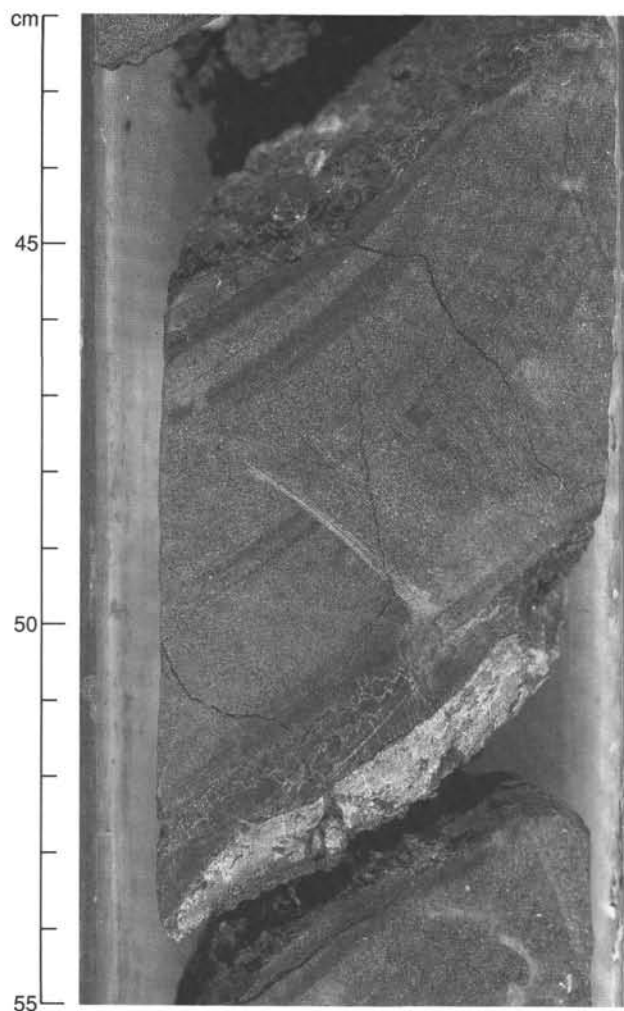


Figure 23. Veins inclined at about 50° (section slightly oblique to real dip) in Section 128-794D-12R-2 from 42 to 55 cm. Note the succession, from the edge to the center, of strips corresponding to alteration halo, talc-chlorite, and calcite, respectively.

vertical fissures?), (3) gently dipping joints, (4) steep (about 60°) veins and veinlets (and vertical ones?), and (5) gently dipping veins that are conjugate in places (and subhorizontal ones?).

The relative age of early fractures (relationships 4 and 5) is ambiguous. Some indications exist in favor of an older age for the low-angle fractures. For instance, at Section 128-794D-12R-3 (664.4 mbsf), a 30° inclined vein seems to be crosscut and offset by a steeper one; at Section 128-794D-12R-2 (663.4 mbsf; Fig. 26), a steep joint abuts a low-angle vein, thus is probably younger. In contrast, at Section 128-794D-13R-2 (668 mbsf), a steep joint is apparently offset by a flat vein (Fig. 27). In this case, at least the central filling of the flat vein, although not necessarily the whole flat fracture, is younger than the joint. According to the presently available data, an early north-northeast to south-southwest compression phase, affecting the basement igneous units, is plausible. Its consequences are not seen in the upper part, above Core 128-794D-10R. If confirmed by further study, this compressive stress system may be significant for the problem of initiation of the opening of the Yamato Basin. Actually, this is consistent with the stress system and right-lateral transpressive deformation occurring at that time (early Miocene) from Hokkaido to western Honshu (Jolivet, 1987; Kimura and Tamaki, 1986; Tamaki, 1988; Jolivet and Huchon, 1989) and, consequently,

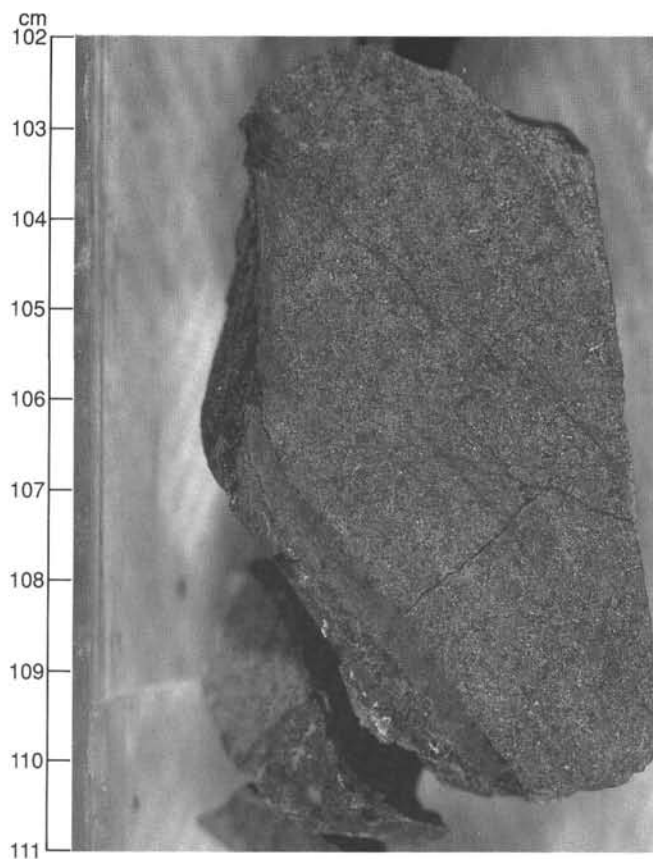


Figure 24. Steep veins (early conjugate(?) fractures) in Section 128-794D-14R-2 from 102 to 111 cm. Note the succession halo, talc-chlorite, and calcite.

with the hypothesis of a pull-apart mechanism (Lallemand and Jolivet, 1986; Jolivet, 1987).

Correlation with Leg 127 Holes 794B and 794C and with Unit Boundaries from Logging Data

Holes 794B and 794C, drilled during Leg 127, are located 170 m east of Hole 794D. A total of 32 m of igneous "basement" rock was recovered between 542.4 and 645.8 mbsf during Leg 127, with a recovery rate of 33% (Tamaki, Pisciotto, Allan, et al., in press). Scientists of Leg 127 distinguished six igneous lithologic units on the basis of petrographical and geochemical information. In addition, a sediment unit was cored between two igneous units. Figure 13 presents a correlation of Holes 794B and 794C with Hole 794D. By combining data from both legs, 184.7 m of predominantly igneous lithostratigraphy was established from 542.4 to 733.5 mbsf. Apart from the interbedded sedimentary unit, a total of nine igneous units can be recognized and distinguished as dolerite sills, doleritic basalt flows, or basalt flows. The thickness of each unit has been estimated by neglecting possible interbedded detrital layers, except for the recovered sedimentary Unit 5, and from logging data.

Unit 0 of Leg 128 Corresponds to Unit 1 of Leg 127 (Hole 794B)

Unit 0, the first encountered in Hole 794B during Leg 127 under a 542.4-m-thick sedimentary cover, was described by Tamaki, Pisciotto, Allan, et al. (in press) as a fine-grained, moderately plagioclase, phyric dolerite. The weak baking of the overlying claystone, as well as the chilled margin in the upper part of the dolerite and the texture of the rock, suggest

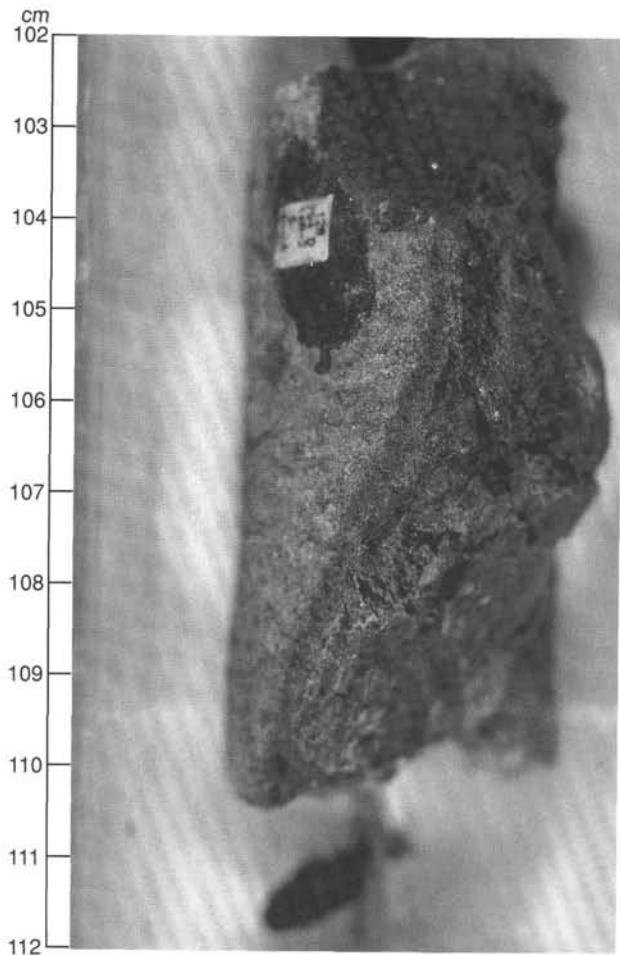


Figure 25. Peripheral view of veins, same interval as in Figure 24.

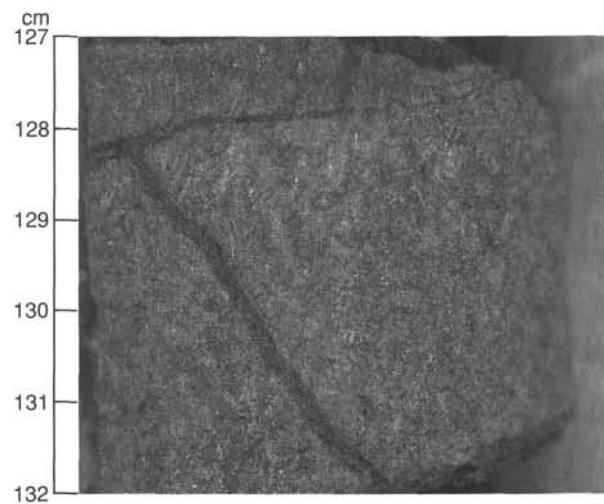


Figure 26. Steep early joint abutting low-angle ones in Section 128-794D-12R-2 from 127 to 132 cm.

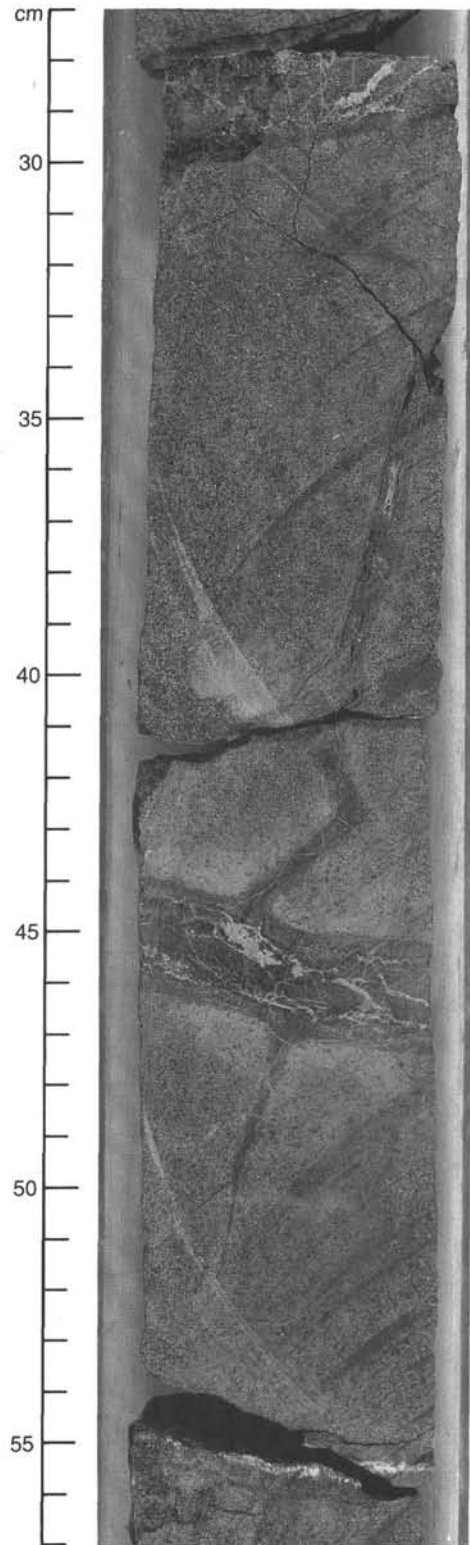


Figure 27. Intersection and offset of a steep joint-veinlet by a low-angle vein in Section 128-794D-13R-2 from 27 to 57 cm.

that this unit is a sill that was intruded into soft sediment at a shallow depth. The thickness from the observed upper contact to the presumed lower boundary in the logging data is less than 5 m.

Unit 1 (Hole 794D) Corresponds to Unit 2 of Leg 127 (Hole 794C)

From its petrographical composition and texture, Unit 2 of Hole 794C from Leg 127 is obviously the same as Unit 1 of Hole 794D from Leg 128. However, orthopyroxene, seen in Hole 794D, was not identified in Hole 794C (Tamaki, Pisciotto, Allan, et al., in press), perhaps because of its low abundance and random distribution. No contacts were observed, but in the lower part, the dolerite texture becomes microlitic, indicating proximity to the base. This massive, homogeneous, and highly resistive unit is well recorded in the logging data (see "Downhole Measurements" section, this chapter). The unit's top extends up to 546 mbsf, and its base is located at 593 mbsf (based on the NGT record). The FMS shows layering, several centimeters thick, that dips west between 589 and 591 mbsf. This layering and the cumulate petrographic texture suggest that this dolerite unit is a laccolith. Its total thickness reaches 47 m.

Unit 2 (Hole 794D)

This basalt was not recovered in Hole 794C during Leg 127. Either it may be missing or it may correspond to a void section in the core, although pieces of moderately plagioclase, phyrlic basalt found in the drilling rubble at the top of Core 127-794D-7R may belong to this unit (Tamaki, Pisciotto, Allan, et al., in press). The textural and vesicular features of Unit 2 indicate an outpouring into the uppermost soft sediments at a medium-to-great water depth (>2000 m?). It is 7 m thick, from 593 (upper altered part) to 600 mbsf.

Unit 3 (Hole 794D) Corresponds to Unit 3 of Leg 127 (Hole 794C)

These units from holes drilled during Legs 127 and 128 clearly correspond to the same dolerite sill. Subvertical fracturing was observed in both. Their approximate thickness is 7 m. Volcanic sand was sampled by the temperature tool at the base of this sill and was also logged from 607 to 608 mbsf (See "Downhole Measurements" section, this chapter).

Unit 4 (Hole 794D) Corresponds to Units 4 and 5 of Leg 127 (Hole 794C)

This dolerite resembles Unit 3 and is distinguished only by a difference in rock chemistry (see below). In Hole 794C, the occurrence of a fine-grained section having a slight chemical change (decrease in nickel and in chondrite normalized niobium/zirconium) was used by the Leg 127 scientists to subdivide the unit into two subunits. Such a distinction was not observed in Hole 794D during Leg 128, but owing to the poor recovery, the existence of two superimposed sills is possible. The upper boundary is located at about 607 mbsf, beneath the volcanic sand. The lower contact with baked sediment is seen in Hole 794C at 644 mbsf. The same sedimentary unit was cored in Hole 794D at 642 mbsf. The logging record shows the lower, partly altered portion and its contact with sediment (Unit 5) at about 641 mbsf. Therefore, the sill reaches 34 m thick.

Unit 5 (Hole 794D) Corresponds to Sedimentary Unit V of Leg 127 (Hole 794C)

The 1.60 m of silty clay and clayey tuff of Hole 794D obviously corresponds to the 1.05 m tuff and tuffaceous claystone of Hole 794C.

Unit 6 (Hole 794D) Corresponds to Unit 6 of Leg 127 (Hole 794C)

The same basalt flow, with a chilled and highly altered upper margin, underlies a sediment bed (Unit 5) in both holes.

The record for Hole 794C ends in the chilled upper part at 645.8 mbsf. The contact with the sediment is fairly sharp and without important observable baking, supporting the contention that Unit 6 is a lava flow. The hydroclastic volcanic material in the lower clayey beds of Unit 5 (Hole 794D) is most probably linked to this same volcanic activity. The Unit 6 flow includes doleritic inner and lower parts and has a total thickness of 19 m.

The following three units were not recovered in Hole 794C, but are presented here to complete the information about unit boundaries.

Unit 7 (Hole 794D)

This unit is heterogeneous, probably with some subunits of different grain size from 661 to 687 mbsf, as determined from the logging record, and was observed in the portions of core that were recovered. Between 676 and 682 mbsf, the rock is highly fractured and altered. Total thickness of the unit is 26 m.

Unit 8 (Hole 794D)

The upper chilled and altered part of the flow is well recognized in core from 689 to 691 mbsf. The inner part is homogeneous until 702 mbsf. Below an altered zone, the base of the unit is heterogeneous until 712 mbsf. The unit reaches 25 m thick.

Unit 9 (Hole 794D)

The top of this dolerite sill corresponds to a sharp increase in resistivity and to high *P*-wave velocities at 712 mbsf (See "Downhole Measurements" section, this chapter). This dolerite was cored to 727.1 mbsf. The finer grain size of the deepest samples might indicate either the approaching base of the sill or only an inner textural variation, such as was observed in Unit 7.

Sequence of Igneous Events and Relative Ages

The texture of the basaltic lavas indicates that they erupted at medium-to-great water depth into the upper part of a soft sediment pile. This common setting of subaqueous volcanic flows in a sedimentary basin is well illustrated by the Unit 6 basalt and its penecontemporaneous clay and hydroclastic tephra deposit. It is also probable that the fine-grained dolerite (Unit 0) was intruded under a thin sediment cover. In contrast, the medium- to fine-grained doleritic sills (Units 1, 3, 4, and 9) were probably intruded under a thicker cover after the basaltic outpouring. This reasoning indicates the initial chronologic succession of magmatic events within the effusive sequences: Unit 8—Unit 7—Unit 6—Unit 2—Unit 0.

Generally, in an interbedded succession of basalts and sediments, the doleritic sills are preferentially found just beneath the basaltic layer, which behaves as a screen or a barrier to the new magma supply. Each subsequent intrusion takes place beneath the former sill, unless the upper volcanic pile was fractured, in which case the magma may reach the upper strata and even the seafloor to produce a lava flow. This behavior gives the ordering of a basaltic to doleritic sequence such as Unit 2—Unit 3—Unit 4. Using these guidelines, we determined that the overall chronologic succession of the igneous events at Site 794 was as follows: Unit 8—Unit 9—Unit 7—Unit 6—Unit 2—Unit 3—Unit 4—Unit 0—Unit 1.

No sediments were found below the submarine basalt flow of Unit 6, although logging suggests that either sediment or altered basalt, not recovered in core, occurs in the lower parts of the hole (See "Downhole Measurements" section, this chapter). We inferred that this flow corresponds to the top of basement. This inference also was based on abrupt changes in

concentrations of trace elements in the rocks (see below) and on the development, in Units 6 to 9, of hydrothermal mineralization consisting of talc, chlorite, quartz, pyrite, and calcite. Thus, two volcanic complexes can be distinguished: a lower complex consisting of Units 6 to 9, and an upper complex consisting of Units 0 to 4. The successive supply of the nine magmatic pulses is interpreted in Figure 28. The basalt lava flows of the upper volcano and partly sedimentary complex, in the time sequence of Unit 6 followed by Unit 2 and Unit 0, gives us the relative successive levels of the sea bottom. The last magmatic supply (Unit 1) was accumulated as a laccolith under a moderately thick sedimentary pile, although the volcanic complex was probably more or less contemporaneous with the sediments. Tamaki, Pisciotto, Allan, et al. (in press) estimated that the age of the overlying sediments was between 15.8 and 16.5 Ma; therefore, we inferred that the volcanic complex was emplaced during the late early to early middle Miocene.

Whole-Rock Chemistry and Magmatic Affinity

Chemical Distinction

A total of 16 XRF analyses for major and trace elements were performed on board the ship (Table 2). The different volcanic units are represented, except for dolerite Unit 3, which was poorly cored and returned only a few altered and fractured samples. Loss on ignition (LOI) is commonly high, about >4% in altered samples where the amount of secondary minerals is >50%. According to correlations between the LOI and relative abundances of elements, alteration has resulted in increased magnesium, alkalis, and rubidium.

SiO₂ ranges from 48.42% to 52.10%. Al₂O₃ is high: 15.04% to 20.11%. The magnesium ratio, defined as Mg/(Mg + Mn + calc. Fe²⁺), varies from 0.515 to 0.685, but has been influenced by alteration, as has the total content of alkalis of 2.74 to 5.23. Contents of TiO₂ is consistent in all samples, with an average of 1.41%. Most of the trace elements vary within a short range. Good agreement exists between the chemical compositions and the petrographic modes, with for example, the olivine basalt (Unit 6) having high magnesium, chromium, and nickel contents and the plagioclase cumulophyric dolerite (Unit 1) having high aluminum, strontium, and barium contents.

The 17 XRF analyses of the equivalent units of Leg 127 (Tamaki, Pisciotto, Allan, et al., in press) were combined with the 16 analyses from this study (Table 2) to obtain as complete an understanding as possible of the igneous rocks at Site 794. In the following diagrams of elemental abundances and ratios, the units are ordered in their assumed chronological succession (see above). In Figures 29 to 31 we present the chronological evolution of some major and minor elements in which the samples have been plotted sequentially from youngest to oldest. In addition, evidence of geochemical evolution is shown by the antipathetic behavior of chromium and barium in Figure 32. To distinguish chemical groups, it is necessary to select the well-measured elements and discard, first, the elements that were influenced by alteration, and, second, the elements that were involved in differentiation processes. A common way of doing this is to use incompatible elements combined in binary diagrams, for example, barium, niobium, zirconium, and yttrium. In such diagrams, co-genetic lavas normally plot along a straight line from the most primitive to the most evolved compositions. In Figures 33 and 34, the units clearly are distributed into two main groups that correspond to the upper and lower complexes. One group representing the lower complex includes Units 7, 8, and 9. The other group representing the upper complex includes Units 0, 1, 2, 3, and 4. In some cases, a further distinction can perhaps be made for

the latter into another subgroup (Units 2 and 3) having an intermediate niobium and barium content between samples of the lower and upper complexes. The analyses of Unit 6 show that it has a more primitive composition than all the other units and plot either on the line for the lower complex (yttrium-zirconium), or on the line for the upper complex (yttrium-barium, barium-zirconium). On the combined diagram zirconium/yttrium vs. zirconium (Fig. 35), the two magmatic groups are well distinguished by their different zirconium/yttrium ratios. Unit 6 appears to be the primitive magma of the lower complex. Consequently, the ratios of these discriminant elements have been used to characterize the chemical composition of the units in Figure 13.

In conclusion, there are two distinct magmatic complexes that correspond to the two volcanic complexes: a lower complex consisting of Units 9 to 7 and an upper complex consisting of Units 4 to 0, with Unit 6 being an intermediate magmatic event of primitive composition.

Magmatic Affinity

The petrographical features are clearly related to the tholeiitic magmatic series *sensu lato* in which the order of "dry" crystallization commences with the development of abundant plagioclase, followed by clinopyroxene in an interstitial to subophitic texture. The overall chemical compositions are in agreement with this classification.

If "Normal-Mid-Ocean-Ridge Basalt" (N-MORB)-normalized values of the cerium/yttrium ratio obtained by shipboard XRF analysis (Fig. 36) are used as a substitute for the conventional light rare earth elements/heavy rare earth elements ratio, the units are either very slightly enriched (lower complex) or slightly enriched (upper complex and Unit 6) in light rare earth elements, compared to N-MORB. The niobium content is not enriched (lower complex) or slightly enriched (upper complex and Unit 6), compared to N-MORB (Fig. 33). Concerning the large ion lithophile elements, except for a few samples having anomalously low barium and rubidium values and discarding potassium values (affected by alteration), all the units are enriched in rubidium, barium, and strontium. This enrichment is more pronounced in the upper complex, including Unit 6 (Fig. 34). However, interpretation of this observation must be tempered with the knowledge that interaction between seawater and basalt gives increased contents of potassium, rubidium, and strontium.

The above characteristics may be ascribed either to an island-arc tholeiite series or a back-arc tholeiite series (Saunders and Tarney, 1984). However, there is a clear evolution from the lower complex to the upper complex toward a more calc-alkali composition. This trend is emphasized mineralogically by the crystallization of orthopyroxene in the dolerite Unit 1, which is the most evolved lava of the upper complex. Pearce and Cann's (1973) titanium-zirconium diagram is consistent with these magmatic signatures (Fig. 37): the analyses of the lower complex plot in the "Ocean-Floor Basalt" (OFB) area and exclude "Low-K Tholeiite" (LKT) and "Calc-Alkali Basalt" (CAB). Analyses of the upper complex are distributed between the two OFB and CAB areas. In Pearce's (1982) chromium-yttrium discrimination diagram (Fig. 38) the lower complex may belong to a "Mid-Oceanic Ridge Basalt" (MORB) series or a "Back-Arc Basalt" (BAB) series. The upper complex belongs to the "Island-Arc Tholeiite" (IAT) series.

The older and lower magmatic complex has been tentatively interpreted as an OFB of back-arc tholeiitic composition (large ion lithophile element-enriched), whereas the younger and upper complex belongs to an IAT series. However, such a superposition is inconsistent with the normal magmatic evolution of a back arc in a geodynamic context,

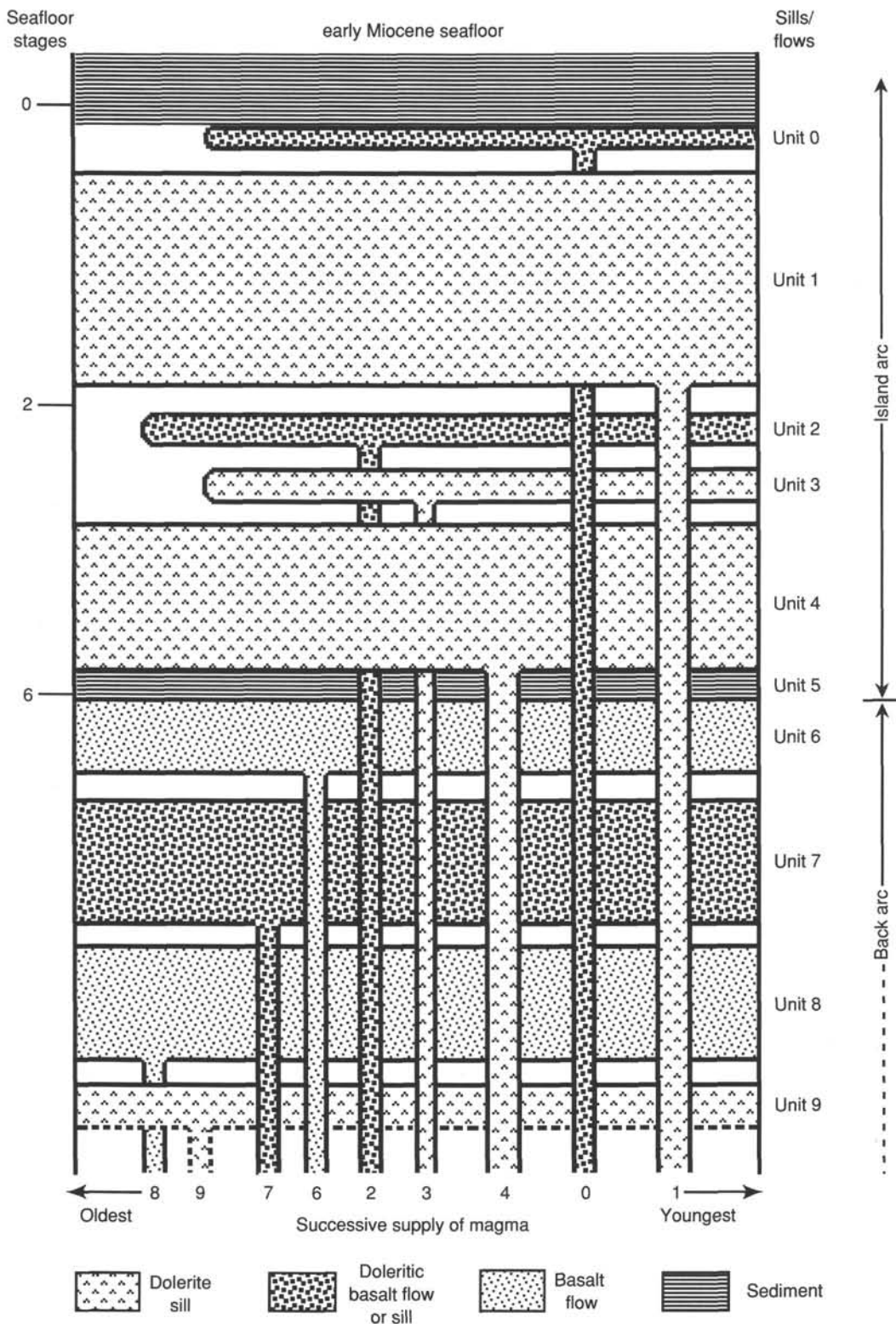


Figure 28. Schematic diagram of the igneous basement sequence drilled at Site 794, representing early Miocene seafloor and crust beneath the Yamato Basin, Japan Sea. Seafloor stages 0, 2, and 6 represent the relative position of the seafloor at the time that Units 0, 2, and 6 were emplaced, i.e., these units were emplaced at or near the seafloor. Other units were emplaced beneath the seafloor. Units are shown in contact only when the actual contact was observed in the cores. The unit numbers in the lower part of the diagram are shown to stress that the stratigraphic position of the units does not represent the order in which they were emplaced.

Table 2. XRF analysis of trace and major elements in igneous rocks from Hole 794D.

Section: Interval (cm): Unit:	1R-1 96-101 1	3R-3 89-94 1	4R-1 32-37 2	7R-2 8-10 4	8R-2 126-130 4	9R-2 16-20 4	10R-2 70-74 6	11R-1 89-95 6	12R-3 36-40 7	13R-1 81-84 7	14R-1 81-84 7	16R-1 67-70 8	17R-1 97-100 8	18R-1 44-47 8	19R-1 11-14 9	20R-1 20-23 9
<i>Major elements</i>																
SiO ₂	50.64	50.04	52.10	51.27	50.63	51.23	51.01	48.58	48.87	48.64	49.20	50.01	48.84	49.37	48.42	47.73
TiO ₂	1.31	1.27	1.06	1.44	1.29	1.40	1.09	1.11	1.64	1.51	1.64	1.63	1.54	1.67	1.51	1.48
Al ₂ O ₃	19.56	18.11	17.36	16.56	16.35	17.23	16.48	16.15	15.80	15.04	15.11	20.11	17.56	17.80	17.30	16.65
Fe ₂ O ₃	10.24	10.01	8.56	9.13	9.61	9.11	9.92	10.26	11.84	11.55	11.66	8.49	9.96	8.68	10.53	10.64
MnO	0.13	0.12	0.23	0.12	0.12	0.13	0.14	0.16	0.18	0.18	0.21	0.22	0.28	0.27	0.20	0.21
MgO	6.40	6.57	11.04	10.63	11.12	11.28	14.26	12.43	7.43	8.26	7.08	7.65	7.49	7.39	7.99	9.36
CaO	8.91	9.50	5.41	8.18	7.86	6.77	2.76	7.75	10.86	10.63	10.82	7.91	10.79	10.76	10.61	10.18
Na ₂ O	3.46	3.25	3.24	2.98	2.91	3.25	2.21	2.49	2.99	2.83	3.17	3.34	2.65	3.02	2.91	2.82
K ₂ O	0.61	0.62	1.54	0.59	0.69	0.64	3.02	0.25	0.12	0.24	0.24	0.45	0.21	0.22	0.20	0.22
P ₂ O ₅	0.20	0.21	0.17	0.21	0.19	0.20	0.16	0.15	0.13	0.16	0.17	0.25	0.18	0.19	0.17	0.17
Total	101.47	99.70	100.72	101.10	100.79	101.25	101.05	99.34	99.87	99.04	99.28	100.06	99.49	99.37	99.85	99.46
LOI	2.16	1.73	4.70	2.60	4.13	3.02	5.01	4.02	0.90	0.76	1.25	4.57	2.65	2.26	2.44	2.18
Mg-ratio	53.35	53.59	68.99	67.16	67.05	68.48	71.61	67.97	52.37	55.61	51.46	60.90	56.46	59.39	56.96	60.52
<i>Minor elements</i>																
Nb	6	7	4	11	8	9	3	2	3	3	3	4	2	3	2	2
Zr	85	90	85	100	93	99	41	41	96	90	95	131	97	107	92	92
Y	20	20	21	22	21	20	15	16	34	31	33	29	31	33	29	28
Sr	395	370	238	279	246	277	171	277	196	194	191	263	181	200	185	173
Rb	6	7	9	4	7	5	13	0.4	1	3	4	5	3	3	3	2
Zn	28	49	57	36	44	49	28	47	75	85	91	108	77	83	81	53
Cu	30	34	39	56	46	51	18	54	58	63	63	55	61	74	60	56
Ni	12	21	182	88	159	126	128	147	82	129	117	113	108	124	137	124
Cr	47	79	358	216	313	266	341	377	288	324	311	329	283	319	312	291
V	272	238	257	289	252	278	250	256	271	245	284	278	255	281	232	234
Ce	22	14	19	35	25	22	6	18	23	19	27	33	24	31	22	12
Ba	122	154	143	133	129	121	89	57	48	21	11	58	10	6	12	53

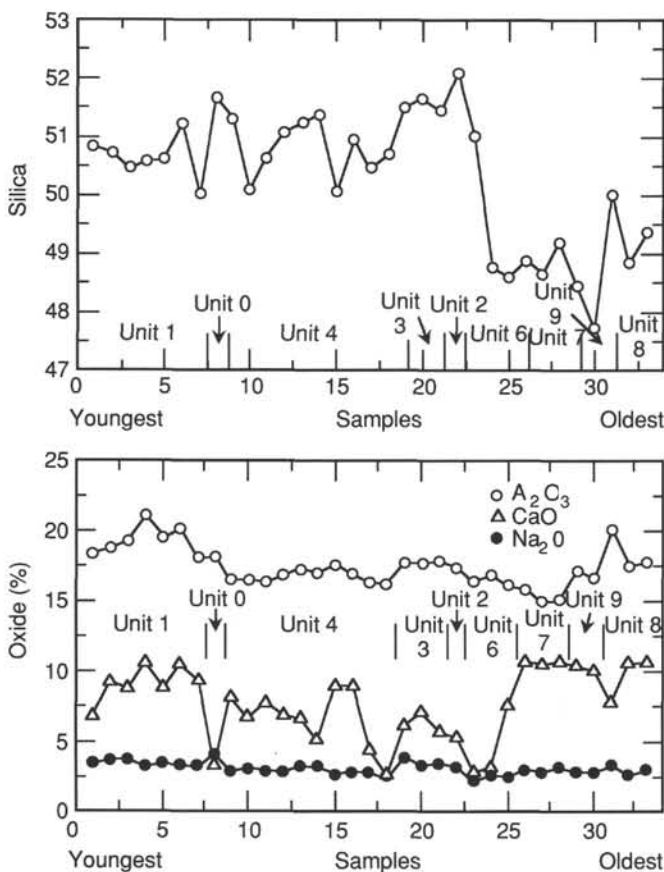


Figure 29. The contents of some major elements in samples, arranged in their proper chronologic order from youngest to oldest. Locations of units also are shown. Data are from Table 2.

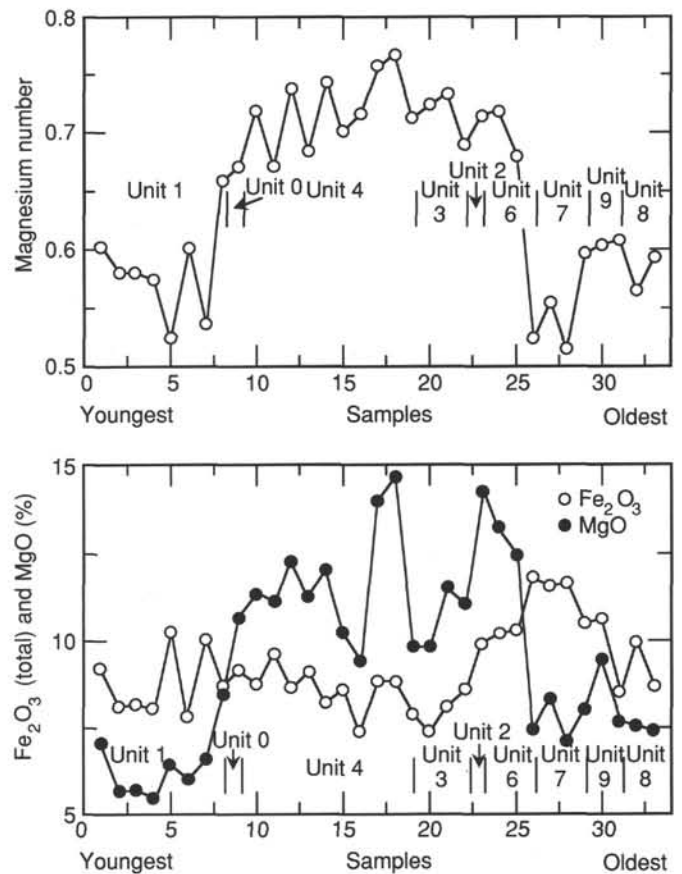


Figure 30. Magnesium numbers of total iron as Fe₂O₃ and MgO in samples, arranged in their proper chronologic order from youngest to oldest. Locations of units are shown. Data are from Table 2.

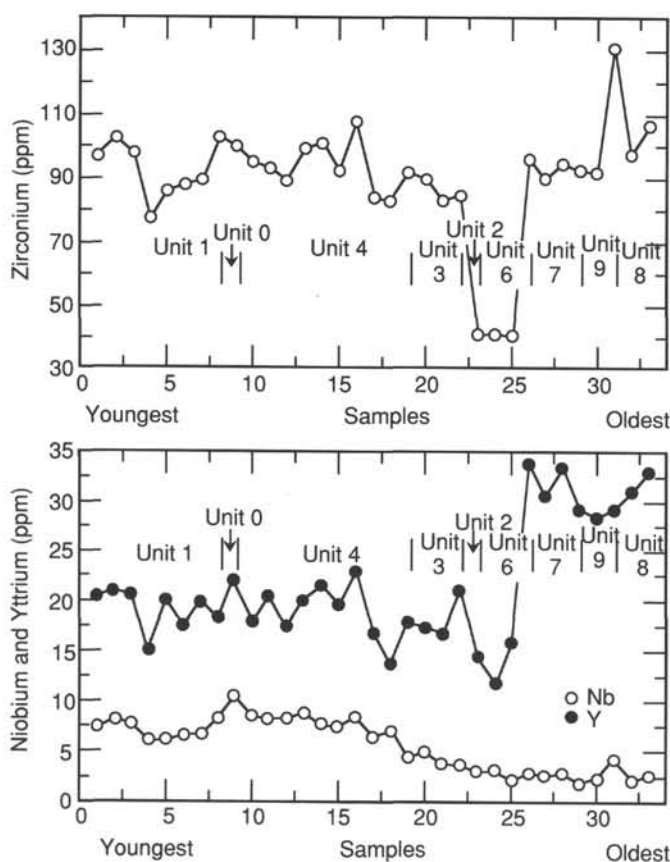


Figure 31. Contents of the trace elements zirconium, niobium, and yttrium in samples, arranged in their proper chronologic order from youngest to oldest. Locations of units are shown. Data are from Table 2.

where the back-arc magma has been generated during and after splitting of the volcanic arc, resulting in the younger BAB more or less overlying the IAT. The two volcanic complexes were emplaced successively during a relatively-short period of time and in the same tectonic context, thus they cannot have originated from sources very far removed from one another.

Alternatively, the lower volcanic complex may be the remnant of the initial magmatic activity of an immature volcanic arc generated from depleted upper mantle. This remnant may constitute the basement of the upper volcanic complex, which we have attributed to the development of the succeeding, present-day, island arc. The seeming contradictions of magma provenance, as given by trace-element signatures cannot be resolved from shipboard analyses alone and will have to await further chemical and isotopic study.

BIOSTRATIGRAPHY

Introduction

Microfossils were observed in a 2.52-m-thick sediment layer near the bottom of Hole 794D. This sediment is interbedded between a basalt flow below and a dolerite sill above, and in each case, the nature of the contact was indistinct. Based upon its stratigraphic setting and the depth of occurrence, it appears to be identical to what was referred to as a tuff by scientists of Leg 127 (Tamaki, Pisciotto, Allan, et al., in press). Microfossils are present, but occur rarely. Spongodiscidlike radiolarians are the most common, followed by benthic foraminifers and diatoms. No single microfossil group

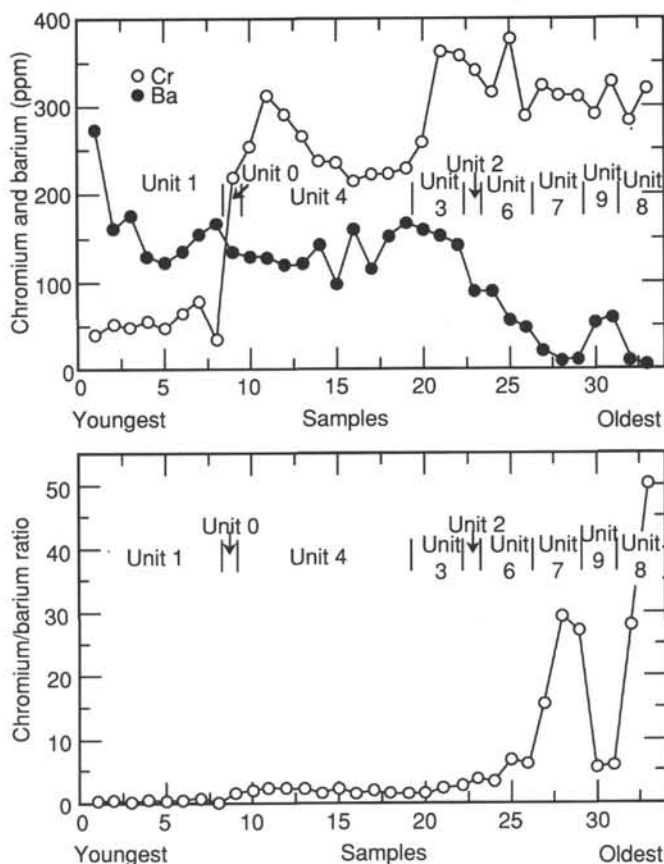


Figure 32. Variations in chromium, barium, and chromium/barium ratios in samples, arranged in their proper chronologic order from youngest to oldest. Locations of units are shown. Data are from Table 2. Changes in contents of chromium and barium with age are as expected for a fractionating magma, with chromium precipitating in spinel phases and barium in feldspar.

can be used to interpret this sediment; however, when combined, these groups give a temporal and spatial picture of the Japan Sea that is not inconsistent with that presented in the Leg 127 Initial Reports volume (Tamaki, Pisciotto, Allan, et al., in press). All microfossils observed in this sediment exhibit signs of dissolution or recrystallization.

Microfossils

As noted above, radiolarians are common in Section 128-794D-10R-1, 26–30 cm. Unfortunately, they have recrystallized so that the internal structure, and frequently the surface structure, has been obscured, if not completely destroyed. This made identification at the species or even generic level impossible. Diatoms also exhibited evidence of recrystallization, but not to the extent that the surface structure was completely destroyed. We did observe two species: *Thalassionema nitzschoides* and *Coscinodiscus curvatulus*. Both species are found in present-day waters of the northwest Pacific and the Japan Sea. To our knowledge, they do not occur before the Neogene. If we place our meager age data within the stratigraphic and chronostratigraphic context of Site 794 (Tamaki, Pisciotto, Allan, et al., in press), then we would have to conclude that Section 128-794D-10R-1, 26–30 cm, is Neogene in age and correlative with the early or middle Miocene.

Paleoenvironment

The various microfossil groups observed in Hole 794D, although rare and generally in a poor state of preservation,

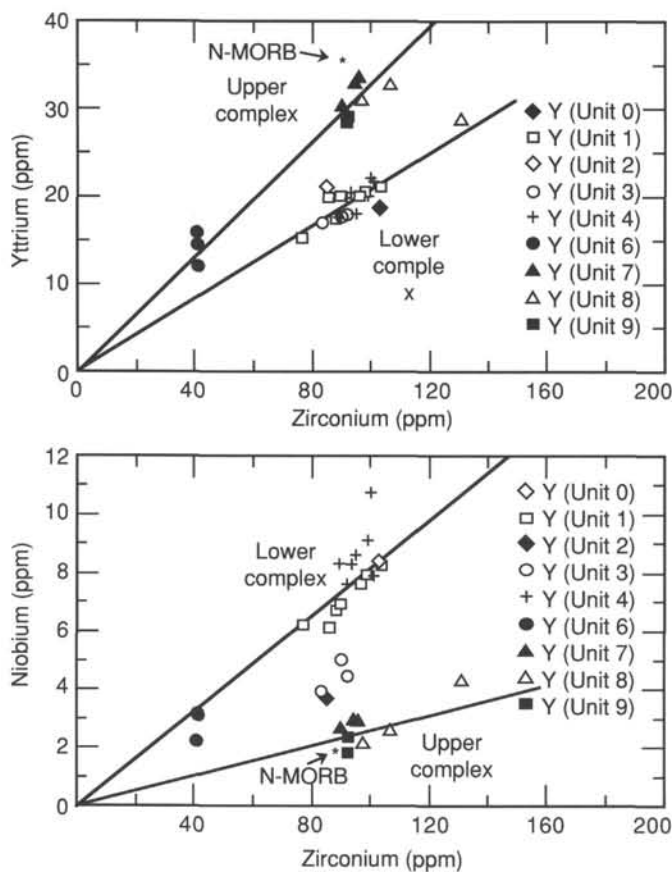


Figure 33. Variations in the incompatible elements yttrium (upper) and niobium (lower) with zirconium. Two chemical groups, corresponding to the upper and lower complexes, are distinguished. Lavas of Unit 6 are more primitive. Data are from Table 2.

give a rather consistent picture of the environment of deposition. The presence of the diatom species mentioned above indicates that the sediments were deposited in a marine environment. Radiolarians species indicate that it was an open-ocean marine environment. Finally, the presence of the benthic foraminifer *Cyclammina* sp. suggests a deep-water marine environment, not unlike the present-day water depth at Site 794. Thus, the micropaleontological data suggest rapid subsidence occurred at this site during the late early Miocene shortly after the opening of the Japan Sea.

PALEOMAGNETISM

Introduction

A total of 160.5 m of igneous rock was drilled; 34.85 m of this was recovered in Hole 794D. The drilled section was divided into nine lithologic units, based on lithologic and paleomagnetic studies. The upper six units were previously observed in Holes 794B and 794C, drilled during Leg 127. These igneous-rock units consist of five dolerite sills, three basalt flows, and a thin layer of sediments (see "Igneous Rocks" section, this chapter).

Experimental Procedures

A total of 33 minicore samples were taken from the recovered cores, with a sampling frequency of one sample per section. Because of the low recovery rate, only one sample was taken from Cores 128-794D-1R, 128-794D-4R, 128-794D-15R, 128-794D-16R, 128-794D-17R, and 128-794D-20R. The

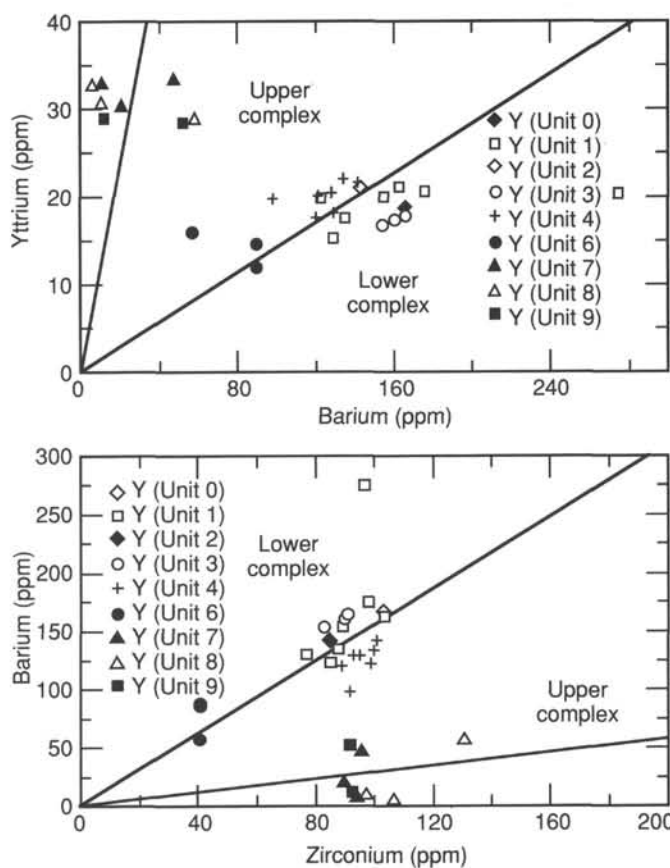


Figure 34. Variations among yttrium, barium, and zirconium contents. Two chemical groups are distinguished, as in Figure 33. Data are from Table 2.

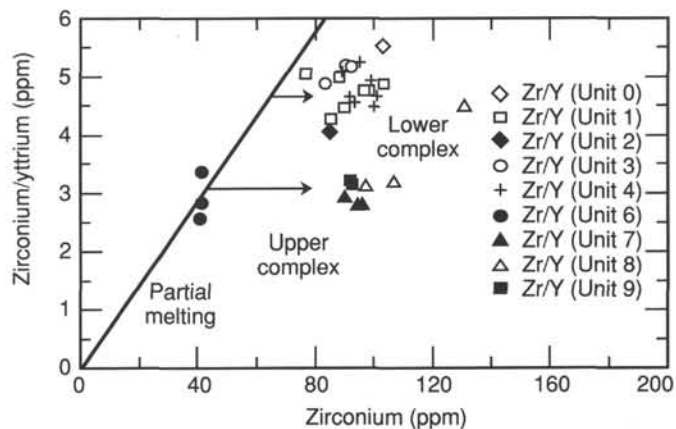


Figure 35. Plot of zirconium/yttrium ratio vs. zirconium. Two chemical groups, corresponding to the upper and lower complexes, are distinguished by their different zirconium/yttrium ratios and degrees of partial melting. Unit 6 is a primitive magma belonging to the upper complex. Data are from Table 2.

magnetic remanence of these minicore samples was measured with a minispin spinner magnetometer having demagnetization steps of 0, 2, 5, 10, 15, 20, 30, and 40 mT. These steps were sufficient to isolate the stable components of the remanence in these samples. Magnetic susceptibility then was measured with a Bartington susceptibility meter.

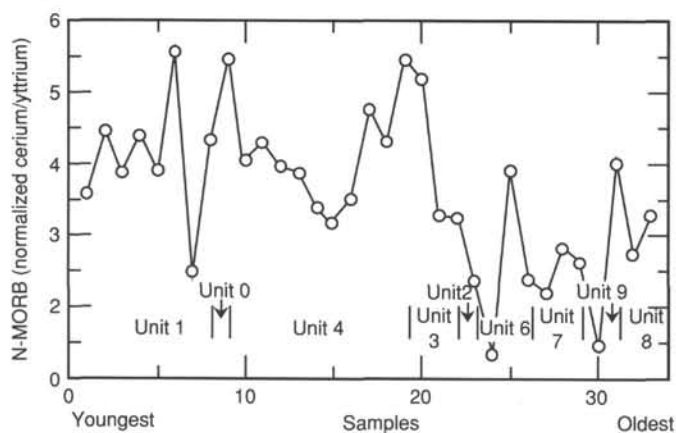


Figure 36. N-MORB normalized cerium/yttrium ratios of samples arranged in their proper chronologic order from youngest to oldest. Cerium/yttrium ratios from shipboard XRF analyses are used as a substitute for LREE/HREE ratios. Locations of units are shown. Data are from Table 2.

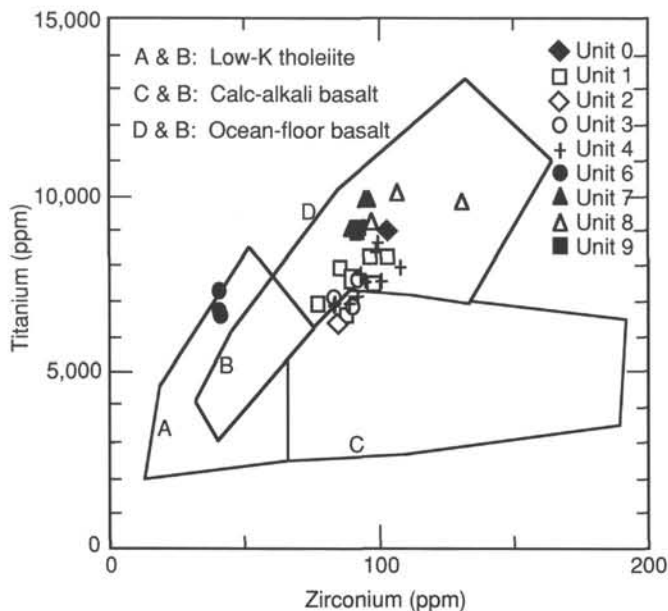


Figure 37. Titanium-zirconium diagram (Pearce and Cann, 1973) for the igneous units of Site 794. Data are from Table 2.

Results

Results of the paleomagnetic measurements are listed in Table 3, where natural remanent magnetization (NRM) declination, stable declination, NRM inclination, stable inclination, NRM intensity, and susceptibility values are shown for all the samples, along with the depth below seafloor. Stable inclination and NRM intensity are also plotted as a function of depth below seafloor in Figure 39.

Two components of the remanence, the so-called soft component, which has a secondary origin, and the stable component, were identified in most of the samples. Although the intensity of the soft component was high, it could be easily demagnetized at the alternating field (AF) of 5 mT. The stable component was isolated beyond this demagnetization level. Examples of the variation of the remanence during the demagnetizations are shown in Figure 40. The soft components of Samples 128-794D-10R-1, 56 cm; 128-794D-8R-2, 74 cm;

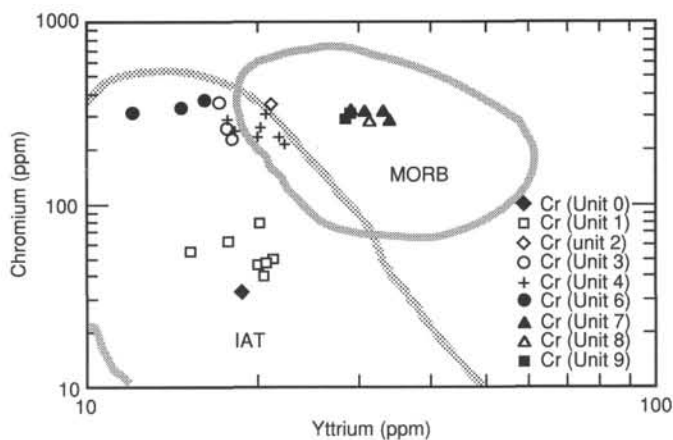


Figure 38. Chromium-yttrium diagram (Pearce, 1982) for the igneous units of Site 794. Data are from Table 2. MORB = mid-ocean ridge basalt; IAT = island-arc tholeiite.

128-794D-3R-1, 67 cm; 128-794D-2R-1, 44 cm; and 128-794D-1R-2, 14 cm, have negative inclinations, whereas the component of all the other samples have high positive inclinations. Thus, the origin of the soft component is not clear, although viscous remanent magnetization (VRM) or the remanence acquired during drilling are the most provable causes of this remanence.

NRM intensity of the igneous rocks ranges from 186 to 11472 mA/m, with a mean of 1735 mA/m for 31 samples. Contrary to this wide variation of NRM intensity, magnetic susceptibility is confined within a narrow range with a mean and a standard deviation of 2639 and 659, respectively. This feature can be clearly seen in the NRM intensity vs. susceptibility relationship shown in Figure 41. Because the value of the magnetic susceptibility is proportional to the amount of magnetic minerals in a rock, the variation of the NRM intensity cannot be attributed to the variation of the concentration of the magnetic carriers. Probably, the grain size of the magnetic grains controls the NRM intensity.

As is evident from Table 3, NRM inclination gives scattered values. However, the stable inclination, obtained by AF demagnetization, gives a consistent value within each lithologic unit. Note that all the igneous-rock samples, except samples taken between 645 and 654 mbsf, have negative inclinations.

The two sediment samples we analyzed (128-794D-10R-1, 56 cm, and 128-794D-10R-1, 136 cm) are characterized by their low NRM intensities and low magnetic susceptibilities. However, their remanence properties are different. The variation of their remanence during AF demagnetization is shown in Figure 42. The remanence of Sample 128-794D-10R-1, 56 cm, has essentially one component having a shallow inclination. Alternatively, Sample 128-794D-10R-1, 136 cm, has a remanence that consists of two components: the direction of the soft component is similar to that of the upper sample, while the stable component has a positive inclination. Because this latter sample is near the underlying basalt flow (which has a positive inclination), the stable component must have been acquired as a result of heating by the basalt flow. Hence, we can conclude that the sediment layer pre-dates the underlying basalt flow.

Discussion

Stable inclination and NRM intensity for seven lithological units (see "Igneous Rocks" section, this chapter) are summarized in Table 4. None of the samples taken from Units 3 and 5 correspond to a sediment layer. Hence, these units have been

Table 3. Results of paleomagnetic measurements for Hole 794D.

Core, sample interval (cm)	Depth (mbsf)	NRM declination (degrees)	Stable declination (degrees)	NRM inclination (degrees)	Stable inclination (degrees)	NRM intensity (mA/m)	Susceptibility
128-794D-1R-2, 14-16	574.64	233.9	211.1	-21.9	-31.1	955	2941
2R-1, 44-46	581.04	302.3	213.4	-52.1	-29.7	712	—
2R-2, 30-32	582.40	22.3	33.5	-13.4	-35.4	735	2412
3R-1, 67-69	586.57	339.0	334.6	-37.1	-28.2	1572	2812
3R-2, 69-71	587.99	254.2	224.9	-3.8	-21.8	362	3492
3R-3, 28-30	589.03	150.9	149.4	-45.9	-38.3	844	3824
4R-1, 39-41	595.79	154.4	133.1	-70.7	-61.8	850	1828
7R-1, 39-41	619.39	286.1	232.4	72.7	-27.1	1540	4231
7R-2, 81-83	621.31	118.4	191.3	81.7	-24.8	597	1942
8R-1, 18-20	623.68	16.4	83.5	-31.9	-44.4	783	2965
8R-2, 74-76	625.74	248.8	198.2	-58.5	-38.5	512	3010
9R-1, 58-60	633.58	353.6	355.0	-24.3	-37.0	2329	3118
9R-2, 46-48	634.81	324.0	230.3	30.2	-27.9	186	2523
10R-1, 56-58	642.76	300.4	294.6	-10.1	7.0	3	58
10R-1, 136-138	643.56	282.1	233.9	46.3	61.4	8	114
10R-2, 96-98	644.66	180.6	178.5	44.4	48.5	4385	2345
11R-1, 107-109	652.47	331.9	335.1	47.0	45.1	2299	2274
11R-2, 37-39	653.19	154.0	155.2	55.0	49.6	2335	2814
11R-3, 27-29	654.39	281.0	277.4	51.4	47.0	3661	2692
12R-1, 69-71	661.39	356.1	229.6	-87.5	-69.9	1685	1960
12R-2, 118-120	663.38	356.1	335.1	-53.0	-68.3	1711	1869
12R-3, 20-22	663.88	316.7	249.2	-49.2	-64.9	2563	1575
13R-1, 74-76	666.74	230.7	195.5	-65.6	-59.9	1790	2237
13R-1, 87-89	666.87	313.5	199.0	-20.1	-66.2	665	2004
13R-2, 64-66	668.14	296.9	276.0	-57.8	-61.2	572	2696
14R-1, 88-90	671.38	26.5	67.5	28.5	-72.9	1011	2095
14R-2, 76-78	672.56	282.3	216.7	-71.2	-71.2	929	2912
14R-2, 136-138	673.16	345.3	342.2	50.1	-70.7	2742	2341
15R-1, 64-66	680.54	343.0	304.3	17.3	-15.0	419	3302
16R-1, 110-112	690.40	228.6	225.2	-62.1	-62.1	11473	2503
17R-1, 38-40	698.98	25.8	13.1	-17.7	-60.3	712	2458
18R-1, 16-18	708.06	18.3	64.9	15.0	-60.9	838	3831
20R-1, 5-7	726.65	302.2	293.6	-54.1	-56.1	2018	2151

omitted. As shown in Table 4, data indicate that the intensity of the basalt flows tends to have higher values than that of the dolerite sills. This tendency probably reflects the smaller grain size of the basalt flows, which results from the higher cooling rate of the flow relative to the dolerite sills. One should also note that the lower unit has a higher intensity in each rock type, although the reason for this feature is not clear.

Units 1 and 4 are thick, dolerite sills having about the same thickness (see "Igneous Rocks" section, this chapter). Both units have negative inclinations of about -30° . Because the inclination of the geocentric axial dipole field at Hole 794D is 59.5° , the inclination value of the two units is too shallow to be explained by a secular variation of the geomagnetic field. We infer that block rotation of these units after solidification is the cause of this shallow inclination.

Angular standard deviation of the geomagnetic field at this latitude is about 10° . Hence, the inclination values of other units are within the range of the secular variation of the Earth's field. However, note that six out of seven units have negative inclinations. During the Miocene, the average period of each polarity was about 300,000 yr. Hence, the patterns in the Site 794 igneous sequence suggest that the volcanic activity responsible for the entire drilled section of volcanic rocks may have occurred within a few hundred thousand years. If more than 1 m.y. was required for this activity, then the age of the activity is probably between 15 and 16 Ma, when a long reverse-polarity period existed.

PHYSICAL PROPERTIES

Introduction

Coring at Hole 794D penetrated a 160-m-thick section of igneous and sedimentary rocks. Physical properties analyzed

in samples from this sequence consisted of 2-min GRAPE (bulk density), thermal conductivity, compressional-wave velocity, and index properties, such as wet-and dry-bulk densities, water content (expressed as weight of water relative to total dry weight), grain density, and porosity. The methods used are described in detail in the "Explanatory Notes" (this volume).

Wet-Bulk Density

Wet-bulk density, as determined from 2-min GRAPE counts, generally varies from 2.11 to 2.80 g/cm³ (Table 5). A minimum value was determined in the sedimentary section recovered from Core 128-794D-10R. A maximum value was determined for Core 128-794D-14R. Wet-bulk densities from discrete samples, determined by the pycnometer method, yield values from 2.34 to 2.93 g/cm³ (Table 6).

Compressional-Wave Velocity

Compressional-wave velocity ranges between 3784 and 6316 m/s. A minimum value was determined for Core 128-794D-17R; a maximum value for Core 128-794D-13R (Table 6).

Thermal Conductivity

Thermal conductivity was routinely determined for one slab from each core. Results are shown in Table 7. Thermal conductivities varied between 1.191 and 1.665 W/m · K. The sedimentary sequence of Core 128-794D-10R (see "Igneous Rocks" section, this chapter) is generally characterized by a smaller thermal conductivity than the igneous rocks above and below that sequence.

Grain Density

Grain densities varied and range from 2.58 to 2.94 g/cm³ (Table 6). A minimum value was determined for the sedimen-

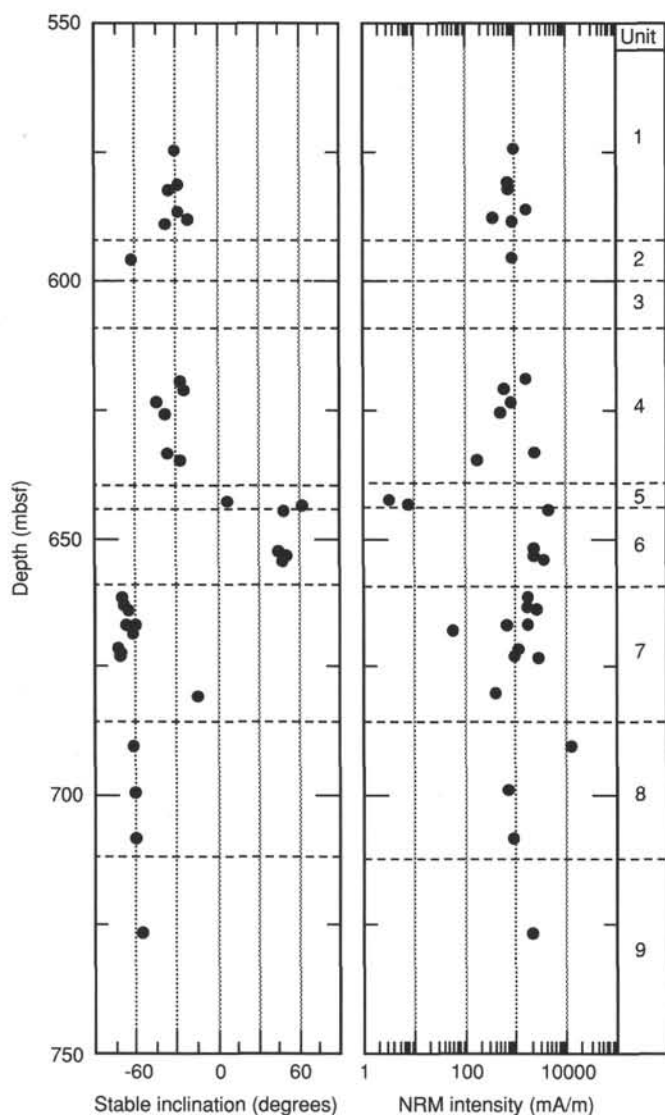


Figure 39. Plot of stable inclination and NRM intensity vs. depth for all samples from Hole 794D.

tary sequence of Core 128-794D-10R; a maximum value for Core 128-794D-12R.

Porosity and Water Content

The results of measuring porosity and water content are listed in Table 6. The sedimentary sequence of Core 128-794D-10R is generally characterized by higher values for water content and porosity than values in the igneous rocks above and below that sequence.

DOWNHOLE MEASUREMENTS

Operations

Because of the poor hole conditions encountered at Hole 794D, only one of the four logging runs scheduled at this site was completed. A seismic stratigraphy combination was run in the 173.5 m of open hole from total depth (733.5 mbsf) to the base of the casing (560 mbsf). The FMS obtained data from 596 to 560 mbsf, in the upper portion of the open hole. A summary of the sequence of events that occurred during logging operations, with individual tools listed, is presented in Table 8.

The hole problems occurred at the boundaries between the igneous sills and flows (see "Igneous Rocks" section, this chapter), where a probable mixture of sediment and altered igneous rock was sloughing and/or swelling into the borehole. Despite attempts to clear these bridges, they rapidly reformed, leading us eventually to abandon logging.

Quality of Logs

Despite the reduced logging program at Hole 794D, the data obtained were of high quality and invaluable for accurately constraining the number, position, and thickness of the sills and flows in the sequence (see "Igneous Rocks" section, this chapter). This was not possible from cores alone as overall core recovery was only about 22%. Unfortunately, we were unable to read the hole diameter for most of the logged sequence as the potentiometer on the caliper of the seismic stratigraphy tool combination broke during the first, unsuccessful attempt at logging the hole. Our second attempt with this tool produced good quality logs, as seen in Figure 43. However, the sonic velocity logs exhibited a fair amount of cycle skipping around the boundaries between the igneous units. This was caused by a probable combination of borehole washouts and the attenuation of the sonic waves by the sharp velocity contrast between the igneous units and the intervening sediments or alteration zones. Some preliminary processing has been performed for the velocity log shown in Figure 43, but this should be much improved by post-cruise processing at Lamont-Doherty Geological Observatory using the sonic waveform data.

Log Characteristics

The volcanic rocks observed in the Leg 128 cores can be divided into eight main units on the basis of the response of the NGT (see Fig. 43, solid intervals), and in combination with the resistivity log, Unit 5 can be subdivided into three subunits, with Units 7 and 8 into two subunits each (Fig. 43).

The sedimentary layers and regions of altered volcanic rock can be readily identified from the trace of the NGT because these have considerably higher total gamma-ray values (dashed intervals in Fig. 43). This increase in gamma rays is a function of the higher contents of uranium, thorium, and potassium of the sediments relative to the igneous units. In addition, the altered basaltic flows and sills were observed to contain some potassium-bearing alteration minerals, such as celadonite (see "Igneous Rocks" section, this chapter). This potassium probably derived from seawater, either by direct interaction at the top of the volcanic flows, or by later hydrothermal circulation. Therefore, part of this increase in gamma rays may result from potassium enrichment of the basaltic material, which we saw from the cores was highly altered near the boundaries of the units. Figure 44 presents the spectral component of the total gamma-ray log. This log indicates that an enrichment of potassium, uranium, and thorium occurs in the high gamma-ray sections relative to the igneous units. Both potassium and uranium can be enriched or depleted in a host rock that has undergone alteration, as potassium is soluble in seawater and uranium can be, depending on its oxidation state. However, thorium is insoluble and is not generally enriched by seawater alteration; therefore, one would expect thorium to be present in higher concentrations in sediments. Although we observed sediment in the cores only between Units 4 and 5, it is probably present between the other main unit boundaries as well.

Volcanic sand and mud were recovered from openings within the bottom portion of the Lamont-Doherty temperature tool, which was stopped by a bridge at 607 mbsf, and one can reasonably assume that the bridge consisted, at least in part,

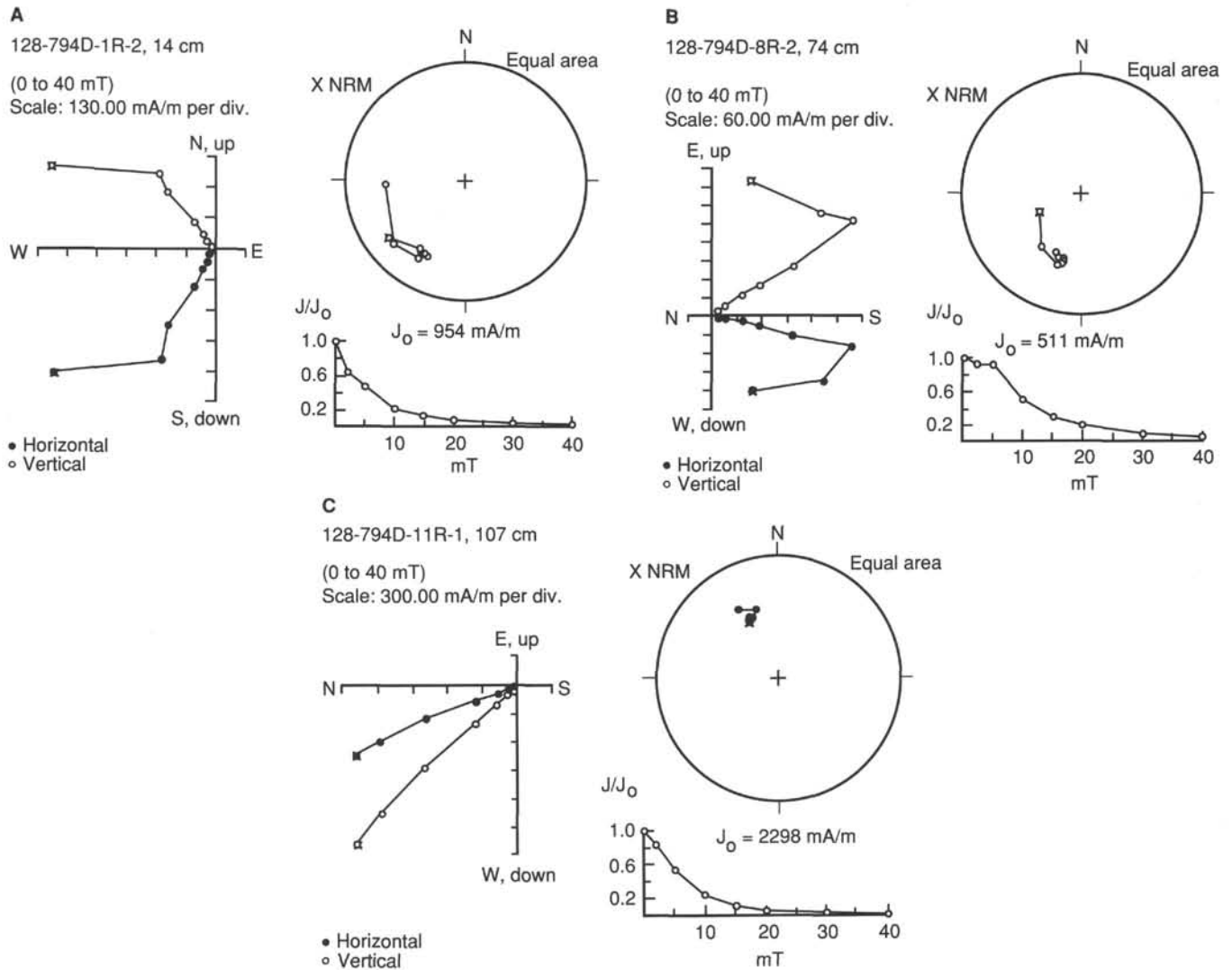


Figure 40. Examples of Zijderveld plot, equal-area projection, and plot of intensity plot of the demagnetization curves for samples from Hole 794D. **A.** Sample 128-794D-1R-2, 14 cm. **B.** Sample 128-794D-8R-2, 74 cm. **C.** Sample 128-794D-11R-1, 107 cm.

of the material brought up in the end of the tool. This volcanic clay and sand is reflected by high gamma-ray and low resistivity log values of between 607 and 609 mbsf. Sediments were observed in Core 128-794D-10R at the interval of higher gamma-ray values from 640 to 645 mbsf.

The lower resistivity readings are an indication of sedimentary clays, ash zones, and individual flow boundaries (Fig. 43). Separation of the deep resistivity (IDPH) curve from the shallow resistivity (SFLU) curve is an indication of possible fracturing or secondary porosity within the volcanic rocks; this separation occurs at 685 mbsf and between 461 and 462 mbsf. Only the medium-depth resistivity is shown in Figure 43. The magnitude of the resistivity of the igneous units gives one a general indication of competency and degree of alteration that these units underwent. The flows identified from these cores were generally more altered and exhibited a lower resistivity than the sills (See "Igneous Rocks" section, this chapter). As seen from the logs, the three units that have the highest resistivity values, Units 1, 5B, and 8, were identified as sills from the cores (Core petrologic Units 1, 7, and 9). These three units also have the highest sonic velocity, indicating a higher degree of competency over the flows. Unit 8 has by far the highest resistivity (with a maximum value of

about 400 ohm-m) as well as the highest average sonic velocity. This was reflected in the cores, as this unit was the least altered and contained fresh olivine.

The base line of the gamma-ray curve exhibits a definite shift to lower values between log-defined volcanic Units 1, 2, 3, and 4; and the four lower volcanic Units 5, 6, 7, and 8 (Fig. 43). The same relationship can be seen in the potassium curve (Fig. 44). The variation in both the total gamma-ray and potassium contents reflects a change in the chemistry within the hole, as noted in the "Igneous Rocks" section (this chapter).

The Formation Microscanner

The FMS log was obtained only in the uppermost sill from 596 to 560 mbsf. However, this short record shows a remarkable amount of detail, a short section of which is shown in Figure 45. The FMS images, which represent four orthogonal resistivity profiles of the borehole wall, exhibit numerous resistivity gradations that are interpreted as cumulate layering within the thick sill. The images also show a network of infilled veins and fractures on a centimeter-scale. There is a continuous record of the azimuth of the pads, so it will be possible to work out in detail the direction of dip of the

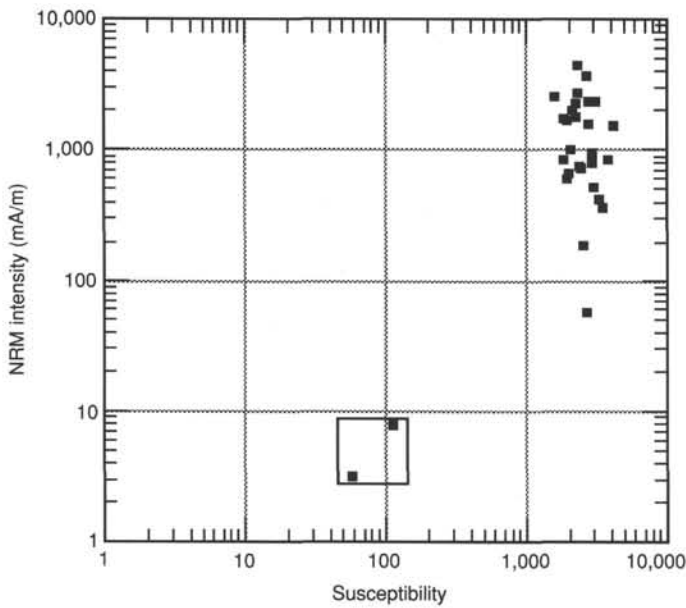


Figure 41. Relationship between NRM inclination and magnetic susceptibility for the basement rocks recovered from Hole 794D. Two samples at lower left are the sediment samples.

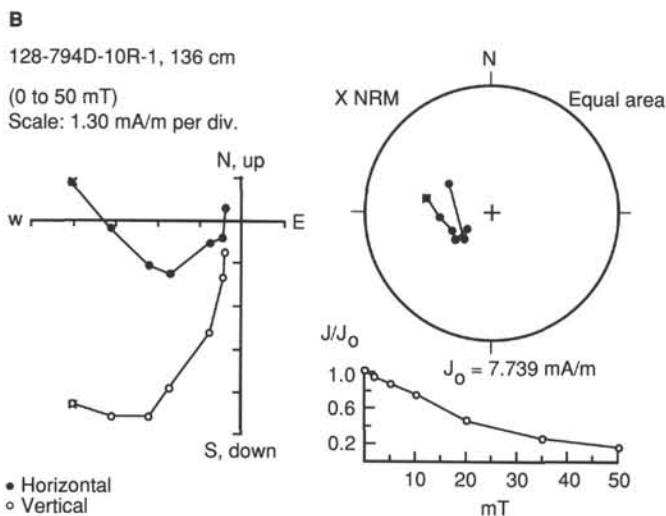
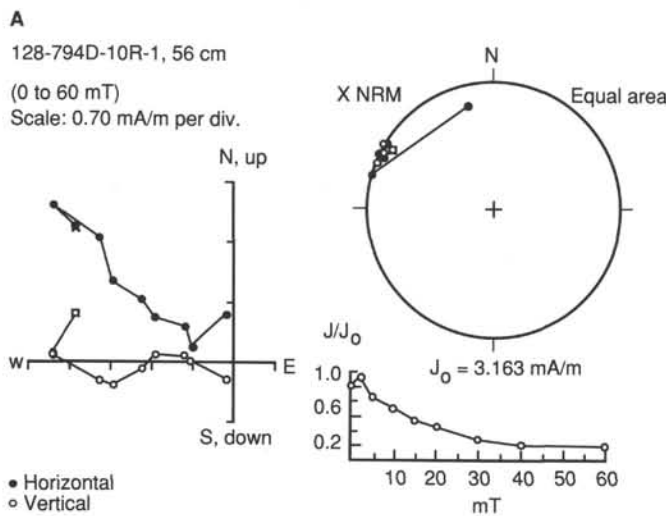


Figure 42. Comparison of demagnetization curves for the two sediment samples from Hole 794D. A. Sample 128-794D-10R-1, 56 cm. B. Sample 128-794D-10R-1, 136 cm.

Table 4. Stable inclination and NRM intensity for the lithological units observed in Hole 794D.

Igneous lithology unit	Stable inclination (degrees)	NRM intensity (mA/m)	Lithologic description
1	-30.8 ± 5.8 (6)	863 ± 400 (6)	Dolerite sill
4	-33.3 ± 7.8 (6)	991 ± 796 (6)	Dolerite sill
7	-67.2 ± 4.5 (8)	1519 ± 787 (9)	Dolerite sill
9	-56.1	2017	Dolerite sill
2	-61.8	849	Basalt flow
6	47.6 ± 2.0 (4)	3170 ± 1029 (4)	Basalt flow
8	-61.1 ± 0.9 (3)	4340 ± 6176 (3)	Basalt flow

Note: Numbers in parenthesis are the number of samples in each unit.

Table 5. GRAPE-measured density for Hole 794D.

Core, section, interval (cm)	Depth (mbsf)	Wet-bulk density (g/cm ³)
128-794D-1R-2, 21-23	574.71	2.56
2R-1, 0-22	580.60	2.58
3R-1, 61-73	586.51	2.62
4R-1, 21-23	595.61	2.30
4R-1, 29-31	595.69	2.32
7R-1, 66-81	619.66	2.45
8R-1, 42-52	623.92	2.43
9R-1, 45-61	633.45	2.45
10R-1, 67-83	642.87	2.11
11R-2, 25-39	653.07	2.49
12R-1, 64-76	661.34	2.63
13R-1, 7-23	666.07	2.77
14R-1, 66-92	671.16	2.80
17R-1, 80-91	699.40	2.70
18R-1, 38-46	708.20	2.68
19R-1, 0-16	717.10	2.71
20R-1, 15-31	726.75	2.79

Table 6. Summary of physical-properties data for Hole 794D.

Core, section, interval (cm)	Depth (mbsf)	Wet-bulk density (g/cm ³)	Grain density (g/cm ³)	Water content (%)	Porosity (%)	P-velocity (m/s)
128-794D-1R-2, 17-19	574.67	2.73	2.79	3.8	9.7	4856
2R-1, 44-46	581.04	2.67	2.75	3.5	8.7	4971
2R-2, 30-32	582.40	2.66	2.77	4.1	10.1	4437
3R-1, 67-69	586.57	2.68	2.87	4.6	11.4	4474
3R-2, 69-71	587.99	2.73	2.86	3.6	9.1	5166
3R-3, 28-30	589.03	2.70	2.84	3.7	9.3	5257
4R-1, 39-41	595.79	2.35	2.78	12.8	26.0	5380
7R-1, 37-39	619.37	2.60	2.78	26.1	41.7	4241
7R-2, 81-83	621.31	2.60	2.83	7.1	16.4	4377
8R-1, 18-20	623.68	2.60	2.81	6.6	15.4	—
8R-2, 74-76	625.75	2.58	2.82	6.9	16.1	4691
9R-1, 58-60	633.58	2.57	2.79	7.0	16.2	4174
9R-2, 46-48	634.81	2.41	2.76	11.8	24.5	4576
10R-1, 56-58	642.76	2.34	2.58	24.1	38.0	—
10R-2, 96-98	644.66	2.49	2.65	6.3	14.0	3810
11R-1, 107-109	652.47	2.53	2.74	6.0	13.9	3823
11R-2, 37-39	653.19	2.58	2.76	4.9	11.7	4062
11R-3, 27-29	654.39	2.60	2.78	4.6	11.2	4227
12R-1, 69-71	661.39	2.82	2.83	1.7	4.4	5704
12R-2, 118-120	663.38	2.80	2.88	1.7	4.6	5033
12R-3, 20-22	663.88	2.93	2.94	0.3	0.8	6037
13R-1, 74-76	666.74	2.82	2.85	1.9	5.2	4929
13R-1, 87-89	666.87	2.93	2.93	0.6	1.6	6316
13R-2, 64-66	668.14	2.64	2.82	5.8	13.8	4765
14R-1, 88-90	671.38	2.84	2.89	2.0	5.4	5986
14R-2, 135-138	673.16	2.71	2.86	4.3	10.8	4620
15R-1, 64-66	680.54	2.78	2.91	3.6	9.2	5000
16R-1, 110-112	690.40	2.62	2.81	6.0	14.2	4205
17R-1, 38-40	698.98	2.70	2.84	4.5	11.3	3784
18R-1, 16-18	708.06	2.73	2.81	3.4	8.6	4610
20R-1, 5-7	726.65	2.89	2.89	0.6	1.5	5355

Table 7. Thermal conductivities recorded at Hole 794D.

Core, section, interval (cm)	Depth (mbsf)	Thermal conductivity (W/m · K)
128-794D-1R-2, 21-23	574.71	1.659
2R-3, 9-10	583.44	1.665
3R-2, 95-96	588.25	1.465
4R-1, 21-22	595.61	1.191
7R-2, 103-104	621.53	1.237
8R-1, 40-41	623.90	1.464
9R-2, 35-36	634.70	1.533
10R-1, 67-68	642.87	1.445
11R-3, 92-93	655.04	1.549
12R-1, 45-46	661.15	1.558
13R-1, 10-11	666.10	1.439
14R-1, 92-93	671.42	1.501
17R-1, 81-82	699.41	1.340

Table 8. Summary of the sequence of operations conducted during logging of Hole 794D.

Time (UTC)	Procedure
1645 to 1915 (24 September 1989)	RIH with seismic stratigraphy combination (SDT-DITE-NGT+TLT). Log down from end of casing to 607 mbsf, where bridge encountered. Unable to pass bridge, log up to end of casing, POOH.
1915 to 0500 (25 September 1989)	Ream through bridges to base of hole, sweep hole and displace with a weighted mud (10 ppg) containing 2% KCl. POOH with pipe to 432 mbsf.
0500 to 0815	RIH with seismic stratigraphy. Logged down to TD setting down once on reforming bridge at 607 mbsf. Logged up into end of casing, POOH.
0815 to 1115	RIH with FMS combination (FMS+NGT). Sat down on bridge at 596 mbsf, unable to pass. Log up section between bridge and end of casing (twice), POOH to recondition hole.
1115 to 1515	Wash down to TD, bridges encountered at 595, 640, and 672 mbsf. Pull pipe back to 648 mbsf (just below worst bridge).
1515 to 1830	RIH for second attempt with FMS. Tool sat down on obstruction within pipe at 642 mbsf. Attempt to work tool out of pipe, apply 400 psi water pressure, no success in getting out of pipe. POOH, out of time, logging aborted.

Note: Table includes a listing of the individual tools run for each logging string. RIH = run in to hole; DITE = phaser induction tool; SDT = digital sonic tool; NGT = Natural gamma spectroscopy tool; END OF CASING = 560 mbsf; TLT = temperature logging tool (Lamont-Doherty); FMS = formation microscanner; POOH = pull out of hole.

layering, fractures, and veins within the sill. From the fracture directions, one should be able to elucidate the stress regime of the hole.

DOWNHOLE SEISMOMETER EXPERIMENT

Introduction

A broad-band digital downhole seismometer was installed at Hole 794D in the northern Yamato Basin to aid in the study of laterally heterogeneous crust and upper mantle in the Japan subduction complex. Studies of the heterogeneous interior of Earth or of the complex fracturing dynamics of earthquakes require a seismic network that covers the whole surface of the planet. The general objective for installing a downhole seismometer is to establish a permanent seismic station in the

oceans that cover 70% of Earth's surface. Major technical difficulties exist for accomplishing such a task, namely, how to supply power and how to retrieve the data (e.g., COSOD II, 1987). During the years of the Deep Sea Drilling Project, however, scientists attempted to emplace ocean borehole seismometers, utilizing drilled holes during Legs 65, 67, 78A, 78B, 88, and 91 (Lewis, Robinson, et al., 1983; Aubouin, von Huene, et al., 1982; Biju-Duval, Moore, et al., 1984; Hyndman, Salisbury, et al., 1984; Duennebie, Stephen, et al., 1987; Menard, Natland, et al., 1987). Since the deployments of 1983, there have been no further attempts until now.

In the 1980s, digital and feedback sensor technology made it possible for scientists to establish a digital seismic network having a wide frequency band and large dynamic range on land. This network has yielded important new images of Earth's interior and its seismic activity (e.g., Romanowicz and Dziewonski, 1986). We think that our attempt to install a downhole seismometer during Leg 128 is the first application of such new technology at an ocean-floor station. In the following sections, we describe the downhole seismometer experiment that took place during Leg 128 at Site 794. The first part of the experiment was to install the borehole instrument and to perform a controlled-source, seismic-refraction profiling experiment with the support of the *Tansei-maru* of the University of Tokyo Ocean Research Institute. Then, recording, power supply, and retrieval packages were deployed on the seafloor for off-line, long-term seismic observation in coordination with another supporting vessel, *Kaiko-maru-5*, chartered by the University of Tokyo Ocean Research Institute.

System Design

The downhole seismometer system is composed of two main units: (1) the sensor package, emplaced in the drilled hole and (2) the recorder unit, which can be deployed on the seafloor should off-line data acquisition be employed, or maintained aboard a vessel in cases where scientists wish real-time observation. The two units are linked by a seven-conductor logging cable normally used for downhole logging at ODP. The layout of this system is similar to ocean sub-bottom seismometer (OSS) systems built at the University of Hawaii (Duennebie, Stephen, et al., 1987). Although this was the first deployment by the *JOIDES Resolution*, the installation procedure was intended to be nearly the same as that previously performed by the *Glomar Challenger* (Table 8).

The sensor package includes three orthogonal, feedback-type accelerometers having leveling mechanisms and a broad-band data transmission system that converts the analog signal to 16-bit digital data with high and low gains for each component. The six-channel digital data are transferred uphole at a rate of 80 Hz sampling/channel (19,200 bps) via the logging cable. The high-gain channel has a resolution of about 10^{-8} m/s² between 100 s and 30 Hz, while the low-gain channel is shifted by about 2 bits between DC and 30 Hz (Table 9). Commands can be sent downhole to center the masses and to level the bases of horizontal components within the pressure vessel. The pressure vessel is 3 m long and 98 mm in diameter to allow it to run through the drill pipe. It is equipped with a pad that extends outwardly to clamp in the open, 10-in.-diameter hole.

Data and power links were made through all seven conductors and the armor of the logging cable (Table 10). The assignment of each conductor to power and signal was chosen to minimize the electrical resistance for the power lines. A final change in the power supply scheme was made on board the ship. Originally, a DC-to-DC converter was placed to generate the positive and negative voltages required for run-

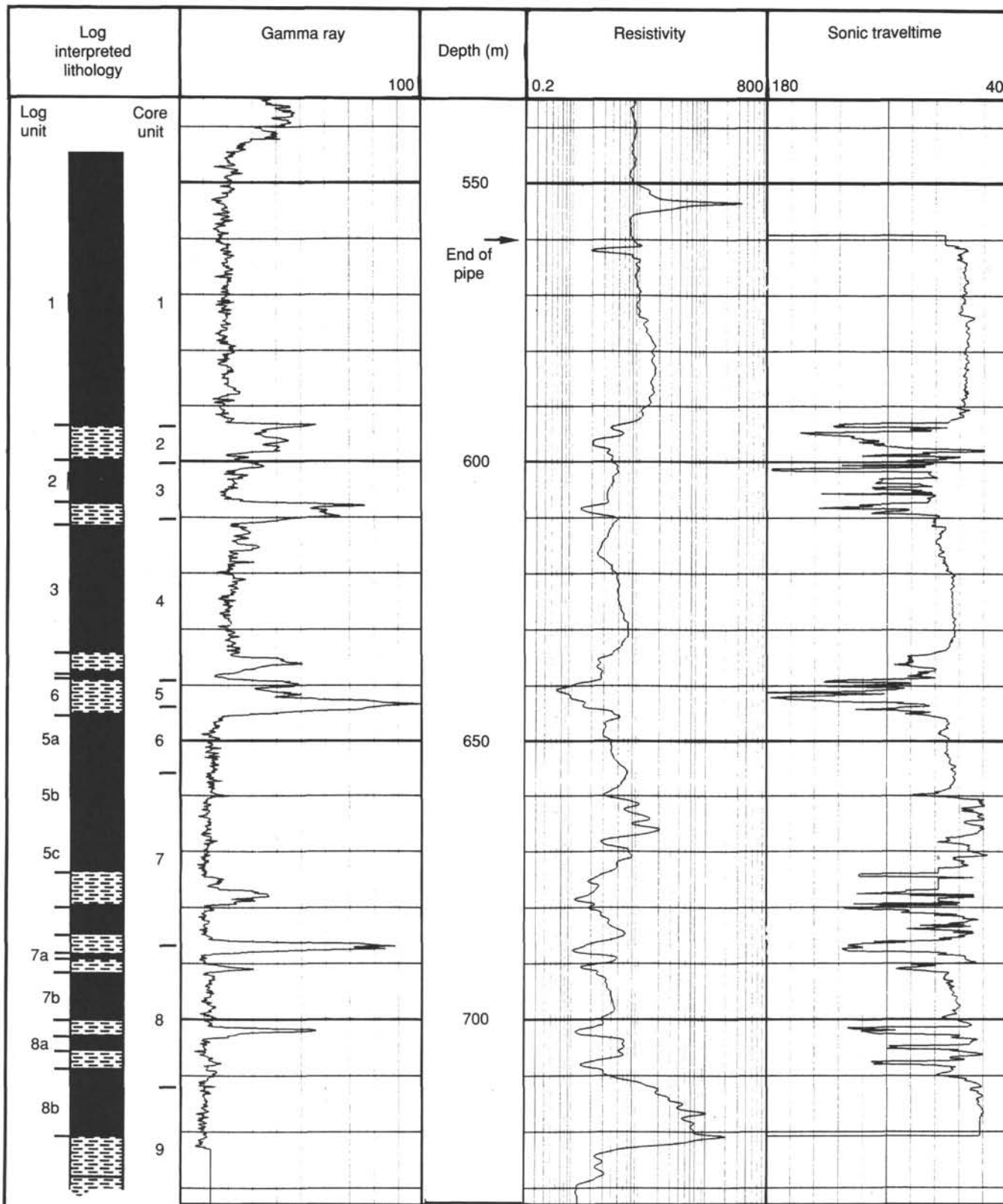


Figure 43. Selected log traces for Hole 794D. Column 1, interpreted lithology from the logs: eight igneous units (dark shading), separated by sediment/altered volcanic material (light shading). Column 2, lithologic units based on core observations extrapolated with logging data (see "Igneous Rocks" section, this chapter), are included for comparison; total gamma rays (0–100 API units); resistivity (phasor induction medium, 0.2–800 ohm-m); sonic traveltime (180–40 μ s).

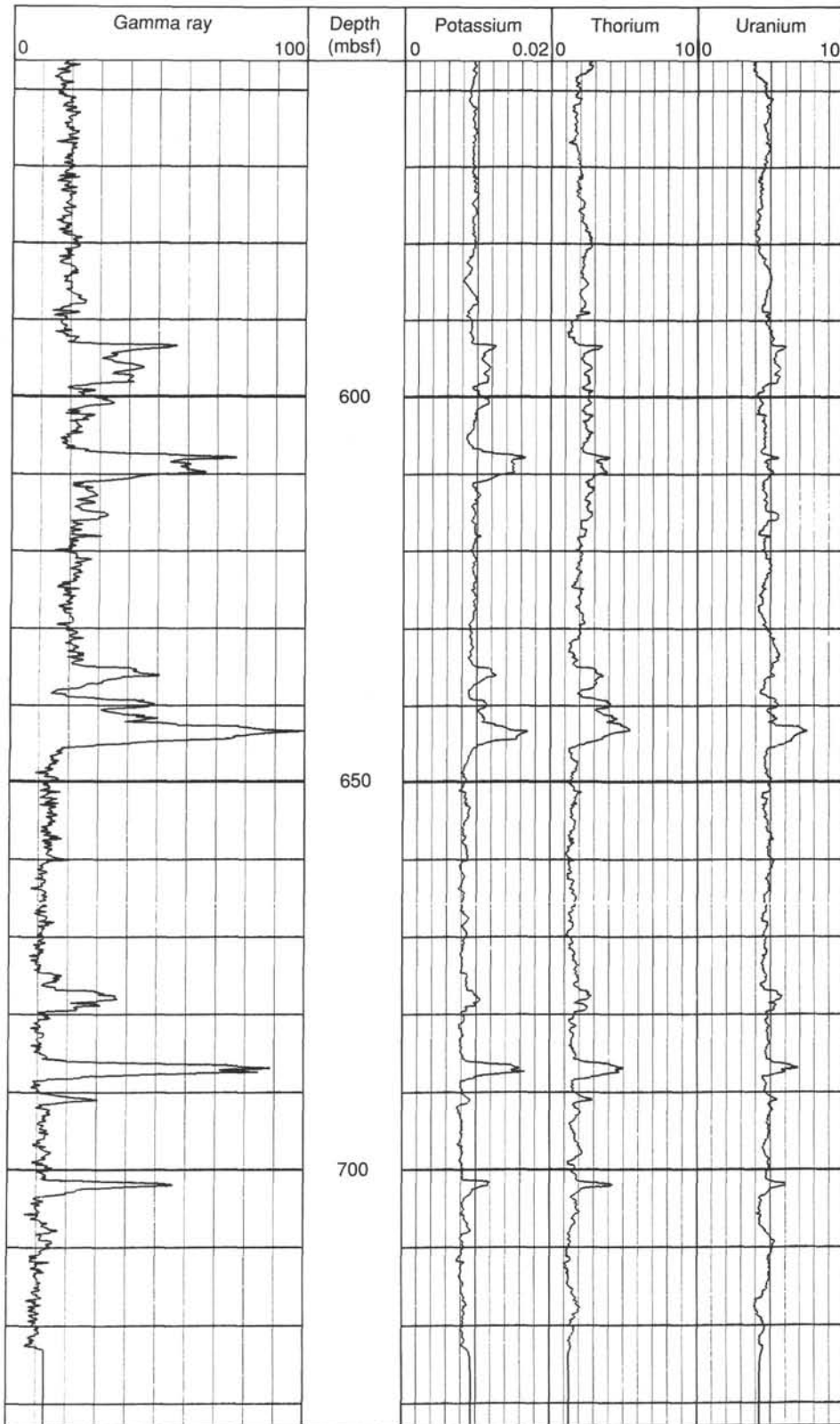


Figure 44. Selected NGT log traces for Hole 794D. These data should be considered semiquantitative; post-cruise processing will correct these data for measuring and calibrating errors. Total gamma ray (API units), potassium (wt%), thorium (ppm) and uranium (ppm).

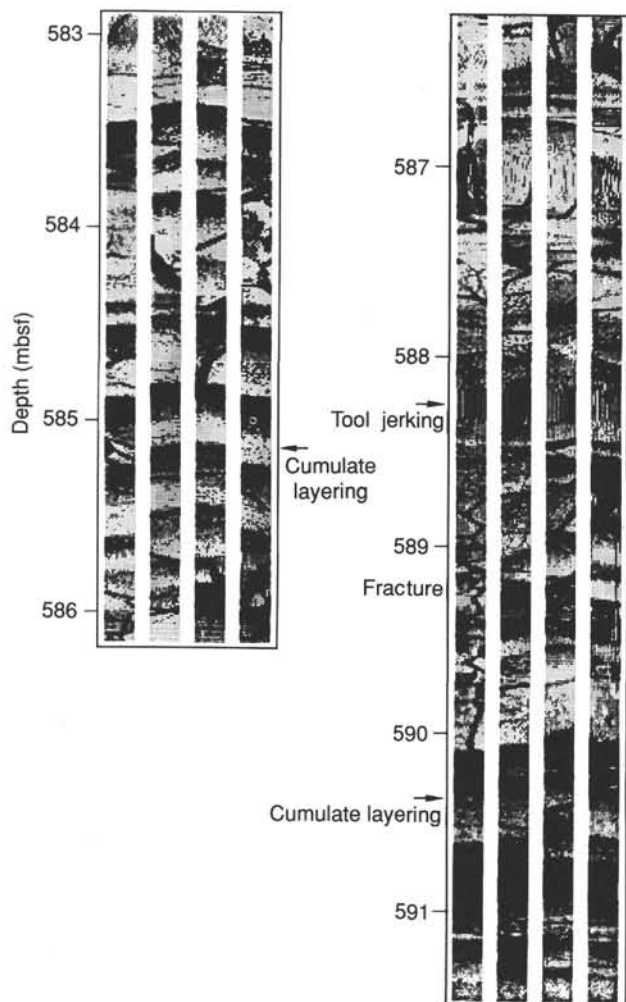


Figure 45. Preliminary microresistivity images from the formation microscanner (FMS) of an 8 m section of Hole 794D. The four tracks represent the resistivity profile of the borehole wall measured by each of the four orthogonal pads of the FMS. Depths are shown in meters below sea floor.

Table 9. Specifications of the downhole seismometer employed during Leg 128.

Pressure vessel with extending pad: Kaihatsu Kogyo Co.
Dimension: 3 m (length) × 98 mm (diameter)
Pad: Extends to 272 mm diameter, driven by a motor
Sensor: Guralp DT008A slimline CMG-3
Three-axis feed-back accelerometers
Sensitivity: Low-gain 2,700 V/m/s ² (DC-30 Hz)
High-gain 16,000 V/m/s ² (0.01-30 Hz)
Resolution: Low-gain 5.65 × 10 ⁻⁸ m/s ² (1 bit)
High-gain: 9.5 × 10 ⁻⁹ m/s ² (1 bit)
Dynamic range: 16-bit each gain
Sensor and feedback electronics stack:
Dimension: 525 mm (length) × 75 mm (diameter)
Power supply: +12 V, -12 V
Leveling control:
Vertical: Mass centering by command-driven motor
Horizontal: Mass centering by command-driven motor and sensor base leveling (accommodates 5° of tilt)
Broad-band data transmission system:
Dimension: 500 mm (length) × 75 mm (diameter)
Power supply: +15 V, -15 V (operates at ±12 V and ±5 V)
A/D converter: 16-bit, 80 Hz sampling/channel
Data transmission: DPSK (differential phase shift key) modulation
Command transmission: FSK (frequency shift key) modulation

Table 10. Assignment of cable conductors.

#1:	GND
#2:	Power (48 V)
#3:	Command (RXD+)
#4:	Data (TXD+)
#5:	Power (-48 V)
#6:	Data/command common
#7:	Pad motor
Armor:	GND

Note: Center conductor is #7.
Conductor #1 through #6 runs clockwise looking downhole.

ning the downhole instrument. Instead of sending only positive voltage, both positive and negative voltages were sent downhole. We thought this was necessary to send and regulate the power downhole to operate commands, and was made possible by reducing the data lines from four to three.

The seafloor recorder package consists of an event-driven, 60-Mbyte, intelligent recorder and a battery pack, to which the logging cable from the downhole instrument is connected (Table 11). With the present design of limited-capacity data storage, recording is mostly performed at much lower rates after applying anti-aliasing, low-pass filters. Using the present system, the rate of power consumption permits only a limited time (two months) for long-term observation. This system has been designed so that the batteries will not be totally discharged. The seafloor unit is attached to a 6000-m buoyant rope, an acoustic transponder, glass spheres, and a weight (Table 11). Upon recovery, an acoustic command will be sent from the surface to release the weight. If that should fail, the buoyant rope will be fished.

The digital data-recording scheme has two modes. One is an event-driven scheme and the other is a pre-set time-window data recording. The former mode has higher priority. An event is detected by monitoring the ratios of the short-term average (STA) and long-term average (LTA) of signals sampled at 20 Hz (SP) and 1 Hz (LP) (Table 11). The STA/LTA threshold level is set at 4; however, if no event occurs over 10 days, then the STA/LTA will be set at 2. If either ratio is over

Table 11. Specifications of the seafloor recording/recovery unit deployed at Site 794.

Dimension: 1274 mm (length) × 270 mm (diameter)
Recorder: Sea data high-capacity recorder HCR-660K (60 Mbytes)
Media: Cartridge tape
Power supply: 20AH battery pack
Data recording controller: Akashi Co.
Second-order digital low-pass filters: 10 Hz, 0.5 Hz, 8.33 mHz, 138.9 μHz
Recording scheme:
Event detection: short period (SP) 20 samples/s × 6 chs × 40 min long
period (LP) 1 sample/s × 6 channels × 2 hr
STA = average of 10 samples; LTA = average of 1000 samples
STA/LTA > 4; if no event over 10 days, then STA/LTA > 2
Time window: Low-gain channels-1 sample/hr × 180 days
Low-gain channels-1 sample/min × 45 days
All channels 80 sample/s: 1 min length × 10 times
Modem: Guralp Systems
Main power supply: Deep Sea Power & Light Inc.
Frame: 1.49 m × 1.38 m × 0.94 m
Battery: Sea batteries 24 V-38AH (20)
Connection: +48 V and -48 V
Rope system:
Nylon rope: 24 mm (diameter) × 500 m (length)
Polypropylene rope: 24 mm × 3500 m
Polypropylene rope: 16 mm × 2000 m
Acoustic transponder: Kaiyo Denshi Co.

the threshold, recording will begin. Once started, no detection or change of mode will be made until recording is finished. Time-window data recording is intended to provide background noise and activity information. Data recording at three sampling rates has been programmed to begin at three different time spans (Table 11).

Real-time recording was performed on board the *JOIDES Resolution* in the Underway Geophysics laboratory (Table 12). A modem was required to demodulate the incoming data and to modulate the downhole commands. An RS232 serial interface connected with IBM-PC/AT compatible computers was used to receive and record all the data and to send commands. Two recordings were performed simultaneously: one onto an 80-Mbyte hard disk of a COMPAQ-386 computer, and the other to a magneto-optical disk (600 Mbyte) interfaced to a Toshiba J-3100GT laptop computer. Because the rate of data transmission is high and there is no control over the line, considerable efforts were made in software development to capture continuously and to store the data on the hard disk with time stamping. Time was calibrated vs. the Japan Standard Time (JJY) radio signal.

Installation

We had planned to emplace the seismometer in Hole 794C, which was drilled to basement and cased through the sediments during Leg 127. This would allow us to stabilize the hole for about two months before installation. However, a BHA was left in the hole during Leg 127 because of operational difficulties. The Leg 128 schedule was lengthened by 10 days to allow for fishing of the BHA, but our attempt to fish the BHA failed, and a new hole was drilled and cased. Because the geophysical downhole experiments required two supporting vessels that were on tight schedules, the pre-scheduled experiment dates had to remain unchanged despite the 10-day extension of the cruise.

Hole 794D (water depth, 2807 mbsf) was drilled to 666 mbsf from 4 September to 13 September, and the sedimentary section was cased through 560 mbsf. The hole was deepened to 733.5 mbsf from 22 September to 24 September (See "Operations" section, this chapter). Logging runs were attempted at this time; however, only one complete run of the seismic stratigraphy tool and a partial run of the FMS tool could be conducted because of "bridge" constriction in the hole (see "Downhole Measurements" section, this chapter). Logging information, together with that obtained from sampled igneous rocks (see "Igneous Rocks" section, this chapter), was used to determine the depth at which the seismometer would be installed. The igneous-rock section below the casing is about 174 m long. Within this section, intervals having consistently higher resistivity and sonic velocity values for appreciable lengths were either at the top or at the bottom, corresponding to Units 1 or 8, respectively (see "Igneous Rocks" section, this chapter). We decided to

Table 12. Real-time recording set-up used at Site 794.

Modem: Guralp Systems
Reference time: Japan Standard Time (JJY radio signal)
Time code generator: accuracy $<10^{-6}$
Recording System A:
Processor: COMPAQ 386-40
Storage: 80-Mbyte hard disk
IRWIN 40-Mbyte minicartridge tape back-up system
Recording System B:
Processor: TOSHIBA J-3100 GT
Storage: SONY magneto/optical disk (600-Mbyte)

try to place the seismometer in the bottom part of the hole, from 710 to 720 mbsf.

The drill pipe was lowered to near-bottom so that the instrument would not encounter obstructions. The same cable used for logging was re-headed and connected to the downhole seismometer. After testing the instrument in the Downhole laboratory and on the rig floor, we lowered it to the pre-determined depth of 718 mbsf and clamped it in the hole by extending its pad. Incoming data were saturated by noise and, hence, it was difficult to judge the performance of the instrument. Because the leveling commands did not seem to function properly, we decided to re-clamp the instrument. The pad was retracted, and the instrument was pulled up 3 m. The drill pipe was raised 8 m to make sure that the instrument was out of the pipe.

After re-clamping, the logging cable was slackened, and the instrument was tested for 1 hr. As the mass on each sensor was ranging between positive and negative extremes, we decided to position the instrument in its final location at 714.5 mbsf. The pad was not retracted because the pipe-stripping procedure would not, in principle, pull the cable. To accommodate for the motion of the ship's heave, the cable was slackened, and the pipe-stripping procedure proceeded smoothly after the cable was cut at the rig floor. Torpedo splicing was completed, and real-time recording began in the Underway Geophysics laboratory. Two stands of drill-pipe were used to protect the cable as it went through the moon pool while the *JOIDES Resolution* moved away from the hole. The *JOIDES Resolution* was offset by 1536 m in a 180° direction while paying out 1353 m of logging cable. The offset direction was determined, taking into account the OBS array location and sea currents. At this time, *JOIDES Resolution* was ready for the real-time, controlled-source experiments to begin.

Real-Time Experiment

Our objectives for conducting a controlled-source seismic experiment were (1) to obtain a detailed crustal structure of the northern Yamato Basin, and (2) to calibrate the downhole seismometer. Ample seismic reflection studies have been conducted in the Japan Sea (e.g., Honza, 1979; see "Background and Scientific Objectives" section, this chapter), but detailed information about deeper structures and seismic-wave speeds are generally absent, except for the array controlled-source seismic experiment conducted in the southwestern part of the basin in 1985 (Hirata et al., 1987). Because the instrument is not oriented, air-gun shooting will provide data about the orientation of the horizontal components. In addition, the waveforms between the records from OBSs and the downhole seismometer will be compared.

Table 13 lists the free-falling, pop-up type of OBSs that were deployed by the *Tansei-maru* of the University of Tokyo Ocean Research Institute. One OBS (from Hokkaido University) records 9 hr of digital data and the others (from Chiba University and the University of Tokyo) about two weeks of analog data. Figure 46 shows the air-gun shooting profiles for this experiment, which consisted of two circles and two cross lines. The OBSs were configured to form an array with a closely spaced subarray (Fig. 47).

Air guns were shot every 60 s at 100 kg/m² by either two 9-L or a single 17-L gun(s) for about 48 hr (Table 14). During that time, the sensors were operated in an 11-min, auto-centering mode. As no provision was made for monitoring the records while the computers were running at their capacity, the masses were automatically re-centered every 11 min. A

Table 13. Ocean-bottom seismographs deployed during the Leg 128 real-time experiment.

OBS ID	Latitude N	Longitude E	Comment
JRT-1	40°17.9000	138°28.5567	Analog
JRT-2	40°12.9000	138°17.2516	Analog
JRT-3	40°12.1500	138°15.5558	Analog
JRT-4	40°11.4000	138°13.8600	Analog
JRT-4	40°11.4000	138°13.8600	Digital
JRT-5	40°04.9000	137°59.1633	Analog
JRT-6	40°12.6990	138°12.8809	Analog
JRT-7	40°13.9981	138°11.9019	Analog
JRT-8	40°22.6583	138°05.3749	Analog

storm hit the area during the experiment, which allowed us to monitor recordings during both calm and rough seas (Fig. 48).

Real-time recording ended when the logging cable was cut at the rig floor at a length of 4962 m. This was done after slacking 49 m of cable at the offset position, clamped at the rig floor by a "T-bar," which left 19 m of cable with free tension.

Deployment of the Seafloor Package

The second phase of the experiment was aimed to initiate long-term seismic observation by deploying a complete system for off-line recording on the seafloor. These data will be recovered at a later time by another vessel.

This operation was delayed because of the late arrival of the *Kaiko-maru-5*, which had encountered bad weather and engine trouble. The vessel was to deploy the seafloor recording/retrieval unit after receiving the end of the logging cable from the *JOIDES Resolution* and to act as the "shooting vessel" during the electrical resistivity experiment (See "Electrical Resistivity Experiment" section, this chapter).

After re-heading the logging cable, we passed the cable through the moon pool to the starboard side of the *JOIDES Resolution*, where it was held by a crane to enable the *Kaiko-maru-5* to retrieve it. We took great care when passing the cable because the tension had to be transferred without losing the cable. We had originally planned for the *Kaiko-maru-5* to tie up to the *JOIDES Resolution* to receive a sufficient length of cable (about 60 m) for maintaining the connection without tension. This could not be accomplished because of the conditions of the sea and because of problems with holding the cable at the side of the ship's hull.

After successfully transferring the cable, the instrument was tested on the *Kaiko-maru-5*. The first test was conducted using the same set-up as that at the *JOIDES Resolution* Underway Geophysics laboratory, with the Toshiba J-3100GT system. Then, the cable head was connected to the seafloor recording package. The same modem boards used in our real-time experiment were inserted in the package. The instrument was tested again. After confirming that at least two sensors were operating normally, we initialized the recording cartridge tape (60 Mbyte), started the clock, set the event-trigger parameters (STA/LTA = 4), and began the recording.

The recorder package with batteries was placed into the water, followed by the rope system. The tension of the rope decreased when 2500 m of rope was paid out, at which time the recording unit probably reached the seafloor. A total of 6000 m of rope was paid out, and finally the retrieval system was placed into the water. The transponder on the retrieval unit was interrogated every 5 min until it reached the seafloor and had been located from the ship.

The downhole seismometer experiment during Leg 128 was completed at 0257UTC on 30 September, as summarized in Table 15. The final layout of the seafloor unit is shown in Figure 49.

Summary

A downhole seismometer was deployed in Hole 794D at a depth of 714.5 mbsf (3532.5 mbsl). This seismometer is equipped with a three-axis, feed-back type accelerometer having a large dynamic range and broad frequency band. A controlled-source seismic experiment was conducted while real-time recording of data was transmitted digitally over a logging cable to *JOIDES Resolution*. One horizontal-component was malfunctioning and could not be fixed during this leg. Two other components seemed to produce excellent data, as indicated by the examples presented in Figures 50 and 51. The data set will be used to study crustal structure and signal and noise characteristics over a previously unavailable, large seismic observation "window." Results, together with a detailed description of the system, will be discussed in the *Scientific Results* volume of Leg 128. After the real-time experiment, we deployed the seafloor recording/retrieval unit to initiate long-term digital recording of seismic events and background noise.

ELECTRICAL RESISTIVITY EXPERIMENT

Introduction

Electrical resistivity structure under the seafloor has been observed by various techniques. Resistivity is a useful tool for obtaining information about water content and the distribution of water at shallow depths, as well as for inferring temperature and the distribution of melts at depth in the Earth's crust and upper mantle. During DSDP and ODP cruises, scientists conducted Schlumberger logging and large-scale resistivity experiments in drill holes (Francis, 1982; Von Herzen et al., 1983; Becker, 1985). These techniques determined the resistivity structure through the hole with a depth range of about 1 km and a resolution limit of several centimeters. Natural electromagnetic disturbances also have been measured at the seafloor and have been used to determine resistivity structure to about 300 km deep (Cox et al., 1970; Filloux, 1981; Yukutake et al., 1983). Although this technique allows for deep measurements, its resolution limit is larger than 10 km because of the shielding effect of seawater on the higher frequencies of the natural disturbances. Hence, information about shallow structure is required for interpretation. To link the two types of measurements, several methods that use controlled current sources have been invented and tested (Cox et al., 1980; Edwards et al., 1981; Nobes et al., 1986). During Leg 128, a new electrical resistivity experiment was conducted using Hole 794E as a sensor.

Experiment Methods

The basic elements of this two-ship experiment are illustrated in Figure 52. A signal was generated by the *Kaiko-maru-5* and measurements were performed on board the *JOIDES Resolution*. The signal source for the controlled-source method is a vertical-current dipole that extends from the sea surface to the seafloor. Current electrodes made of stainless steel are attached at the end of two cables, one of which is lowered to the seafloor and the other of which is deployed at a specified shallow depth. The signal voltage applied between these two electrodes transmits a current signal through the water column. The transmitter consists of a DC power source and a switch box; both cables are connected to the output ports of the switch box. For the Site 794 experiment, the cable was 3500 m long and had a resistance of 4.2 ohms, including the surface resistances at the two electrodes. Hence, a constant current of 20 A could be safely

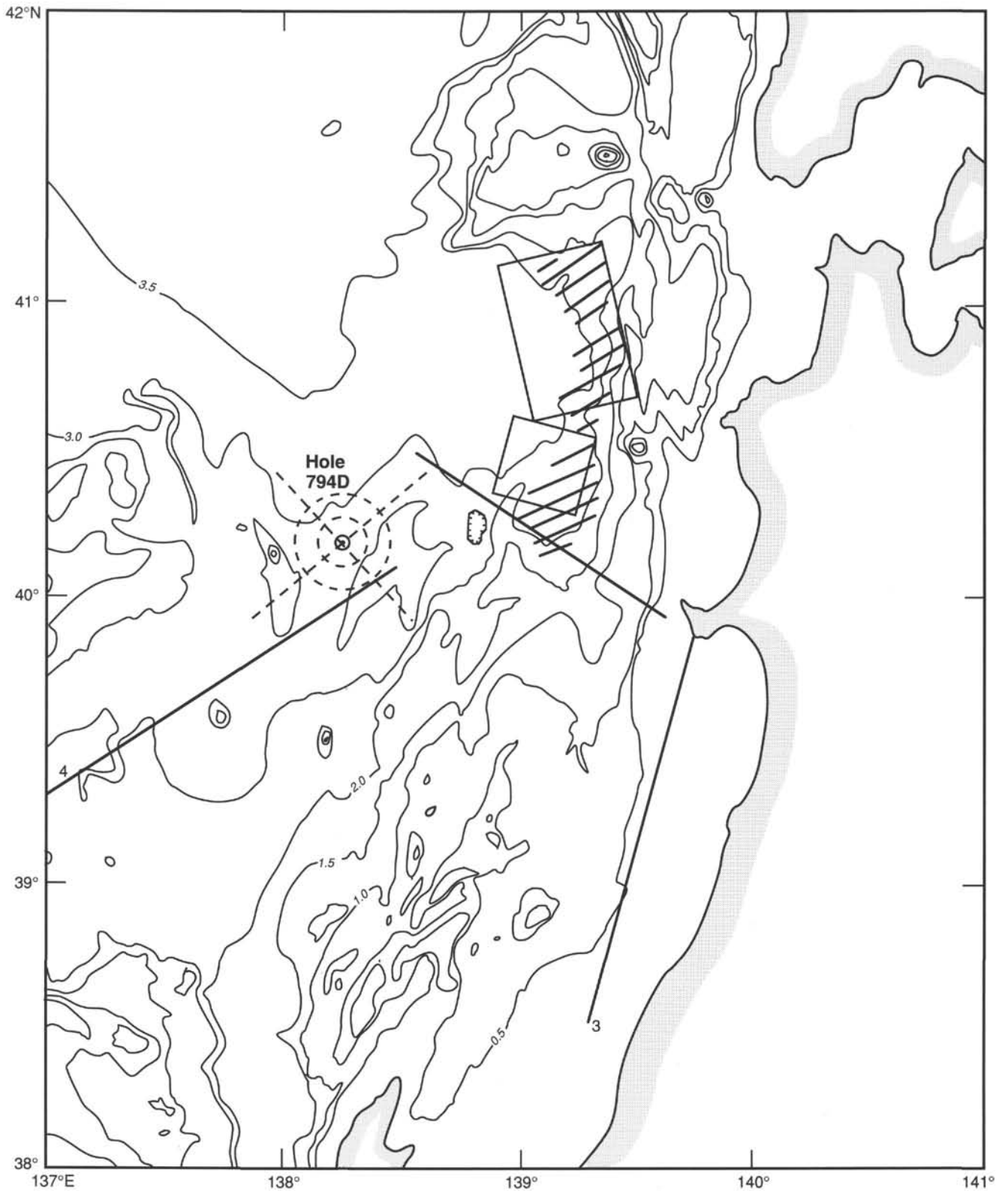


Figure 46. General map of the area surrounding Hole 794D. Solid lines are refraction profiles (Murauchi, 1966; Yoshii and Asano, 1972). Two rectangles are surface projections of faults ruptured during the 1983 Japan Sea earthquake, as inferred from teleseismic observations (Shimazaki and Mori, 1983). Aftershocks have been occurring in the hatched area. Dashed lines are the air-gun profiles shot during the real-time experiment by *Tansei-maru* of Ocean Research Institute, University of Tokyo.

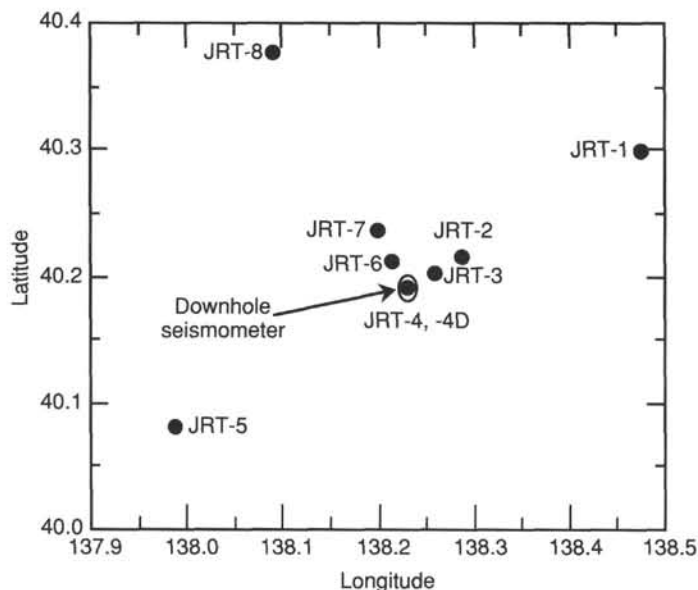


Figure 47. Locations of OBS's deployed during the controlled source seismic experiment. All OBS's were recovered after the experiment.

Table 14. Air-gun shooting sequence used at Site 794.

Profile	Date (Sept. 1989)	Time (UTC)	Comments
Inner circle	26	22:32	Start in clockwise direction
	27	05:35	End after 1/4 overlap
Outer circle	27	06:13	Start in CCW direction
	27	~13:00	<i>Tansei-maru</i> engine trouble
	27	~14:00	Air-gun malfunction
	27	15:15	Resume shooting
	27	18:45	End
Line 1	27	17:00	Start
	28	02:45	Pass <i>JOIDES Resolution</i>
Line 2	28	06:30	End at northwest end
	28	14:00	Start
	28	17:40	Pass <i>JOIDES Resolution</i>
	28	22:00	End

transmitted by a power supply having a maximum DC voltage of 100 V.

The variation in time of the current signal is shown at the bottom right in Figure 52. Positive and negative constant currents having a duration of 1 s were applied alternately. Most of the current flows through seawater, but part of it leaks into the crust and eventually returns to another electrode. The current flow is a function of the electrical resistivity contrast between the seawater and the underlying crust. Hence, observations of the electric current reveal the electrical resistivity structure beneath the seafloor. The maximum depth of the current flow is proportional to the distance between the current source and the receiver. Therefore, observations of signals at different distances can be used to obtain the vertical distribution of the electrical resistivity.

Because the current itself cannot be observed directly, magnetic or electric fields induced by this current are observed in the actual experiments. Chave and Cox (1982) derived exact closed-form expressions for the electromagnetic induction fields produced by vertical and horizontal current sources in the conducting ocean overlying a one-dimensional layered earth. In our case, because of the axial symmetry of the dipole source, only the azimuthal component of the magnetic field and the vertical and radial components of the

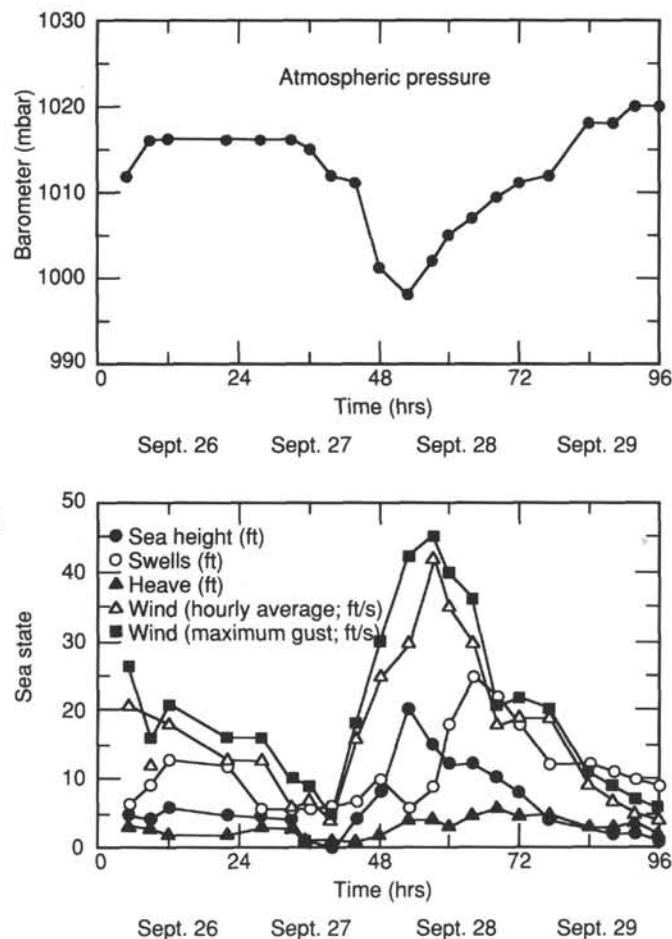


Figure 48. Barometer readings and sea state during real-time experiment from ship log. Upper figure shows barometer readings. Lower figure shows heights of seas and swells, heave motion, hourly average and maximum of wind speed.

Table 15. Summary of operations for installing downhole seismometer at Site 794.

Date (Sept. 1989)	Time (UTC)	Operation
24	14:45	<i>Tansei-maru</i> starts OBS deployment
26	00:50	Start re-heading of logging cable
	02:00	Test instrument through logging cable
	02:21	Start descent through drill pipes
	03:46	Stop winch at 3536 m (11,600 ft)
	04:26	Clamped at 3533 m (11,590 ft)
	04:45	Begin rig move in DP mode
	05:05	All components responding to commands
	05:45	Cut cable at rig floor. Start stripping drill pipe
	16:50	Start splicing cable
	18:40	Test instrument after splicing
	21:30	<i>Tansei-maru</i> ready to start real-time experiment
	22:18	<i>JOIDES Resolution</i> shift 1.5 km south from Hole 794D
	22:32	Start controlled-source seismic experiment
28	22:00	End controlled-source seismic experiment
29	06:02	End continuous seismic observation. Cut cable
	07:00	Attach cable head for connection to seafloor recording unit
	11:45	Cable hung by crane on starboard side
	14:00	Complete passing cable
	18:30	Test the recorder package on <i>Kaiko-maru-5</i>
	22:00	Start deployment by <i>Kaiko-maru-5</i>
30	02:57	End of operation

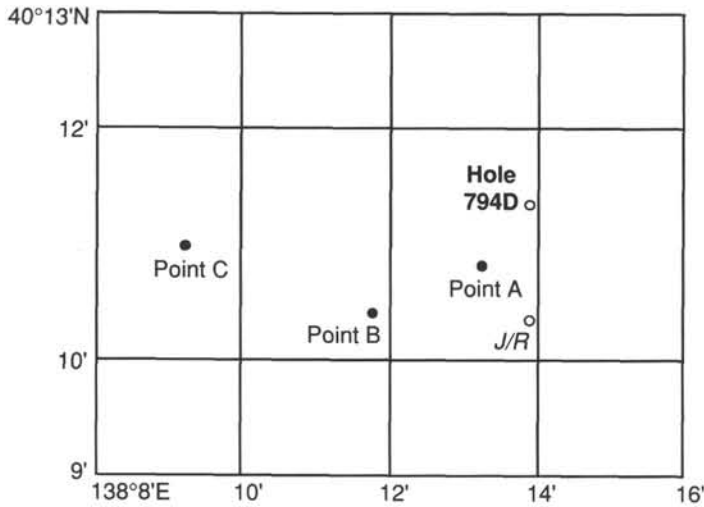


Figure 49. Layout of the downhole seismometer system. Downhole seismometer is at 714.5 mbsf in Hole 794D. *Kaiko-manu-5* deployed recorder unit at Point A (9/29 2152UTC), was located at Point B when recorder unit reached bottom (2251UTC), and deployed acoustic transponder after paying out 6000 m of rope at Point C (9/30 0008UTC).

electric fields exist. As shown in Figure 52, our experiment measured the vertical electric field in the sediment layer.

The sensor for our experiment consists of a seven-wire insulated cable with silver and silver chloride electrodes. A 300-m-long cable was connected to the bottom of the logging cable. Its position in Hole 794E is shown in Figure 53. Five electrodes are attached to the cable at 10, 40, 150, 260, 290 m from the top of the cable. These electrodes are numbered 1 through 5 from top to bottom. The bottom of the drill pipe was originally 74.7 mbsf, which was about 15 m above the uppermost electrode. During the initial test, we observed that the uppermost electrode had a noise level of about 1 mV and that the noise levels of the other electrodes decreased systematically with their distance from the drill pipe. Therefore, throughout the experiment, the electric field was measured between two pairs of electrodes (Channel 1: electrodes 3 and 5, Channel 2: electrodes 2 and 4). The distances between the electrode pairs are 140 and 220 m for Channels 1 and 2, respectively. The observed signal has been schematically illustrated in the bottom left of Figure 52. Because of the shielding effect of seawater on higher-frequency signals, the variation in time of the signal has been filtered. The amplitude of the signal yields a vertical gradient of the electric potential through the hole and, hence, the electric current density.

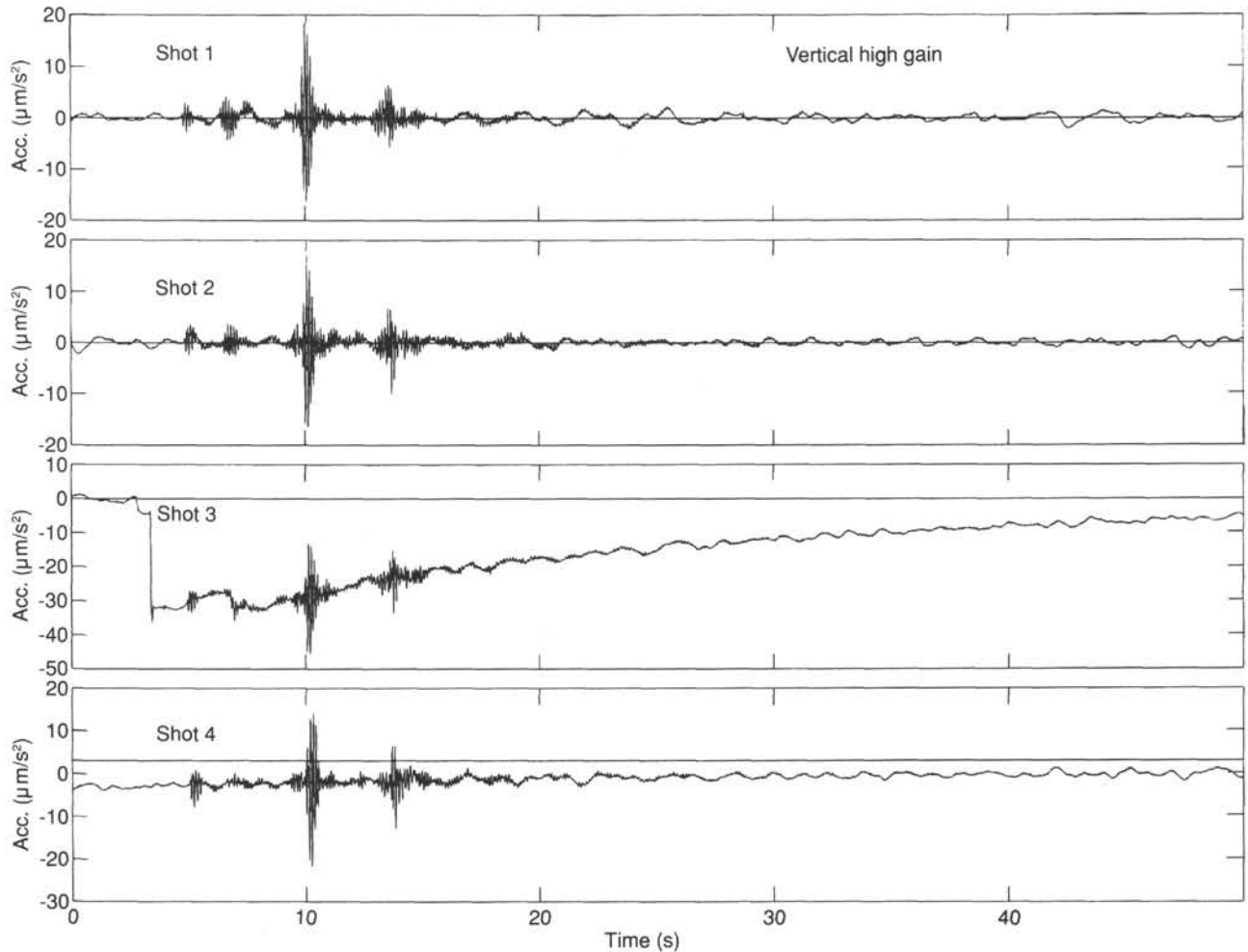


Figure 50. An example of four air-gun shots from vertical high gain channel record between 2303-2308-UTC on September 26 at a distance of 9 km offset. The DC shift before air-gun shot 3 is due to mass centering.

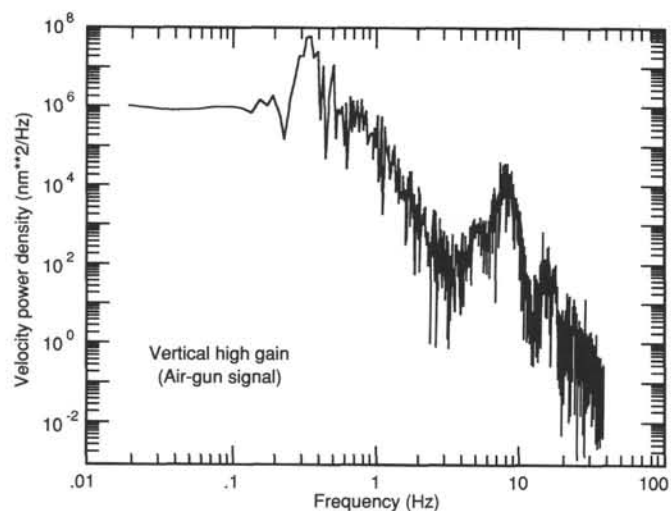


Figure 51. Velocity power spectrum density plot obtained from the air-gun shot 1 record shown in Figure 50. Data length is 50 s with a sampling rate of 80 Hz. A peak at about 8 Hz is due to air-gun shots.

Operation

Hole 794E is located at 40°10.532'N, 138°13.954'E at a water depth of 2800.9 mbsl. This hole is about 1.5 km south of Hole 794D. Drilling began at 1915UTC, 29 September 1989, and Hole 794E was drilled to a total depth of 3200.9 mbsl (400 mbsf) (see "Operations" section, this chapter). The drill pipe then was pulled up to 74.7 mbsf; it was raised to 65.7 mbsf at 1400UTC, 30 September, and to 57.0 mbsf 2 hr later. At 0820UTC, 30 September, five electrodes were attached to the insulated cable on the rig floor, and the sensor cable was lowered through the drill pipe. A sinker bar weighing about 50 kg was connected to the bottom of the sensor cable as a weight. At 1000UTC, 30 September, the sensor cable was installed in Hole 794E (as shown in Fig. 53), and the experiment started.

The ends of the wires were connected to a YEW3655 analyzing recorder for the measurement of the electric potential; the recorder has two input channels with 14-bit A/D converters and 8 kword of memory. This instrument can store and add the observed time series up to 256 times. Stacked data can be transferred to a computer through a GP-IB port for

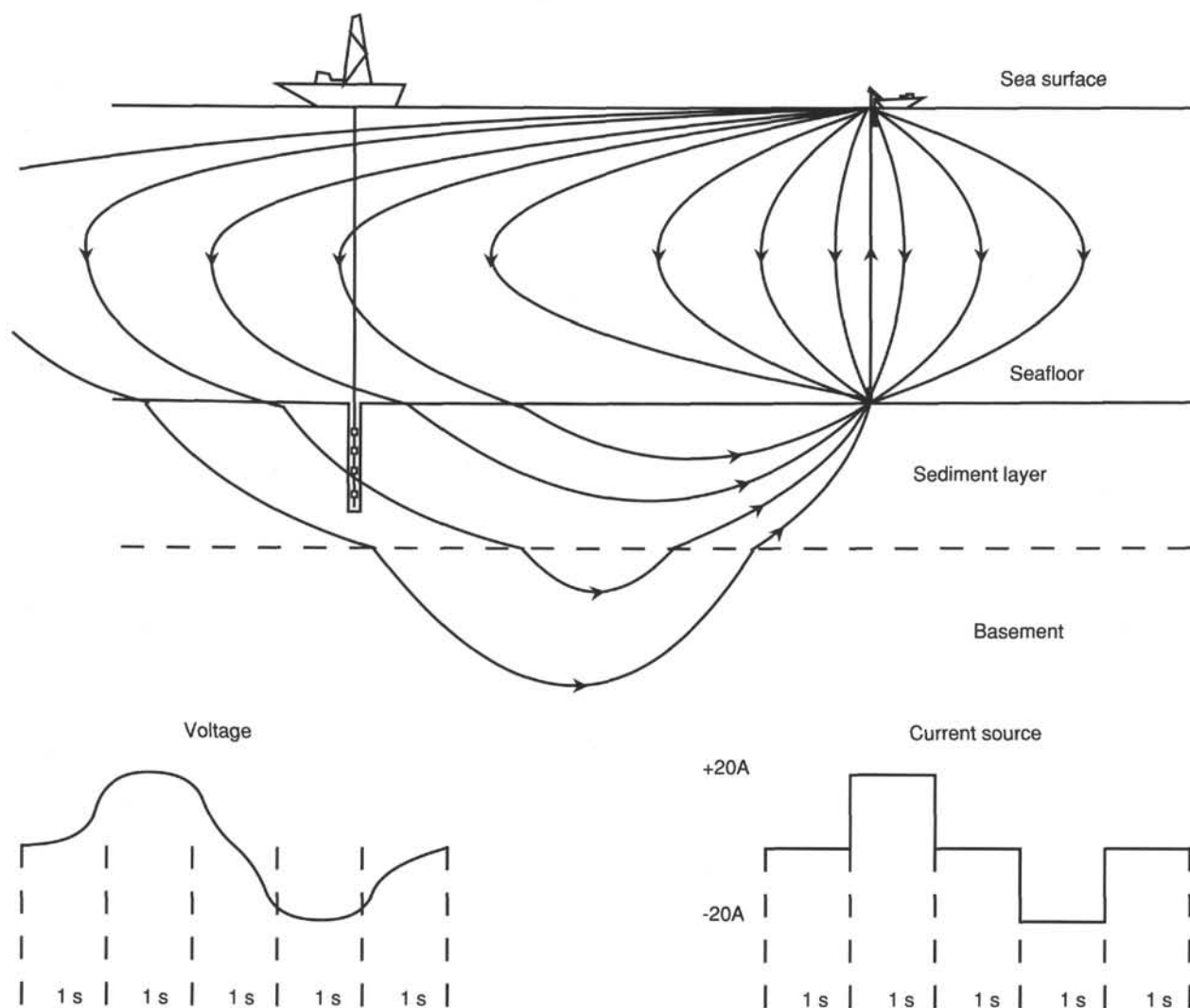


Figure 52. A schematic illustration of the electrical resistivity experiment at Site 794. Time variations of the current source (right) and the observed signal (left) are shown at the bottom.

later analysis. Monitoring the output of the record also is possible with a built-in pen plotter.

After the sensor cable was installed in Hole 794E, we tested the DC offset voltage and noise levels of the five electrodes. Initially, the maximum offset voltage was about 5 mV, but then it decreased to 3 mV within 1 hr. The main cause of this DC offset was the difference in the external electric potentials among the electrodes. The noise level was highest at the uppermost electrode (with amplitude of about 1 mV) and systematically decreased in the lower electrodes. Hence, the two electrode pairs indicated in Figure 53 were used throughout the experiment. The size of the data stack was determined by monitoring the reduction of the noise level. A maximum 256-fold stack was used for the farthest station.

During the experiment, we measured the signal at eight different positions of the shooting ship (*Kaiko-maru-5*), as shown in Figure 54. Four stations were aligned approximately in a N60°E direction, and the other four in a N30°W direction. This configuration was selected to observe a possible anisotropy of the electrical resistivity. The distance and direction of these stations (relative to Hole 794E) are also noted in Figure 54. The nearest station is about 1 km from Hole 794E, and the

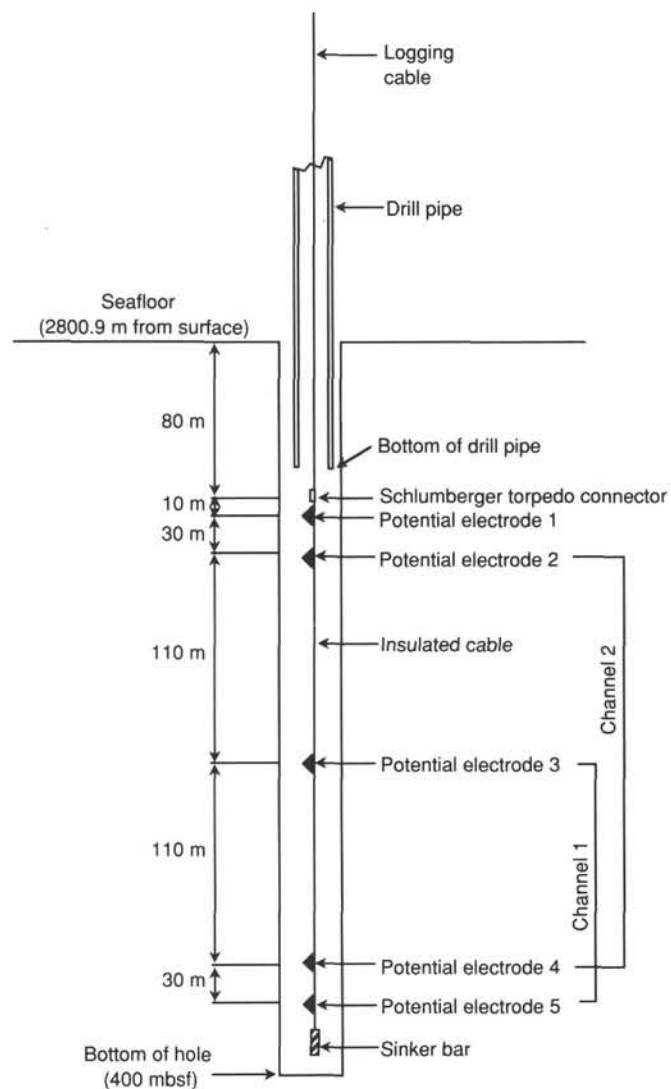


Figure 53. Configuration of the sensor cable during the resistivity experiment in Hole 794E.

Station	Distance (km)	Direction
1	0.94	74°
2	2.41	70°
3	4.07	58°
4	6.29	59°
5	6.62	330°
6	3.89	325°
7	1.90	330°
8	0.85	325°

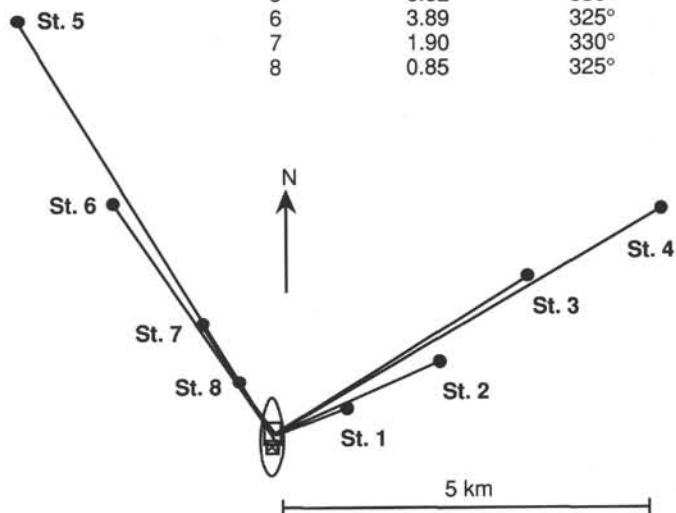


Figure 54. Distance and direction of the current source positions relative to *JOIDES Resolution* during the electrical resistivity experiment at Site 794.

farthest position is about 7 km from the hole. At each station, the shooting ship lowered the current cable to the seafloor and then applied power between the ends of the two cables. The average time required for measuring was about 1 hr, after which the ship pulled the cable to the surface and moved to the next station. Lowering and pulling up the cable took about 40 min; time was shortened during later measurements.

Signal (peak-to-peak) amplitude, observed on the monitor output, varies from about 40 μV at the nearest station to about 2 μV at the farthest station for Channel 1 (the voltage difference between electrodes 3 and 5, distance 140 m), and from 100 to 5 μV for Channel 2 (the voltage difference between electrodes 2 and 4, distance 220 m). The current flow lines, shown in Figure 52, allow us to infer that the variation of the electric potential through the sediment layer is not linear. The potential gradient in the bottom part of the sediment layer tends to be smaller than in the upper part. The absolute value of the potential difference between the electrodes and the degree of the nonlinearity of the potential variation can be used to estimate the resistivity structure at the base of the sediment layer (a thickness of about 550 m). The amplitude of the signal that was observed along the N30°W direction is slightly larger than the one observed along N60°E. Although additional processing of the digital data will be required to obtain the resistivity structure, the above difference suggests an anisotropic structure of the electrical resistivity.

Our experiment was completed at 0800UTC, 1 October 1989, and the sensor cable was pulled up to the rig floor at 1000UTC, 1 October.

CONCLUSIONS

We accomplished all of our main objectives at Site 794; namely, (1) to drill deeper into the acoustic basement complex initially encountered when drilling at this site during Leg 127, with the goal of reaching igneous basement in the Yamato Basin; (2) to install a newly developed downhole seismometer

in basement rock for conducting a real-time multiship seismic experiment and for initiating a long-term program of seismic observations in order to analyze the deep structure beneath the Japan Sea; and (3) to conduct large-scale and oblique resistivity experiments using a dedicated hole to determine the deep resistivity structure beneath this site. A detailed review of the results and conclusions for Site 794 is presented in the site summary at the beginning of the chapter. The following statements simply highlight our major findings at this site.

Igneous Basement Beneath the Yamato Basin

Perhaps the highest priority identified for ODP drilling in the Japan Sea was the recovery of rocks representing acoustic basement to provide the heretofore missing element in analysis of the style and dynamics of rifting in this back-arc basin. Further, the major goal of this quest was to recover igneous basement rock; that is, igneous units formed during the initial rapid spreading and opening of the basin. Drilling of Site 794 during Leg 128 penetrated about 190 m into an igneous complex representing a portion of the late early Miocene(?) volcanic floor and the crust of the northern Yamato Basin. Based primarily on chemical evidence, the rocks we cored in the lower section of Hole 794D probably represent igneous basement at this site.

A total of nine predominantly igneous units were recognized within the sequence cored between 573.0 and 733.5 mbsf in Hole 794D, with good correlation established between the upper units in this hole and the same units cored at the base of Hole 794C during Leg 127. Mineralogical, geochemical, and logging data indicate that the rocks forming this sequence represent two distinct magmatic series that are responsible for the petrologic differences noted in the cores. The Hole 794D lithologic sequence represents a series of stacked sills and flows, including (1) an upper and younger set of dolerite sills and flows of probable island-arc tholeiite composition and minor interbedded sediments and (2) a lower and older series of sills and flows comprising ocean floor basalts of back-arc tholeiite composition. Unit 6 in this latter series is an olivine-pyroxene basaltic flow rock of primitive composition that has been interpreted to represent the top of igneous basement at Site 794.

Geophysical Experiments

Conclusions from the downhole seismometer experiment and long-term observations using this instrument and from the electrical resistivity experiments conducted at Site 794 must await laboratory processing of data and further data accumulation over time.

The emplacement of the downhole seismometer in Hole 794D proceeded smoothly (see "Downhole Seismometer Experiment" section, this chapter). We anticipate that processing of data from the successful multiship experiment using this instrument and a seafloor OBS array will yield new insights into the local crustal structure. This program of long-term observations using the downhole seismometer is aimed at acquiring data from natural earthquakes over several months to be used to determine a three-dimensional view of the crust and mantle structure beneath the Japan Sea.

The oblique electrical resistivity experiment at Site 794 also proceeded without major problems and was aimed at determining the high-resolution resistivity structure for a 10-km-deep crustal section beneath Site 794 (see "Electrical Resistivity Experiment" section, this chapter). Results from the experiment, together with existing data, are expected to establish the resistivity structure within the crust and upper mantle beneath the Japan Sea.

REFERENCES

- Aubouin, J., von Huene, R., et al., 1982. *Init. Repts. DSDP*, 67: Washington (U.S. Govt. Printing Office).
- Becker, K., 1985. Large-scale electrical resistivity and bulk porosity of the oceanic crust, Deep Sea Drilling Project Hole 504B, Costa Rica Rift. In Anderson, R. N., Honnorez, J., Becker, K., et al., *Init. Repts. DSDP*, 83: Washington (U.S. Govt. Printing Office), 419-427.
- Berggren, W. A., Kent, D. V., and Van Couvering, J. A., 1985. Neogene Part 2: Neogene geochronology and chronostratigraphy. In Snelling, N. J. (Ed.), *The Chronology of the Geological Record*. Geol. Soc. London Mem., 10:211-260.
- Biju-Duval, B., Moore, J. C., et al., 1984. *Init. Repts. DSDP*, 78A: Washington (U.S. Govt. Printing Office).
- Bouma, A. H., 1975. Deep-sea fan deposits from the Toyama Trough, Sea of Japan. In Karig, Ingle, et al., *Init. Repts. DSDP*, 31: Washington (U.S. Govt. Printing Office), 471-488.
- Chave, A. D., and Cox, C., 1982. Controlled electromagnetic sources for measuring electrical conductivity beneath the oceans: 1. Forward problem and model study. *J. Geophys. Res.*, 87:5327-5338.
- COSOD II, 1987. *Rept. of the 2nd Conf. on Scientific Ocean Drilling (COSOD II)*, Strasbourg, France, 6-8 July 1987 (European Science Foundation).
- Cox, C. S., Filloux, J. H., and Larsen, J. C., 1970. Electromagnetic studies of ocean currents and electrical conductivity below the ocean floor. In Maxwell, A. E. (Ed.), *The Sea*, Vol. 4, Pt. 2: New York (Interscience), 637-693.
- Cox, C. S., Constable, S. C., Chave, A. D., and Webb, S. C., 1980. Controlled-source electromagnetic sounding of the oceanic lithosphere. *Nature*, 320:52-54.
- Duennebie, F. K., Stephen, R. A., Gettrust, J. F., et al., 1987. *Init. Repts. DSDP*, 88: Washington (U.S. Govt. Printing Office).
- Edwards, R. N., Law, L. K., and DeLaurier, J. M., 1981. On measuring the electrical conductivity of the oceanic crust by a modified magnetometric resistivity method. *J. Geophys. Res.*, 86:11609-11615.
- Filloux, J. H., 1981. Magnetotelluric exploration of the North Pacific: Progress report and preliminary soundings near a spreading ridge. *Phys. Earth Planet. Interiors*, 25:187-195.
- Francis, T. J. G., 1982. Large-scale resistivity experiment at Deep Sea Drilling Project Hole 459B. In Hussong, D. M., Uyeda, S., et al., *Init. Repts. DSDP*, 60: Washington (U.S. Govt. Printing Office), 841-852.
- Fukao, Y., and Furumoto, M., 1975. Mechanism of large earthquakes along the eastern margin of the Japan Sea. *Tectonophysics*, 25:247-266.
- Gnibidenko, H., 1979. The tectonics of the Japan Sea. *Mar. Geol.*, 32:71-87.
- Hey, R., 1977. A new class of "pseudofaults" and their bearing on plate tectonics. *Earth Planet. Sci. Lett.*, 37:321-325.
- Hirata, N., Kinoshita, H., Suyehiro, K., Suyemasu, M., Ouchi, T., Katao, H., Koresawa, S., and Nagumo, S., 1987. Report on the DELP 1985 cruises in the Japan Sea. Part II: Seismic refraction experiment conducted in the Yamato Basin, southeast Japan Sea. *Bull. Earthquake Res. Inst. Univ. Tokyo*, 62:347-365.
- Honza, E. (Ed.), 1979. Geological investigation of the Japan Sea April-June 1978 (GH78-2 Cruise). *Geol. Surv. Japan, Cruise Rept.* 13.
- Hyndman, R. D., Salisbury, M. H., et al., 1984. *Init. Repts. DSDP*, 78B: Washington (U.S. Govt. Printing Office).
- Ichikawa, M., 1971. Re-analysis of mechanism of earthquakes which occurred in and near Japan, and statistical studies on the nodal plane solutions obtained, 1929-1968. *Geophysics*, 35:207-273.
- Inoue, M., and Honza, E., 1979. Bathymetric survey. In Honza, E. (Ed.), *Geological Investigation of the Japan Sea, April-June 1978 (GH78-2 Cruise)*. Geol. Surv. Japan, Cruise Rept., 13:14-19.
- Ishii, T., Yamashita, S., Kobayashi, H., Kitamura, A., Shimizu, T., Konishi, K., Tsuchi, R., and Kobayashi, K., 1988. Description of dredged samples from Erimo Seamount and Meiyō-Daini Seamount (Japan Sea) during KH 86-2 cruise. In Kobayashi, K. (Ed.), *Geophysical and Geological Investigation of the Northeastern*

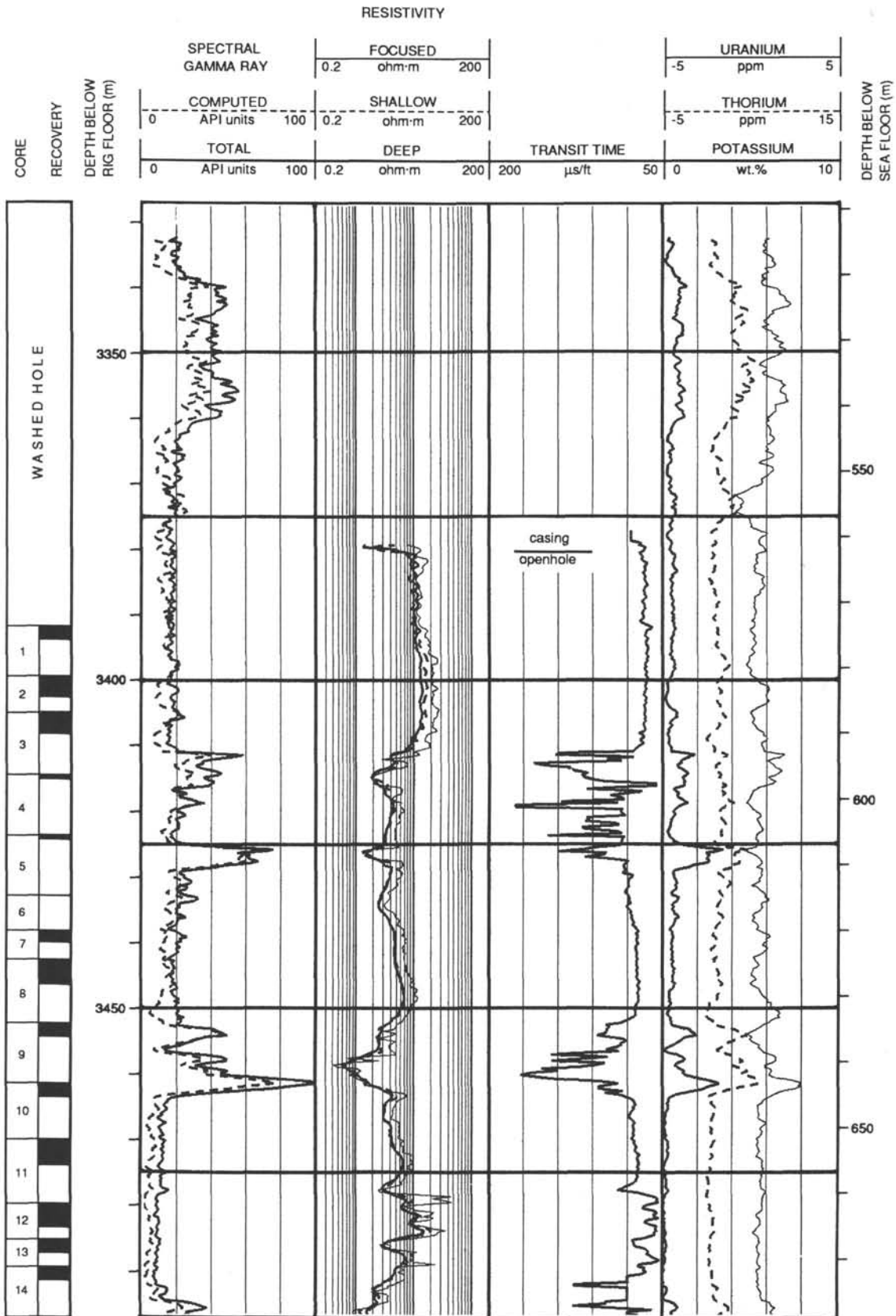
- Part of the Japan Sea and Japan Trench. Preliminary report of the Hakuho Maru cruise KH 86-2* (in Japanese).
- Ishikawa, Y., Takeo, M., Hamada, N., Katsumata, M., Satake, K., Abe, K., Kikuchi, M., Sudo, K., Taskahashi, M., Kashiwabara, S., and Mikami, N., 1984. Mechanism of the central Japan Sea earthquake, 1983. *Chikyū (The Earth Monthly)*, 6:11-17 (in Japanese).
- Jolivet, L., 1987. America-Eurasia plate boundary in eastern Asia and opening of marginal basins. *Earth Planet. Sci. Lett.*, 81:282-288.
- Jolivet, L., and Huchon, P., 1989. Crustal-scale strike-slip deformation in Hokkaido, northern Japan. *J. Struct. Geol.*, 11:509-522.
- Kaneoka, I., 1986. Constraints on timing of the evolution of the Japan Sea based on radiometric dates. *J. Geomag. Geoelec.*, 38:475-485.
- Kaneoka, I., Notsu, K., Takigami, Y., Fujioka, K., and Sakai, H., in press. Constraints on the evolution of the Japan Sea based on ^{40}Ar - ^{39}Ar ages and Sr isotopic ratios for volcanic rocks of the Yamato Seamount chain in the Japan Sea. *Earth Planet. Sci. Lett.*
- Kaneoka, I., and Yuasa, M., 1988. ^{40}Ar - ^{39}Ar age studies on igneous rocks dredged from the central part of the Japan Sea during GH78-2 Cruise. *Geochem. J. Japan*, 22:195-204.
- Karig, D. E., Ingle, J. C., Jr., et al., 1975. *Init. Repts. DSDP*, 31: Washington (U.S. Govt. Printing Office).
- Katao, H., 1988. Seismic structure and formation of the Yamato Basin. *Bull. Earthquake Res. Inst. Univ. Tokyo*, 63:51-86.
- Kimura, G., and Tamaki, K., 1986. Collision, rotation and back-arc spreading in the region of the Okhotsk and Japan seas. *Tectonics*, 5:389-401.
- Kobayashi, K., 1985. Sea of Japan and Okinawa Trough. In Nairn, A.E.M., Stehli, F. G., and Uyeda, S. (Eds.), *The Ocean Basins and Margins. Vol. 7A: The Pacific Ocean*: New York (Plenum Press), 419-458.
- Lallemant, S., and Jolivet, L., 1986. Japan Sea: a pull apart basin? *Earth Planet. Sci. Lett.*, 76:375-389.
- Lewis, B.T.R., Robinson, P. T., et al., 1983. *Init. Repts. DSDP*, 65: Washington (U.S. Govt. Printing Office).
- Ludwig, W. J., Murauchi, S., and Houtz, R. E., 1975. Sediments and structure of the Japan Sea. *Geol. Soc. Am. Bull.*, 86:651-664.
- Menard, H. W., Natland, J., Jordan, T., Orcutt, J., et al., 1987. *Init. Repts. DSDP*, 91: Washington (U.S. Govt. Printing Office).
- Miyazaki, T., 1979. Gravity survey. In Honza, E. (Ed.), *Geological Investigation of the Japan Sea April-June 1978 (GH78-2 Cruise)*. Geol. Surv. Japan Cruise Rept., 13:27-45.
- Miyazaki, T., Tamaki, K., and Murakami, F., 1979. Geomagnetic survey. In Honza, E. (Ed.), *Geological Investigation of the Japan Sea April-June 1978 (GH78-2 Cruise)*. Geol. Surv. Japan Cruise Rept., 13:46-47.
- Murauchi, S., 1966. Exploration seismology. In National Committee for UMP (Eds.), *Second Progress Report on the Upper Mantle Project of Japan (1965-1966)*: Tokyo (Science Council Japan), 11-13.
- Nobes, D. C., Law, L. K., and Edwards, R. N., 1986. The determination of resistivity and porosity of the sediment and fractured basalt layers near the Juan de Fuca Ridge. *Geophys. J. R. Astr. Soc.*, 289-317.
- Pearce, J. A., 1982. Trace element characteristics of lavas from destructive plate boundaries. In Thorpe, R. S. (Ed.), *Andesites*: New York (Wiley and Sons), 525-548.
- Pearce, J. A., and Cann, J. R., 1973. Tectonic setting of basic volcanic rocks determined using trace element analyses. *Earth Planet. Sci. Lett.* 19:290-300.
- Romanowicz, B., and Dziewonski, A. M., 1986. Towards a federation of broadband seismic networks. *EOS, Trans. Am. Geophys. Union*, 67:541-542.
- Sakurai, M., and Sato, T., 1971. Submarine geological structure and history of the Mogami Trough. *J. Geol. Soc. Japan*, 77:489-496.
- Saunders, A. D., and Tarney, J., 1984. Geochemical characteristics of basaltic volcanism within back-arc basins. In Kokelaar, B. P., and Howells, M. F. (Eds.), *Marginal Basin Geology*: Oxford (Blackwell), 59-76.
- Seno, T., and Eguchi, T., 1983. Seismotectonics of the western Pacific region. In Hilde, T.W.C., and Uyeda, S. (Eds.), *Geodynamics of the Western Pacific*. Am. Geophys. Union and Geol. Soc. Am., Geodyn. Ser., 11:5-40.
- Shimazaki, K., and Mori, J., 1983. The mechanism of the 1983 Japan Sea earthquake. *Seismol. Soc. Japan, Fall Meeting*. [Abstracts and Program].
- Tamaki, K., 1988. Geological structure of the Japan Sea and its implications. *Bull. Geol. Surv. Japan*, 39:269-365.
- Tamaki, K., and Honza, E., 1985. Incipient subduction and obduction along the eastern margin of the Japan Sea. *Tectonophysics*, 119:381-406.
- Tamaki, K., Honza, E., Yuasa, M., Nishimura, K., and Murakami, F., 1981. Geological map of the central Japan Sea. *Geol. Surv. Japan, Mar. Geol. Map Ser. 15*, scale 1:1,000,000.
- Tamaki, K., Kobayashi, K., Isezaki, N., Sayanagi, K., Nakanishi, N., and Park, C. H., 1988. Measurement of geomagnetic total force by a proton precession magnetometer. In Kobayashi, K. (Ed.), *Geophysical and Geological Investigation of the Northeastern Part of the Japan Sea and Japan Trench. Preliminary Report of the Hakuho Maru Cruise KH 86-2 (April 21-May 15, 1986)*: Tokyo (Ocean Res. Inst., Univ. Tokyo), 7-9.
- Tamaki, K., Pisciotto, K., Allan, J., et al., in press. *Proc. ODP, Init. Repts.*, 127: College Station, TX U.S.A. (Ocean Drilling Program).
- Ueno, N., Kaneoka, J., Ozima, M., Zashu, M., Sato, T., and Iwabuchi, Y., 1971. K-Ar age, Sr isotope ratio and K/Rb ratio of volcanic rocks dredged from the Japan Sea. In Asano, S., and Udintsev, G. B. (Eds.), *Island Arc and Marginal Seas*: Tokyo (Tokai Univ. Press), 305-309 (in Japanese).
- Utada, H., Hamano, Y., and Segawa, J., 1986. Electrical conductivity structure under the Japanese Islands and vicinity. *J. Geomag. Geoelec.*, 38:447-473.
- Von Herzen, R. P., Francis, T.J.G., and Becker, K., 1983. *In-situ* large-scale electrical resistivity of ocean crust, Hole 504B. In Cann, J. R., Langseth, M. G., Honnorez, J., Von Herzen, R. P., White, S. M., et al., *Init. Repts. DSDP*, 69: Washington (U.S. Govt. Printing Office), 237-244.
- Yamashita, S., 1988. Andesitic lava recovered from Meiyō-Daini Seamount in the Yamato Basin during KH 86-2 Cruise. In Kobayashi, K. (Ed.), *Preliminary Report of the Hakuho Maru Cruise KH 86-2*: Tokyo (Ocean Res. Inst. Univ. Tokyo), 67-74.
- Yoshii, T., 1972a. Features of the upper mantle around Japan as inferred from gravity anomalies. *J. Phys. Earth*, 20:23-34.
- , 1972b. Terrestrial heat flow and features of the upper mantle beneath the Pacific and Sea of Japan. *J. Phys. Earth*, 20:271-285.
- Yoshii, T., and Asano, S., 1972. Time-term analysis of explosion seismic data. *J. Phys. Earth*, 20:47-57.
- Yoshii, T., and Yamano, M., 1983. Digital heat flow data file around the Japan Islands. In unpublished data files, Univ. of Tokyo Earthquake Res. Inst.
- Yukutake, T., Filloux, J. H., Segawa, J., Hamano, Y., and Utada, H., 1983. Preliminary report on a magnetotelluric array study in the Northwest Pacific. *J. Geomag. Geoelectr.*, 35, 575-587.

Ms 128A-104

NOTE: All core description forms ("barrel sheets") and thin sections have been reproduced on specially coated paper and may be found in Section 3, at the end of the volume, beginning on page 405.

Formation microscanner images for this site are presented on microfiche in the back of this volume.

Hole 794D: Resistivity-Sonic-Gamma Ray Log Summary



Hole 794D: Resistivity-Sonic-Gamma Ray Log Summary (continued)

